Experimental Investigation of Topological Superconductors

Huaqian Leng

Experimental Investigation of Topological Superconductors

Huaqian Leng

Experimental investigation of topological superconductors

Huaqian Leng

Copyright © Huaqian Leng 2020
Cover design by Huaqian Leng
All rights reserved

ISBN: 978-94-028-2021-8
Printed by IPSKAMP printing

Experimental investigation of topological superconductors

ACADEMISCH PROEFSCHRIFT

ter verkrijging van de graad van doctor
aan de Universiteit van Amsterdam
op gezag van de Rector Magnificus
prof. dr. ir. K.I.J. Maex
ten overstaan van een door het College voor Promoties
ingestelde commissie, in het openbaar te verdedigen
in de Aula der Universiteit
op woensdag 17 juni 2020, te 15:00 uur

door

Huaqian Leng

geboren te Shandong

Promotieecommissie:

Promotor: Dr. A. de Visser, Universiteit van Amsterdam
Copromotor: Prof. dr. M.S. Golden, Universiteit van Amsterdam

Overige leden: Prof. dr. C. Pappas, Technische Universiteit Delft
Prof. dr. ir. A. Brinkman, Universiteit Twente
Dr. T. Naka, National Institute for Materials Science, Japan
Dr. E. van Heumen, Universiteit van Amsterdam
Prof. dr. P.C.M. Planken, Universiteit van Amsterdam
Prof. dr. F.E. Schreck, Universiteit van Amsterdam

Faculteit der Natuurwetenschappen, Wiskunde en Informatica

Title: Experimental investigation of topological superconductors
Doctoral thesis, University of Amsterdam, 2020
Contact: lenghuaqian@hotmail.com

The research reported in this dissertation was carried out at the Van der Waals-Zeeman Institute for Experimental Physics, University of Amsterdam. The work was partly financed by the China Scholarship Council (CSC) (Grant No. 201604910855), China.

“道可道, 非常道.” – 老子 《道德经》

“Truth can be known, but it may not be the well-known truth.”
– Lau Tzu, *Tao Te Ching*

“But life is very short and anxious for those who forget the past,
neglect the present, and fear the future”
– Lucius Annaeus Seneca,
On the Shortness of Life

To my family and the people who dedicated to fight COVID-19.

Contents

Chapter 1

Introduction

Topological superconductors

Topology originates from a mathematical concept used to classify geometrical objects. Two shapes are said to have the same topology when they can be continuously deformed into each other. When topology is introduced into condensed matter systems, it is used to distinguish how the atomic wavefunctions are combined. A quantum state whose wavefunction bears a distinct character from the atomic limit adiabatically may be called topological [1]. This distinct character can be specified by topological invariants. Superconductors realizing such a topological state in their bulk may be classified as topological superconductors (TSCs). As a new class of quantum materials, TSCs have attracted widespread attention in recent years, not only because their concept is strongly tied to Majorana zero modes, which are significant for developing future devices in quantum computation, but also since it deepens the understanding of quantum mechanics in solids [2].

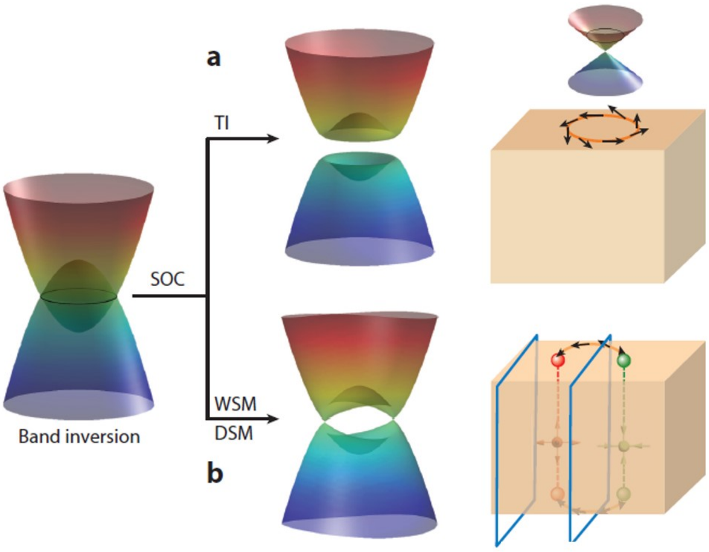

Figure 1.1: The topological insulator and Weyl/Dirac semimetal. The topology of both TI and WSM/DSM results from a band opened by SOC after band inversion. (a) TI with a fully open gap and a surface state (closed loop). (b) WSM/DSM with linear energy dispersion at isolated points and its surface state (Fermi arcs). The figure is taken from Ref. [3].

The research in topological states of matter has made a remarkable progress in the past decades. Although quantum Hall systems have been recognised to be topologically non-trivial since 1982 [4], topological quantum systems have gained wide interests after the discovery of topological insulators (TIs) in 2005 [5, 6]. TIs, different from ordinary insulators, have a gapped band structure in the bulk, but host gapless surface state at the boundary. The surface states are Dirac fermions with a spin-momentum-locked linear energy dispersion. This nontrivial electronic structure results from the inversion of a conduction and valence band by strong spin-orbit coupling (SOC) (see Fig. 1.1). TIs can be characterized by gapless boundary states or a topological invariant. These characteristics generally are referred to as symmetry-protected topological phases, which rely on the presence of certain symmetries, *i.e.* time-reversal symmetry and crystal symmetry [7]. TI properties have been studied in many materials, such as HgTe [8], $\mathrm{Bi_2Se_3}$ [9, 10] and $\mathrm{Bi}_{1-x}\mathrm{Sb}_x$ alloys [11, 12].

Most interestingly, it was proposed that topological classifications are possible for the quantum many-body system where the occupied negative-energy states in the energy-band spectrum are protected by a gap [13, 14]. Therefore systematically superconductors come in view as a new classification of topological matter. TSCs realize a state with a full superconducting gap in the bulk, gapless states protected by symmetry at the boundary. The existence of such gapless boundary states is one of the hallmarks of TSCs. The surface state is correspondingly called an Andreev bound state. Distinct from TIs the excitations in TSCs are not electrons, but Bogoliubov quasiparticles: a linear combination of electron and hole excitations [1]. Particle-hole symmetry is essential to obtain Majorana states in the topological gapless boundary excitations. Generally topological superconductivity cannot be adiabatically connected to the Bose-Einstein condensate of Cooper pairs in a trivial superconducting state. It implies TSC can only be found in unconventional superconductors [15]. A famous intrinsic TSC candidate is the two dimension a chiral $p_x + ip_y$ spin-triplet superconductor, $\mathrm{Sr_2RuO_4}$. It has been investigated extensively, and although the surface Andreev bound state was observed [16], the conclusion of p-wave superconductivity in $\mathrm{Sr_2RuO_4}$ is still under debate [17, 18]. In general superconductors that host a spin-triplet order parameter are rare. On the one hand, extensive efforts have been made on proximity-coupled superconductivity in topological surface states by interfacing with conventional superconductors [19, 20, 21]. On the other hand, superconductivity can also be induced by doping of topological insulators to achieve a state where topologically nontrivial states and robust superconductivity coexist [22, 23, 24]. Promising TSC candidates can be found among the doped 3D topological insulators $\mathrm{Cu}_x\mathrm{Bi_2Se_3}$ [25, 23, 22] and $\mathrm{Sr}_x\mathrm{Bi_2Se_3}$ [24, 26], the doped semiconductor $\mathrm{Sn}_{1-x}\mathrm{In}_x\mathrm{Te}$ [27] and the half-Heusler platinum bismuthide family with 111 stoichiometry: LaPtBi [28], YPtBi [29, 30] and LuPtBi [31].

As discussed above the gap in TIs is fully opened by SOC after band inversion. When the bulk bands are gapped by SOC except at some points where a linear energy dispersion is found (the 3D analog of graphene), a novel classification of

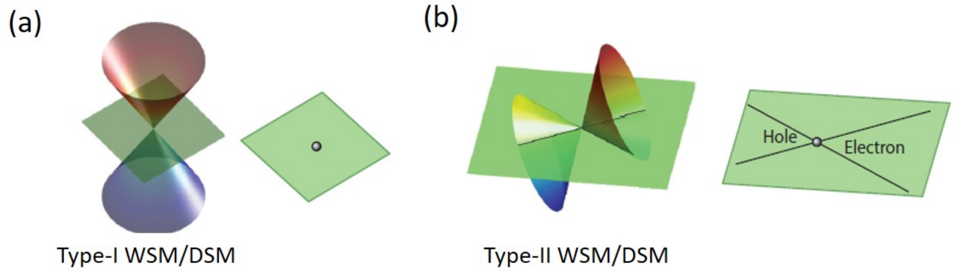

Figure 1.2: Type I and type II WSM/DSM with Weyl/Dirac points sufficiently close to the Fermi energy. (a) Type I WSM/DSM with tilt parameter $k < 1$. The Fermi surface shrinks to zero at the Weyl/Dirac point. (b) Type II WSM/DSM. The Dirac cone is strongly tilted, $k > 1$. Electron and hole pockets are touching around the Weyl/Dirac point. The figure is taken from Ref. [3].

topological matter Weyl semimetal (WSM) is used [32, 33, 34]. WSMs have further extended the repertoire of exotic topological states with topological Fermi arcs on the surface and chiral magnetic effects in the bulk. The Fermi arcs provide a strong proof to identify a WSM. They provide unclosed line on the Fermi surface connecting two Weyl points. This is distinct from the surface states of TIs that commonly form a closed loop [3] (see Fig. 1.1). The WSMs require a breaking of either time-reversal symmetry or inversion symmetry. Coexistence of both symmetries leads to the related Dirac semimetal (DSM) phase. Remarkably, unlike in WSMs, the topological surface state, namely Fermi arcs, is unstable in DSMs. It implies that when the DSM is in the superconducting state, the electrons on the surface may form Cooper pairs, and surface superconductivity is expected [35, 36]. WSMs/DSMs with tilt parameter $k < 1$ generally are classified as type I while the type II class has $k > 1$ [37, 38] (see Fig. 1.2). The open pockets of electrons and holes near Weyl/Dirac points may contribute to a large density of states, which is favorable for superconductivity. Therefore, the type II DSM as a 3D topological material is proposed to be a fruitful platform for TSC. Many WSM candidates have been predicted by theoretical calculations [39, 40] and experimentally confirmed by the observation of Fermi arcs using angle-resolved photoemission spectroscopy (ARPES) [14, 41], for instance TaAs [13], TaP, NaAs and NbP. In addition DSM states were found to exist in Na_3Bi [2], Cd_3As_2 [42, 43, 44] and $PdTe_2$ [35, 45, 46].

This thesis focuses on superconductivity in two topological materials: (i) the Dirac semimetal $PdTe_2$, and (ii) the doped topological insulator $Sr_xBi_2Se_3$.

The transition metal dichalcogenides $PdTe_2$ was recently reported to be a type II Dirac semimetal with the Dirac point at ~0.6 eV below the Fermi energy E_F. This was demonstrated by electronic band structure calculations [35] and

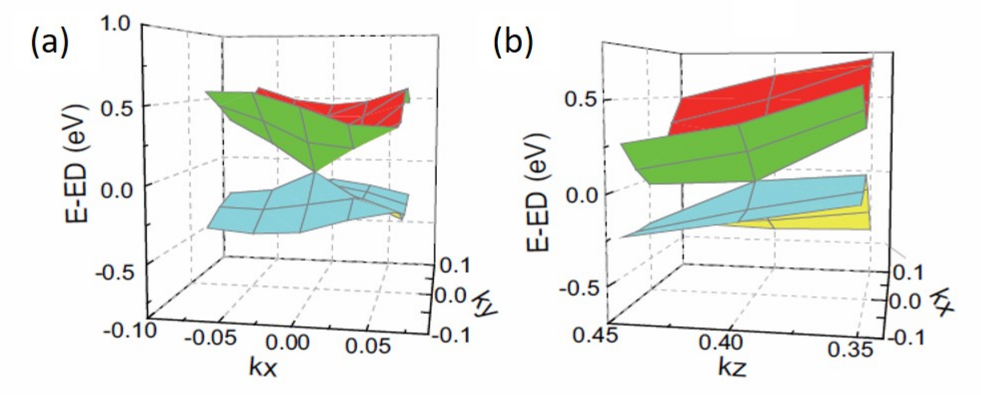

Figure 1.3: Dirac electronic structure calculated for $PdTe_2$. Projection of the Dirac cone on k_x-k_y (a) and k_x-k_z (b). The tilt feature of the Dirac cone is along the k_z direction. ED is the energy of the Dirac cone which is 0.6 eV below E_F. The figure is taken from Ref. [35].

ARPES [45, 46, 47] (see Fig. 1.3). Interestingly, $PdTe_2$ also hosts superconductivity with a critical temperature $T_c = 1.6$ K and a critical field $H_c(0) = 13.6$ mT. This prompts the question whether the superconductivity has a topological nature and whether surface superconductivity exists when the DSM is in the superconducting state. This provides the motivation to investigate the superconducting properties of $PdTe_2$ in detail, the results of which are presented in Chapters 4-6.

The tetradymite Bi_2Se_3 is one of the prototypical topological insulators that has been used to develop the field of 3D TSCs. Superconductivity can easily be induced by doping with Cu [25], Sr [48], Nb [49] or Tl [50]. Cu doped Bi_2Se_3 was the first material in this family to show induced superconductivity, and also is the most studied one. Topological surface states in the normal phase of $Cu_xBi_2Se_3$ were confirmed by ARPES measurements [51]. Fu and Berg proposed $Cu_xBi_2Se_3$ to be an intrinsic topological superconductor with an odd-parity superconducting order parameter [52]. Evidence for this was extracted by the observation of a nematic superconducting state in experiments. The possible superconducting order parameters were evaluated by a symmetry-group classification and odd-parity states ($\triangle_2$, $\triangle_3$, $\triangle_4$-pairing) were put forward as order parameter. The most significant development in $Cu_xBi_2Se_3$ is the observation of rotational symmetry breaking. The symmetry in the superconducting phase is spontaneously lowered to twofold when a magnetic field is applied directed in the trigonal basal-plane. This has been demonstrated by field angular variation measurements of the nuclear magnetic resonance (NMR) signal [22] and specific-heat [53]. This result points to the $\triangle_4$ pairing state, since such an in-plane anisotropy in the gap amplitude is only compatible with the $\triangle_4$ state [54]. Moreover, in this superconducting state

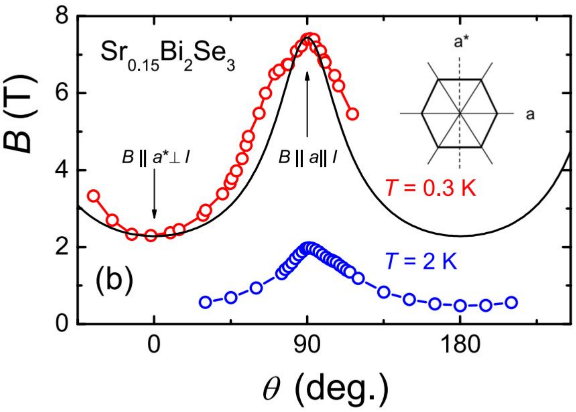

Figure 1.4: Angular variation of the upper critical field B_{c2} in the basal (aa^*-plane) for $\mathrm{Sr_{0.15}Bi_2Se_3}$ at the temperature indicated. The data are obtained from magnetoresistance measurements at fixed temperature. The angle $\theta = 0°$ corresponds to $B \parallel a^* \perp I$ and $\theta = 90°$ to $B \parallel a \parallel I$. The a and a^* directions in the hexagonal basal plane are defined as in the figure in the upper right corner. The figure is taken from Ref. [24].

a nematic director pinned to the crystal lattice lowers the rotational symmetry to twofold, hence this state is labelled as nematic superconductivity [55].

Superconductivity in $\mathrm{Sr}_x\mathrm{Bi_2Se_3}$ was discovered by Liu *et al.* [48]. The presence of a non-trivial surface state was identified by the Dirac-like dispersion observed by ARPES [56, 57]. A great advantage of working with $\mathrm{Sr}_x\mathrm{Bi_2Se_3}$ is that the superconducting volume fraction of single crystals can be as large as 90 %, compared to only 50 % for $\mathrm{Cu}_x\mathrm{Bi_2Se_3}$. Further the superconducting state in $\mathrm{Sr}_x\mathrm{Bi_2Se_3}$ for $x = 0.10$ was characterized by Shruti *et al.* [58] who reported a large Ginzburg-Landau parameter, $\kappa \approx 120$, pointing to extreme type II superconducting behavior. A surprising discovery was made by Pan *et al.* [24] by performing magnetotransport measurements on crystals with nominal concentrations $x = 0.10$ and 0.15: the angular variation of the upper critical field, $B_{c2}(\theta)$, showed a pronounced two-fold anisotropy for field directions in the basal plane, *i.e.* the rotational symmetry is broken (see Fig. 1.4). As mentioned in the discussion on $\mathrm{Cu}_x\mathrm{Bi_2Se_3}$ the breaking of rotational symmetry provides a strong evidence that the $\triangle_4$ state is realized in $\mathrm{Bi_2Se_3}$-based superconductors. The nematicity is supposed to manifest itself in many properties, such as the magnetic penetration depth. Therefore transverse-field (TF) μSR experiments on single crystals $\mathrm{Sr}_x\mathrm{Bi_2Se_3}$ with nominal concentrations $x = 0.15$ and 0.18 ($T_c \sim 3$ K) were carried out to search for in-plane anisotropy in the penetration depth. μSR experiments on $\mathrm{Sr}_x\mathrm{Bi_2Se_3}$ are described in Chapter 7.

Outline of this thesis

In this dissertation we present the experimental results of extensive investigations on the candidate topological superconductors $PdTe_2$ and $Sr_xBi_2Sr_3$. Magnetic and transport measurements, and muon spin relaxation (μSR) experiments were carried out to unveil the superconducting nature as well as its interaction with topological features. The outline of this thesis is as follows:

- Chapter 2 describes all the experimental techniques used in this thesis project. We start with the preparation and characterization of the samples. A brief discussion about the theory behind and the key components of the cryostat follows. Next we move to the experimental details regarding resistivity and susceptibility measurements, and the high pressure technique. At last we introduce the Muon Spin Rotation and Relaxation (μSR) technique and the experimental setup.

- Chapter 3 discusses the theoretical aspects relevant for this thesis project. First a brief introduction of superconductivity is given, as well as the classification of superconductors. Two characteristic lengths in superconductors are addressed, and the criteria for type I, type II and type II/1 superconductivity are given. Then the typical behavior of both type I and type II superconductors in an applied magnetic field is discussed. Next we discuss the basics of surface superconductivity derived from the Saint James and De Gennes Model. Furthermore, the principle of pressure effects on the critical temperature T_c is presented. In the last part of this chapter we will explain the methodology of the data analysis for the μSR technique.

- Chapter 4 reports dc-magnetization, ac-susceptibility and transport measurements on single crystals of $PdTe_2$, conducted to determine the nature of the superconducting condensate. Type I superconductivity with $T_c = 1.64$ K and a critical field $\mu H_c(0) = 13.6$ mT is demonstrated by dc-magnetization measurements and the differential paramagnetic effect observed in ac susceptibility. Our crystals also show enhanced surface superconductivity in fields above the critical field H_c. The surface superconductivity does not obey the standard Saint-James-de Gennes behavior with critical field $H_{c3} = 2.39 \times \kappa H_c$. These unusual results are discussed in view of the presence of topological surface states.

- Chapter 5 presents the results of a high-pressure investigation of the superconducting phase diagram of $PdTe_2$ single crystals ($p \leq 2.5$ GPa). Combined resistivity and ac-susceptibility measurements show T_c increases at low pressures, then passes through a maximum of 1.91 K around 0.91 GPa, and subsequently decreases at higher pressure. Under pressure superconductivity maintains its type-I character. Surface superconductivity persists under pressure as demonstrated by the large superconducting screening signal for applied dc-fields $H_a > H_c$. Interestingly, for $p \geq 1.41$ GPa the superconducting transition temperature of the surface, T_c^S, is larger than T_c of the bulk. This result yields support that surface superconductivity may possibly have a non-trivial topological nature. The measured pressure variation of T_c is compared with recent results from band structure calculations, and the importance of a Van Hove singularity is also discussed.

- Chapter 6 shows an investigation of the superconducting phase of $PdTe_2$ on the microscopic scale via the μSR technique. Experiments were performed in transverse field on a thin disk-like crystal in two configurations: (*i*) with the field perpendicular to the plane of the disk (the demagnetization factor, $N_\perp = 0.87$) and (*ii*) with the field in the plane of the disk ($N_\parallel = 0.08$). By analysing the asymmetry of the μSR signal we find that the normal phase volume fraction grows quasi-linearly with applied field at the expense of the Meissner phase fraction. This provides solid evidence for the intermediate state and type-I superconductivity in the bulk of our $PdTe_2$ crystal.
- Chapter 7 focuses on a muon spin rotation study on $Sr_xBi_2Se_3$ in transverse field. The measurements show that the increase of the relaxation rate σ_{TF} is smaller than the experimental uncertainty in field-cooling experiments, which tell us the magnetic penetration depth λ is very large (≥ 2.3 μm for $T \rightarrow 0$). On the other hand, when we induce disorder in the vortex lattice by changing the magnetic field below T_c a sizeable damping rate $\sigma_{SC} \approx 0.36$ μs^{-1} ($T \rightarrow 0$) is obtained. These results provide microscopic evidence for a superconducting volume fraction of ~ 70 % in the crystal with nominal Sr content $x = 0.18$ and thus bulk superconductivity.

Chapter 2

Experimental techniques

In this chapter we describe all the experimental techniques used in this thesis project. We start with the preparation and characterization of the samples. A brief discussion about the theory behind and the key components of the cryostat follows. Next we move to the experimental details regarding resistivity and susceptibility measurements, and the high pressure technique. At last we introduce the Muon Spin Rotation and Relaxation (μSR) technique and the experimental setup.

2.1 Sample preparation and characterization

All single crystals measured during this thesis project were prepared at the Van de Waals-Zeeman Institute (WZI) by Dr. Y.K Huang, except some batches of $Sr_{0.18}Bi_2Se_3$ that were fabricated by Dr. D. Cherian. For the different measurement techniques samples with specific shapes and dimensions are needed. Those were cut from the single-crystalline batches by a scalpel and/or wire spark erosion.

2.1.1 $PdTe_2$

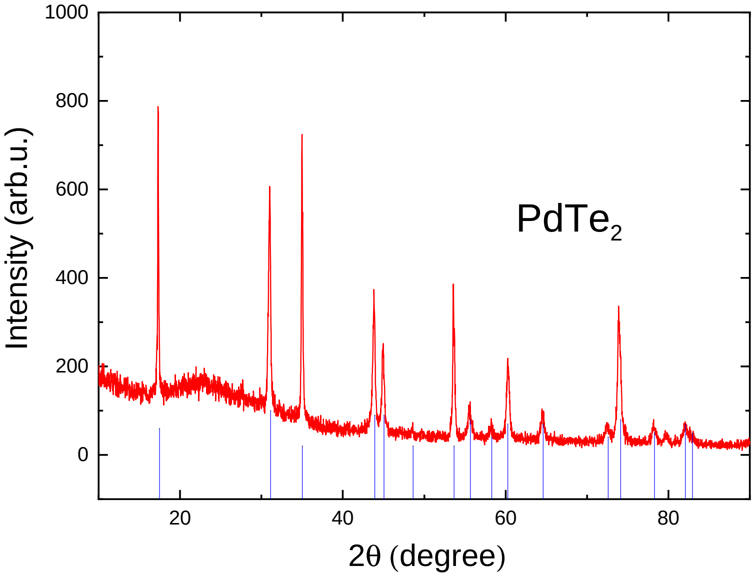

Figure 2.1: Powder diffraction pattern of $PdTe_2$. The blue lines indicate the expected Bragg positions.

Single crystalline samples of $PdTe_2$ were prepared by a modified Bridgeman technique [59]. A powder X-ray diffraction pattern was measured on a crushed piece of the $PdTe_2$ single crystal (see Fig. 2.1). The diffraction pattern, taken with Cu-K_α radiation, confirmed the trigonal CdI_2 structure (spacegroup $P\bar{3}m1$) with lattice parameters a = 4.034 Å and c = 5.132 Å. The pattern shows single phase homogeneity within the experimental resolution (5 %). Laue backscattering was used to orientate the crystals. The chemical composition and stoichiometry of the prepared $PdTe_2$ crystalline batch was investigated by Scanning Electron Microscopy (SEM; Hitachi TM3000) with Electron Dispersive X-ray Spectroscopy (EDX; Quantax 70) at the WZI. Experiments were performed on several single-crystalline pieces, some of them with freshly cleaved surfaces. All these measurements showed the proper 1:2 stoichiometry within the experimental resolution of

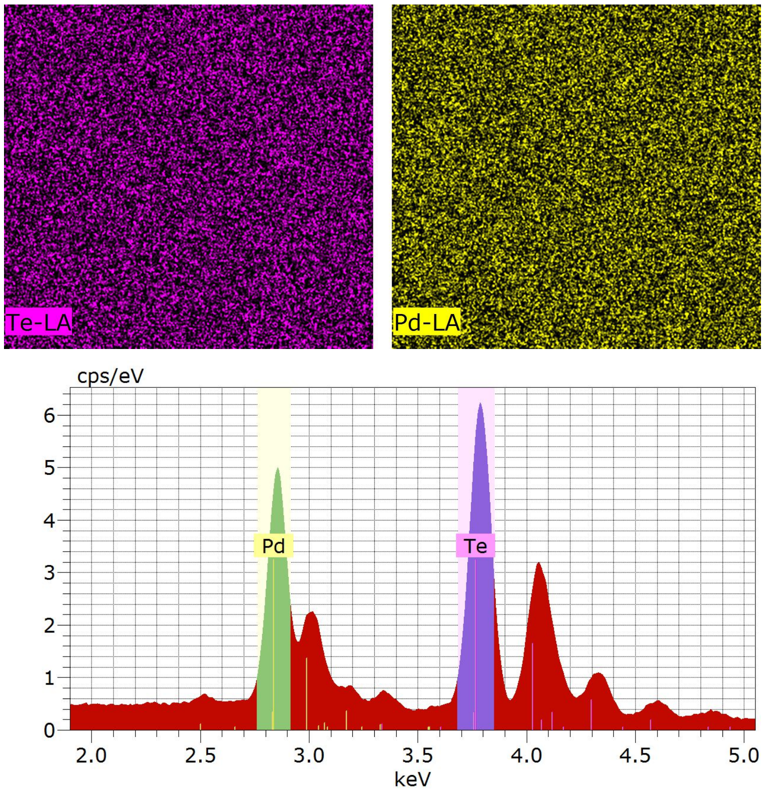

Figure 2.2: EDX analysis of the surface of $PdTe_2$. The surface scans (upper panels, scanned area 360 μm × 385 μm) show the distribution of Pd and Te is homogeneous. The EDX spectrum (lower panel) gives a Pd : Te ratio 33.2 : 66.8.

0.5 %, and a typical SEM micrograph and composition layout are shown in Fig. 2.2. The crystal was characterized by electrical resistivity and ac-susceptibility measurements. It has a superconducting transition temperature of 1.57 K (see Fig. 2.3 inset). Ac-susceptibility measurements show a superconducting shielding fraction of close to 100 %. The resistivity is metallic and the residual resistance ratio $R(300\text{K})/R(2\text{K}) = 30$ as shown in Fig. 2.3.

2.1.2 $Sr_xBi_2Se_3$

Single crystalline samples of $Sr_xBi_2Se_3$ with nominal values $x = 0.15$ and $x = 0.18$ were synthesized by melting high-purity elements at 850 °C in sealed evacuated quartz tubes. The crystals were formed by slowly cooling to 650 °C at a rate of 3 °C/hour. Powder X-ray diffraction confirmed the $R\bar{3}m$ space group [24]. The single-crystalline nature of the crystals was checked by Laue back-reflection [24]. Ac-susceptibility measurements of the single crystalline batch with $x = 0.15$

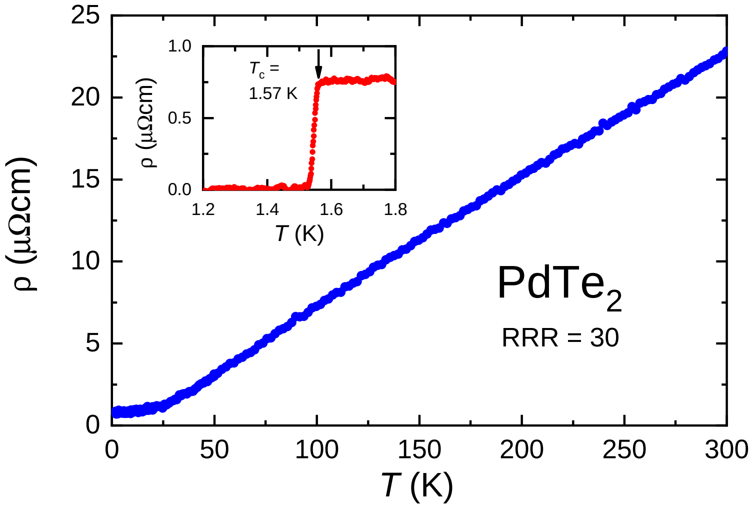

Figure 2.3: Temperature variation of the electrical resistivity of PdTe$_2$. The inset shows the superconducting transition. The arrow points to the onset temperature T_c^{onset} of 1.57 K.

showed a superconducting shielding fraction of 80 %. For the $x = 0.18$ batch, we obtained a slightly lower screening fraction, 70 %.

2.2 Cryogenics

In order to study the superconducting phase of Sr$_x$Bi$_2$Se$_3$ ($T_c = 3.0$ K) and PdTe$_2$ ($T_c = 1.6$ K), the Physical Property Measurement System (PPMS, Quantum Design) and the Heliox Vacuum Loading (VL) ^{3}He refrigerator (Oxford instruments) were used.

The PPMS Dynacool allows to perform measurements in the temperature range $T = 1.9$-400 K without the need for any liquid cryogens. The temperature stability is ±0.02 % for T > 20 K and ±0.1 % for $T < 20$ K. The magnetic field in the PPMS Dynacool can be as large as 9 T with a resolution of 0.016 mT. It is produced in the vertical direction (upwards) by a 9 T switch-less superconducting solenoid magnet. With the PPMS Dynacool different types of measurements can be carried out, such as electrical resistivity (with rotator), ac- and dc-susceptibility and ac-calorimetry.

The Heliox is used for measurements that require temperatures below 1.9 K. It can be operated in the temperature range 0.27-100 K. Magnetic fields up to 14 T are generated by a superconducting magnet. The system consists of a single-shot sorption pumped ^{3}He insert and cryostat (providing the vacuum shield, liquid nitrogen shield and liquid ^{4}He bath). The insert is designed to allow the temperature of the sample to be controlled from base temperature to 100 K, using two separate modes of operation. Below the temperature of around 1.5 K (the temperature of the 1 K pot) it runs as a conventional sorption pumped ^{3}He insert, shown in Fig. 2.4. To collect liquid ^{3}He, the 1 K pot is pumped to keep ^{4}He flowing at a certain rate with the needle valve opened slightly. This keeps the temperature of the 1 K pot at 1.5 K. When the sorption pump is heated to 30 K, the absorbed ^{3}He gas is released. Then the ^{3}He gas condenses in the region of the 1 K pot, and is collected in the ^{3}He pot (see Fig. 2.4 left side). This process takes about 30 minutes. To reach the base temperature, the sorption pump is next cooled to 4 K. When cold it starts to absorb ^{3}He and the vapor pressure above the liquid ^{3}He is reduced. A base temperature of 0.27 K is reached in this way (see Fig. 2.4 right side). Coarse control in low temperature is achieved by setting the temperature of the sorption pump to a constant value and thereby setting its pump speed. Above the temperature of 1.5 K, the ^{3}He pot is heated directly. The level of temperature control can be improved by continuously adjusting the heater power by a feedback via a Proportional-Integral-Derivative (PID) controller. All temperature control can be performed by the Intelligent Temperature Controller 503 (ITC 503, Oxford Instruments) with the help of heaters and thermometers:

- On the ^{3}He sorption pump: 1 heater (resistor of 68 Ω at room temperature (RT)) and 1 Allen-Bradley resistance sensor (100 Ω (RT)).
- On the 1 K pot: 1 RuO_2 resistance sensor (2210 Ω (RT), range 1.4∼ 4 K)
- On the ^{3}He pot: 1 heater (2×200 Ω (RT) firerods in series), 1 RuO_2 resistance sensor (2210 Ω (RT), range 0.25∼ 1.5 K with a resolution of 1 mK, field non-sensitive) and 1 Cernox-1050AA sensor (89.7 Ω (RT), range 1.5 ∼ 300 K)

An additional calibrated RuO_2 resistance sensor is mounted on the sample platform which is located 20 cm below the ^{3}He pot in the center of the magnetic field. The Heliox VL ^{3}He refrigerator is a good multi-purpose platform for measurements of the resistivity, ac-susceptibility, thermal expansion, magnetostriction and torque magnetometry.

2.3 Resistivity and susceptibility

Resistivity experiments were carried out at the WZI with a standard four-point contact method. Samples were mounted on a copper holder for good thermal contact between the sample and thermometer on the sample platform. The samples were attached to the holder by GE-Varnish (with cigarette paper as insulating layer) or double-sided sticky tape. Thin copper wires (diameter 30 μm) were used as voltage and current leads which were attached to the sample surface with

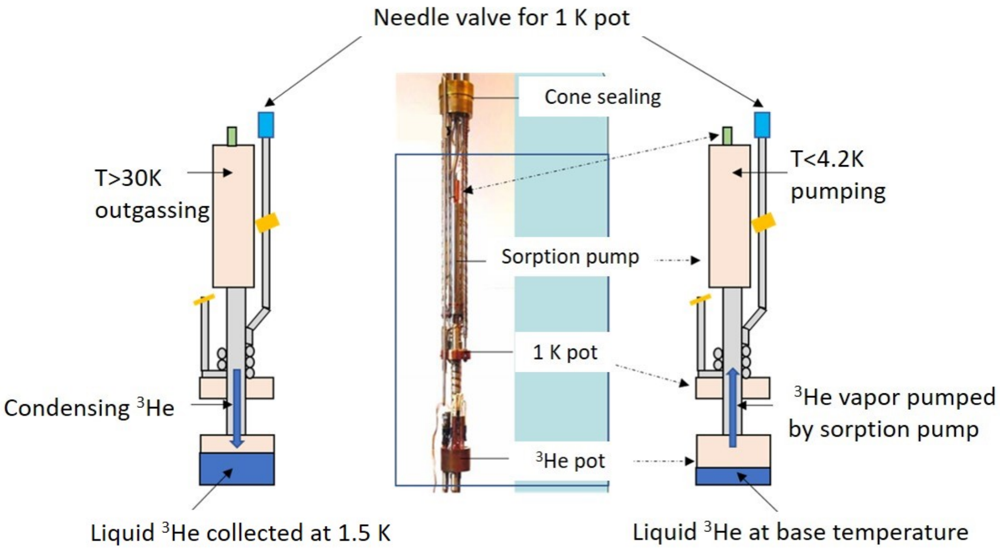

Figure 2.4: Operation principle of a sorption pumped ^{3}He insert. Left: the temperature of the sorption pump is above 30 K, ^{3}He gas is released and condensed by the 1 K pot. Middle: A photograph of the lower part of the Heliox insert. Right: when the temperature of the sorption pump is below 4.2 K, it starts to absorb ^{3}He. The pressure above the liquid ^{3}He is reduced, and a base temperature of 0.27 K is reached. This sketch is taken from Ref. [60].

conductive silver paste. The resistivity signal was collected by a Linear Research AC Resistance Bridge (model LR-700) with an operation frequency $f_{ac} \sim 13$ Hz and an excitation current $I_{exc}\sim$ 30-300 μA.

The ac-susceptibility was measured with the standard mutual inductance method using a home-built coilset in the Heliox and a commercial coilset in the PPMS. In the mutual inductance method, a primary coil is used to generate the driving field. Two identical secondary coils oppositely wound and connected in series pick up the induced voltage. In absence of a sample, the induced voltage due to the driving field should ideally be close to zero. When a sample is inserted in one of the coils, the voltage balance is broken, resulting in an induced voltage that is proportional to the ac-susceptibility of the inserted sample. In the PPMS, the sample is suspended by a sample rod and moved between the two secondary coils. The off balance voltage due to the asymmetry of the two secondary coils can be determined in this way and is subtracted from the recorded signal. This allows to determine the absolute value of the susceptibility. In the Heliox, the sample is at a fixed position in one of the coils (see Fig. 2.5), and the susceptibility signal is not an absolute value but a relative value with off balanced voltage. This value

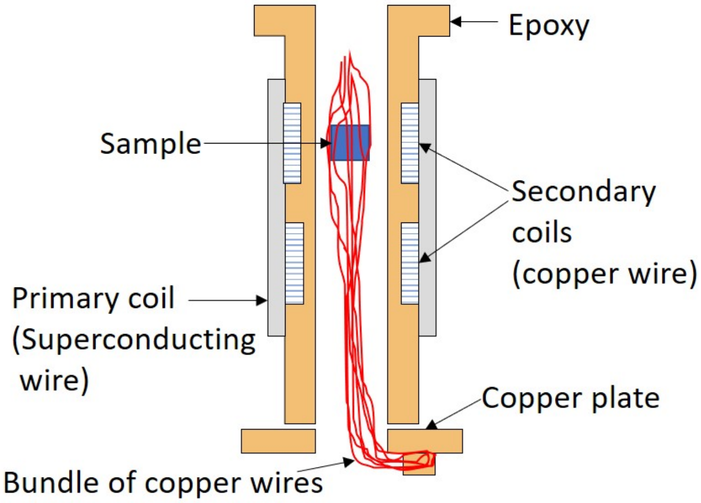

Figure 2.5: A schematic diagram of the mutual-inductance transformer used for ac-susceptibility measurements. This sketch is taken from Ref. [61].

can be calibrated by measuring a sample with known absolute ac-susceptibility. A bundle of copper wires serves for good thermal conductance between the sample and the thermometer at the copper plate (this is the additional calibrated RuO_2 resistance sensor mounted on the sample platform mentioned in the last section). The induced voltage is measured by the LR-700 bridge with $f_{ac}\sim 13$ Hz and I_{exc}~30-300 μA or an EG&G 7265 DSP lock-in amplifier with f_{ac} ~13-13000 Hz and I_{exc} ~20-300 μA.

Part of the dc-magnetization, $M(T,H)$, and ac-susceptibility, $\chi_{ac}(T,H)$, measurements reported in Chapter 4 were performed by Dr. C. Paulsen using a low field SQUID magnetometer developed at the Néel Institute (Grenoble, France). The magnetometer is equipped with a miniature dilution refrigerator making possible absolute value measurements by the extraction technique. A MuMetal and superconducting shield combination results in a residual field of a few milliOersted at the sample position when cooled. As regards χ_{ac}, the in-phase, χ'_{ac}, and out-of-phase, χ''_{ac}, signals were measured in driving fields $\mu_0H_{ac} = 0.0005 - 0.25$ mT with low frequencies $f_{ac} = 2.3 - 13$ Hz.

2.4 Pressure cell technique

Electrical resistance, $R(T,H)$, and ac-susceptibility, $\chi_{ac}(T,H)$, measurements under high-pressure were performed in the Heliox utilizing a clamp-type piston-cylinder cell (height 80 mm and diameter 25 mm), which has a double-layer wall

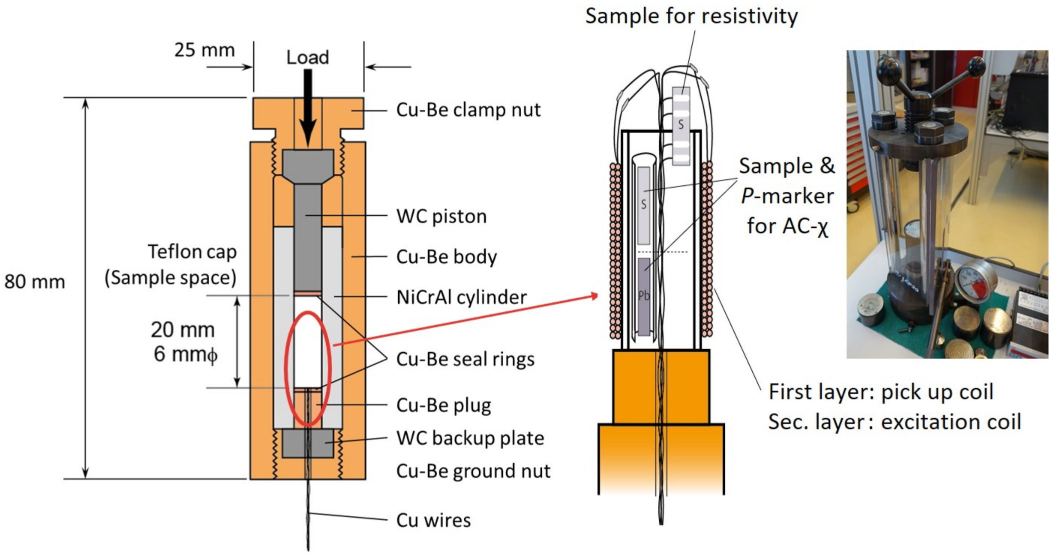

Figure 2.6: Left: a schematic diagram of the clamp-type piston-cylinder cell. Middle: assembly for resistivity and ac-susceptibility measurements mounted on the plug. Right: A photo of the Laboratory Hydraulic Press: LCP20. The schematic diagram is provided by Dr. A. Ohmura.

made of Cu-Be and NiCrAl alloys. Fig. 2.6 shows the cross-section of this cell, where the Cu-Be alloy is orange and NiCrAl is grey. The Cu-Be alloy is used for its hardness, good thermal conductivity and non-magnetic behaviour at low temperatures. The NiCrAl alloy has better mechanical hardness than the Cu-Be alloy, and is used as a cylinder to suppress the expansion that the cell tends to have perpendicular to the compression axis at high pressure. In the sample space a Teflon capsule (height 20 mm, diameter 6 mm) with sample is mounted. However, considering the shrinkage of the sample space after compression, the effective sample space is 4.7 mm in diameter and 8 mm in length. A hand press (Laboratory Hydraulic Press: LCP20 (Unipress), see Fig. 2.6 right side) was used to pressurize the cell via a tungsten carbide (WC) piston, and the pressure is kept with the clamp nut. The pressure is limited to 3 GPa.

Samples were mounted on the plug and loaded into a Teflon capsule together with ac-susceptibility coils and the pressure-transmitting medium. The coilsets for ac-susceptibility were made of 60 μm-diameter Cu wire wound on a cylindrical support of cigarette paper. The Cu wires were taken out of the pressure cell through a hole in the Cu-Be plug (see Fig. 2.6 middle). Here Stycast (2850FT) was used to fill the hole of the Cu-Be plug with Cu wires and seal the cell. We used Daphne oil 7373 for hydrostatic compression [62]. A schematic drawing of the plug with samples and coil is shown in Fig. 2.6. The generated pressure in the capsule relating to each load was estimated from the calibration data for this cell, which was obtained from the pressure variations of the superconducting transition temperatures of lead and tin in previous experiments [63, 64].

2.5 μSR technique

μSR is the acronym for Muon Spin Rotation, Relaxation or Resonance. It is a spin microprobe technique widely used to investigate a variety of static and dynamic phenomena in solid state physics and chemistry, such as superconductivity, magnetism, radical chemistry and many other bulk properties. The principle of the μSR technique is to investigate the local physical environment of implanted muons by measuring the asymmetry function of emitted decay positrons. Positive muons are implanted into a sample and precess around the local field B_μ, with angular frequency $\omega = \gamma_\mu B_\mu$ ($\gamma_\mu = 851.6$ Mrad/(s·T)) is the gyromagnetic ratio). The subsequent asymmetric decay process is monitored by counting the emitted positrons with scintillation detectors placed at opposite directions in the muon-spin precession plane [65, 66]. The μSR technique is made possible by the unique properties of the parity violating decay of pions and muons, and the anisotropic distribution of the decay positrons. In this section, some key elements of the muon and the μSR technique will be discussed. Further details can be found in Ref. [67].

Cosmic rays provide a major source of muons, although at the very low rate of about 100 muons per m^2 every second at sea level. Muons for experiments, with a ten orders of magnitude higher intensity, originate from the decay of pions, which is created in an accelerator by bombarding a light target (graphite) with 600 MeV protons. Charged pions produced with a mean lifetime of 26 ns decay into a muon and a neutrino:

$$\pi^+ \rightarrow \mu^+ + \nu_\mu, \tag{2.1}$$

$$\pi^- \rightarrow \mu^- + \overline{\nu}_\mu. \tag{2.2}$$

The simple two-body decay results in important constraints due to the conservation of momentum and energy. To conserve momentum, the muon and the neutrino must have equal and opposite momentum since pions have no intrinsic angular momentum (S = 0). As only left-handed neutrinos (S = 1/2) are produced in nature (parity violation), the muon has spin S = 1/2 and the beam is around 100 % polarized. In the rest frame of the pion the muons have a unique energy of 4.1 MeV and momentum of 29.79 MeV/c (assuming that the neutrino has a mass $M_\nu = 0$). Either positive or negative muons can be used to perform μSR. In condensed matter physics or chemistry applications almost all μSR research is carried out using positive muons μ^+. In this thesis for simplicity μ^+SR is denoted by μSR.

The intense muon beam sources for experiments are classified into two types: continuous beams (PSI, Switzerland) from a cyclotron and pulsed beams from a synchrotron. Continuous beam (CB) facilities deliver a nearly continuous source of protons used to produce muons that arrive at the experimental stations without any distinct time structure. This means two detectors are necessary to record the arrival time of both muons and the corresponding decay positrons. The use of these two detectors can significantly improve the time resolution of the μSR apparatus. The disadvantage of the CB is the large background in the signal, because consecutive muon decay events must be rejected over a time interval of many muon lifetimes to avoid ambiguity in relating a decay positron to its parent muon [68]. Pulsed beam (PB) facilities deliver intense bunched proton pulses onto the muon production target. The advantage of the PB μSR technique is that the entire incoming muon intensity can be used for measurement and there is almost no background in the signal.

The muons are implanted into a sample and localize at an interstitial site because of their positive charge. The implantation range of the muon depends on its momentum and the mass density of the sample. For typical metallic samples this range is between 0.1 and 1 mm [69]. The implantation and thermalisation process of the muon occurs very rapidly ($\sim$ 1 ns). Depolarization of the muon spin is insignificant in this period. Due to the Larmor precession the muon spin will precess with angular frequency, $\omega = \gamma_\mu B_\mu$. The muon with a mean lifetime of $\tau_\mu \simeq 2.179$ μs decays as follows

$$\mu^+ \ \rightarrow \ e^+ \ + \ \overline{\nu}_\mu \ + \ \nu_\mu. \tag{2.3}$$

This is a three-body decay process in which the kinetic energy of the positron can take values from zero to a maximum $E_{e^+,max} = 52.82$ MeV continuously. To quantify the muon decay the differential positron emission probability per unit of time as a function of the kinetic energy E_{e^+} (or the kinetic energy of the order of $E_{e^+,max}$, $\varepsilon = E_{e^+}/E_{e^+,max}$,) and solid angle Ω is given by [70]

$$\begin{aligned} d\Gamma \ &= \ W(\varepsilon,\theta)d\varepsilon d\Omega \ = \ \frac{1}{4\pi\tau_\mu}2\varepsilon^2(3 \ - \ 2\varepsilon)[1+\frac{2\varepsilon-1}{3-2\varepsilon}\cos\theta]d\varepsilon d\Omega \\ &= \ \frac{1}{4\pi\tau_\mu}E(\varepsilon)[1+a(\varepsilon)\cos\theta]d\varepsilon d\Omega, \end{aligned} \tag{2.4}$$

where θ is the polar angle, ϕ is the azimuthal angle, and $d\Omega = \sin\theta d\theta d\phi$. The energy dependent asymmetry term $a(\varepsilon) = \frac{2\varepsilon-1}{3-2\varepsilon}$ in Eq.2.4 shows the asymmetry dependence of the kinetic energy of the order of $E_{e^+,max}$. The angular distribution $W(\theta)$ of the decay positrons is important for construction of the spatial and temporal distribution of magnetic fields at the muon site. It can be written as

$$W(\theta) \ = \ 1 + a\cos\theta, \tag{2.5}$$

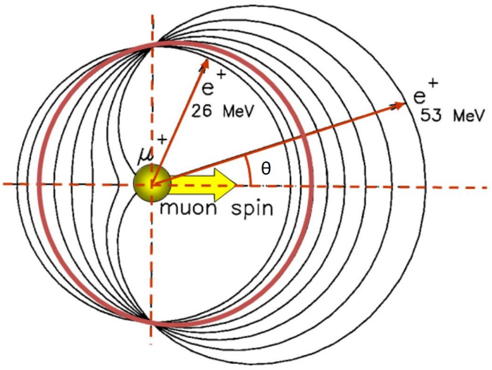

Figure 2.7: Sketch of the angular variation function of the probability $W(\theta)$ for decay positrons with different energy. This sketch is taken from Ref. [71].

where a is the average asymmetry factor. A value of 1/3 can be obtained by integrating the energy dependent asymmetry $a(\varepsilon)$ over all energy with the same efficiency. Fig. 2.7 shows plots of the angular variation function of the probability $W(\theta)$ for decay positrons with different energy. In real measurements, not all positrons in this energy spectrum can be detected, the energy efficiency ϵ is not 1. The initial asymmetry A_0 is therefore of the order of 0.25 to 0.30 and is smaller than 1/3. The positrons with high energy are emitted preferentially along the muon spin direction. This feature makes it possible to obtain the decay positron asymmetry as a function of time by using detectors to record the number of decay positrons.

In the experimental setup the spin rotation can be monitored by using two positron counters mounted on the opposite sides of the sample in the backward (B) and forward (F) directions (see Fig. 2.8). The number of positrons detected by each counter as a function of time is recorded by the two detectors:

$$\begin{aligned} N_B(t) &= N_0 e^{-\frac{t}{\tau_\mu}}[1 + A_0 P(t)] + b_B \\ N_F(t) &= N_0 e^{-\frac{t}{\tau_\mu}}[1 - A_0 P(t)] + b_F, \end{aligned} \tag{2.6}$$

where N_0 is the initial positron count and $b_{B/F}$ is the background value. When deriving Eq. 2.4 and Eq. 2.5, it is assumed that the muon polarization P is 100 % and time independent. In practice, however the muon polarization $P(t)$ is time dependent, and we have the term $P(t)$. More details of $P(t)$ will be discussed in section 3.6.

The signal corresponding to the time evolution of the muon spin polarization can be directly extracted by the asymmetry function $A(t)$, after subtracting the background contribution, determined as the normalized difference of the signals

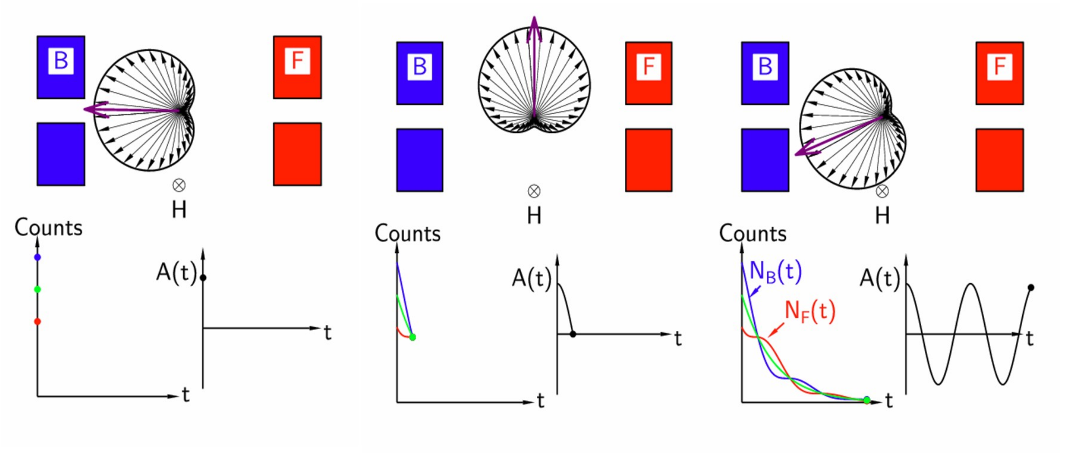

Figure 2.8: Schematic illustration of a transverse field μSR experiment. The magnetic field is directed perpendicular to the plane of the drawing. A spin-polarized beam of muons is implanted in a sample. Upper row: following decay, positrons are detected in the forward detector and in the backward detector. The number of positrons recorded in the forward and backward detectors and the asymmetry function are shown in the second row. This schematic illustration is from Ref. [72].

observed by the two counters,

$$A(t) \equiv A_0 P(t) = \frac{N_B(t) - \alpha N_F(t)}{N_B(t) + \alpha N_F(t)}. \tag{2.7}$$

Here A_0 is the experimentally observable maximum asymmetry, whose value depends on the experimental configuration and α is a calibration constant for correcting the off-balance of the two detectors such as the covered angle. The quantity $A(t)$ (or $P(t)$) contains all the information about the interaction of the muon spin with the local magnetic or spin environment. In the example of Fig. 2.8 the muons are implanted into a sample in a transverse field, *i.e.* an external field perpendicular to the initial direction of the muon spin polarization. The exponential decay can be subtracted from the raw collected histograms and the asymmetry spectrum is obtained. The Fourier transform from the time domain to the frequency domain ($\omega = \gamma_\mu B_{loc}$) allows measurement of the fields experienced by the muons at their stopping site. Furthermore if the sample has different magnetic behaviour regions, the total asymmetry as a function of time will be given by

$$A(t) = \sum A_i(t) P_i(t), \tag{2.8}$$

where i denotes the different magnetic behavior regions which can be distinguished by their specific field distribution. Since the muons are uniformly implanted in a sample, the volume fraction of each region can be obtained by

$$Frac_i = \frac{A_{0,i}}{A_0} = \frac{V_i}{V_{tot}}, \tag{2.9}$$

where $Frac_i$ is the volume fraction of the domain i, $A_0 = \sum A_{0,i}$ is the initially total asymmetry, and V_i and V_{tot} are the volume of the region i and the whole sample, respectively.

In addition to the configuration of transverse field muon spin rotation (TF-μSR), another experimental configuration of μSR technique is longitudinal field muon spin relaxation (LF-μSR) where an external magnetic field is applied parallel to the initial direction of the muon spin polarization. Alternatively, the experiments also can be performed in the absence of an external field, which is called zero field muon spin relaxation (ZF-μSR).

The μSR technique has some unique capabilities in clear advantage [68]. Firstly, the muon is a very sensitive magnetic probe and capable to detect static moments of the order of 0.001 μ_B (~0.1 G), *i.e.* of the order of the nuclear magneton. Secondly, the μSR technique can measure magnetic fluctuation rates in the range 10^4 to 10^{12} Hz, which bridges the gap between fluctuation rates sensed with nuclear magnetic resonance (NMR) and neutron scattering techniques. Thirdly, the μSR technique can be applied in a large variety of environments *e.g.* temperature, high field and high pressure.

All the μSR experiments described in this thesis were carried out with the Multi Purpose Surface Muon Instrument DOLLY installed at the πE1 beamline at the SμS facility of the Paul Scherrer Institute. The positive muon beam used in DOLLY is spin-polarized ($>$ 95 %) with standard momentum 28 MeV/c. Two magnetic field coils are designed to carry out measurements. One is called the main field (WEU) and is directed parallel to the beam with a field range 0-0.49 T. This field configuration is designed for LF-μSR. Another one is named auxillary field (WEV), and is directed perpendicular to the beam with a field range 0-15 mT. The auxillary field is used for TF-μSR.

Chapter 3

Theoretical aspects

In this chapter we discuss the theoretical aspects relevant for this thesis project. First a brief introduction of superconductivity is given, as well as the classification of superconductors. Two characteristic lengths in superconductors are addressed, and the criteria for type I, type II and type II/1 superconductivity are given. Then the typical behavior of both type I and type II superconductors in an applied magnetic field is discussed. Next we discuss the basics of surface superconductivity derived from the Saint James and De Gennes Model. Furthermore, the principle of pressure effects on the critical temperature T_c is presented. In the last part of this chapter we will explain the methodology of the data analysis for the μSR technique.

3.1 Brief introduction of superconductivity

In 1911 the resistance of mercury was observed to reach a value of zero Ohm at the temperature $T = 4.2$ K by Heike Kamerlingh Onnes [73] and the first superconductor was discovered. The transition temperature is defined as the critical temperature T_c. Afterwards another fundamental property of superconductors was found in 1933 by Meissner and Ochsenfeld [74], namely the magnetic field is expelled when cooling to below T_c. This property is named the Meissner-Ochsenfeld effect (Meissner effect).

The first phenomenological theory of superconductivity was put forward by Fritz and Heinz London [75] in 1935 based on the so-called London equation. It directly gives an explanation of the Meissner effect mentioned above. Inspired by the two-fluid model of superfluid ^{4}He, they assumed the superconducting electrons could move without dissipation forming the supercurrent, while the remaining electrons act as the normal electrons with a finite resistivity. Near the surface of the supercondutors supercurrents are flowing which screen the external field from the bulk. A parameter named penetration depth λ is given by the London equation. It is the distance near the surface over which the external field is exponentially reduced to zero. In 1953 the London theory was extended by Pippard [76] who introduced the coherence length (ξ) and put forward a nonlocal generalization of the London equation.

In 1950 another phenomenological theory of superconductivity was proposed by Ginzburg and Landau [77], based on Landau's theory of second order phase transitions [78]. The theory is called the Ginzburg-Landau theory (GL theory). They introduced a complex wave function ψ as the order parameter of the superfluid electrons. The theory was completed by gradually adding new terms, for instance adding spatial variation $\nabla\psi(r)$ for an inhomogeneous system, the magnetic vector potential $\vec{A}$ for the interaction between the magnetic field and the supercurrents, and the complex phase ($\psi(r) = |\psi(r)|e^{i\theta(r)}$) for local gauge invariance and symmetry breaking. Two essential parameters are obtained from this theory. One is the GL coherence length (ξ) for the distance over which the density of superfluid electrons near the surface of the superconductor increases from zero to the bulk value. Another one is the GL parameter $\kappa = \lambda/\xi$ which can be used to distinguish between type I or type II superconductors. The GL theory explains many phenomena in superconductivity, such as flux quantization and the periodic lattice of vortices [79]. Nevertheless it did not explain the microscopic origin of superconductivity.

The first truly microscopic theory of superconductivity was published by Bardeen, Cooper and Schrieffer (BCS) [80] in 1957. The BCS theory was built upon three insights [81]. (1) The interactions between electrons can be attractive in condensed matter rather than repulsive. This was proposed by Fröhlich in 1950 [82]. The attractive interaction between electrons results from coupling between the electrons and the phonons of the crystal lattice. (2) In 1956 Cooper found that two electrons outside an occupied Fermi sea will be paired to a stable state however weak the interaction is, the bound state of the two electrons is called a Cooper-pair [83]. (3) Schrieffer constructed a many-particle wave function where all the electrons near to the Fermi surface are paired up. Based on the many-body wave function, BCS developed the theory for superconducting ground state, the excited quasi-particle states above the energy gap, and the temperature dependence of the gap and the thermodynamic quantities. The original BCS theory gave two famous predictions. One is the correct explanation of the isotope effect $T_c \propto M^{-\alpha}$, where M is the mass of the crystal lattice ions and the isotope exponent α is 1/2. The second one is the existence of an energy gap $2\triangle(0) = 3.52\ k_B T_c$ at the Fermi level [81]. The BCS theory also provided a microscopic foundation for the phenomenological London and Ginzburg-Landau theories of superconductivity.

3.2 Classification of superconductors

Generally superconductors can be classified into two types. They are distinguished by the behavior in an applied magnetic field, which essentially depends on two characteristic length scales, *i.e.* the London penetration depth and the GL coherence length, or their dimensionless ratio κ, the GL parameter. In the following we will first discuss the derivation of these two characteristic lengths, and then illustrate how to distinguish these two types of superconductors. At last type II/1 superconductor will be discussed briefly.

3.2.1 Two characteristic lengths in superconductors

The magnetic penetration depth λ – the London equation

The significance of the penetration depth is the distance over which the applied field penetrating into the superconductor decreases to zero. It results from a phenomenological theory which successfully explains the Meissner effect in superconductors. The London theory relates the supercurrent density $\vec{J_s}$ flowing near the surface to an electromagnetic field $\vec{B}$. Their relation is expressed by [75]

$$\nabla \times \frac{m_e}{n_s e^2} \vec{J_s} + \vec{B} = 0, \tag{3.1}$$

$$\text{or} \qquad \vec{J_s} = -\frac{n_s e^2}{m_e} \vec{A} \tag{3.2}$$

where m_e is the electron mass, n_s is the density of superfluid electrons, e is the electron charge and $\vec{A}$ is the magnetic vector potential with $\vec{B} = \nabla \times \vec{A}$. This equation is the well known London equation. By solving Eq 3.1 for a long superconducting rod with the field applied along the long direction, one obtains

$$B_z(x) = B_0 \exp(-\frac{x}{\lambda}), \tag{3.3}$$

where $B(x = 0) = B_0$ and x is the radial direction. Here λ is the penetration depth defined as

$$\lambda = \sqrt{\frac{m_e}{\mu_0 e^2 n_s}} \tag{3.4}$$

where μ_0 is the vacuum permeability. Clearly flux expulsion does not occur near the surface, an exponential function $B(x)$ is given in Eq. 3.3.

The coherence length ξ – the Ginzburg Landau theory

The GL coherence length characterizes the superconductor by a measure of the distance from the surface over which the density of the superfluid electrons recovers its bulk value. The theory is first set up for a homogenous system where the GL parameters a and b get their constraints. These two parameters are important for the normalization of all parameters throughout the GL theory. Next the theory is extended to an inhomogeneous system where ξ is being defined. For the derivation of the parameters ξ and κ we closely follow Ref. [81].

GL theory is inspired by Landau's theory of second order phase transitions [84]. In the GL theory a complex pseudowave-function $\psi(\vec{r})$ of superfluid electrons was introduced as the order parameter which can be written as

$$\psi(r) = |\psi(r)|e^{i\theta} = \begin{cases} 0 & T > T_c, \\ \psi(r) \neq 0 & T < T_c \end{cases} \tag{3.5}$$

where θ is a phase factor. The free energy density of a superconductor can be expanded in a series:

$$f_s(T) = f_n(T) + a(T)|\psi|^2 + \frac{1}{2}b(T)|\psi|^4 + \cdots. \tag{3.6}$$

Here $f_s(T)$ and $f_n(T)$ are the superconducting state and normal state free energy densities, respectively, and we assume

$$\begin{aligned} a(T) &\approx \dot{a} \times (T - T_c) + \cdots, \\ b(T) &\approx b + \cdots, \end{aligned} \tag{3.7}$$

where $\dot{a} > 0$ and $b > 0$ are constants given by the physical significance of all the parameters. The solution $|\psi|$ for the minimum free energy in terms of the parameters $\dot{a}$ and b is given as

$$|\psi| = \begin{cases} (\frac{\dot{a}}{b})^{1/2}(T_c - T)^{1/2} & T < T_c, \\ 0 & T > T_c. \end{cases} \tag{3.8}$$

The minimum of the free energy in Eq. 3.6 corresponds to the condensation energy of the superconductor. We have

$$f_s(T) - f_n(T) = -\frac{\dot{a}^2(T - T_c)^2}{2b} = -\mu_0 \frac{H_c^2}{2}, \tag{3.9}$$

and the thermodynamic critical field can be derived as

$$H_c = \frac{\dot{a}}{(\mu_0 b)^2}(T_c - T) \tag{3.10}$$

near to T_c.

Next the GL theory of superconductivity will be developed in an inhomogeneous system where the order parameter is position dependent, namely $\nabla\psi(r)$. A new term depending on the gradient of $\psi(r)$ is added to the free energy density. The total energy of this system can be written as

$$F_s(T) = F_n(T) + \int (\frac{\hbar^2}{2m^*}|\nabla\psi(\vec{r})|^2 + a(T)|\psi(\vec{r})|^2 + \frac{1}{2}b(T)|\psi(\vec{r})|^4)d^3r. \tag{3.11}$$

To produce the minimum of the free energy for any arbitrary variation $\delta\psi(\vec{r})$ we have $\delta F_s = 0$. This can only be when $\psi(\vec{r})$ satisfies the Schrödinger-like equation

$$-\frac{\hbar^2}{2m^*}\nabla^2\psi(\vec{r}) + (a(T) + b(T)|\psi(\vec{r})|^2)\psi(\vec{r}) = 0. \tag{3.12}$$

Let us assume the situation of an interface between a normal metal and a superconductor. Suppose that the normal metal is in the $r < 0$ region, the superconductor in the $r > 0$ region and the interface in the yz plane. Therefore we have the boundary condition $\psi(0) = 0$ and the solution of Eq. 3.12 can be obtained as

$$\psi(r) = \psi_0 \tanh\left(\frac{r}{\sqrt{2}|\xi(T)|}\right) \tag{3.13}$$

where ψ_0 is the value of the order parameter in the bulk far from the surface and $\xi(T)$ is the GL coherence length defined by

$$\xi(T) = \left(\frac{\hbar^2}{2m^*|a(T)|}\right)^{1/2} = \left(\frac{\hbar^2}{2m^*|\dot{a}(T - T_c)|}\right)^{1/2}. \tag{3.14}$$

Ginzburg Landau parameter κ

So far we presented the GL model without considering the interactions of the magnetic fields and the currents. For the case of superconductors with supercurrent flowing on the surface, it is required to introduce the vector potential $\vec{A}$ in the free energy function,

$$\begin{aligned} F_s(T) = F_n(T) + \int (\frac{1}{2m^*}|(\frac{\hbar}{i}\nabla + 2\vec{A})\psi|^2 + a|\psi|^2 + \frac{b}{2}|\psi|^4)d^3r \\ + \frac{1}{2\mu_0}\int B(\vec{r})^2 d^3r. \end{aligned} \tag{3.15}$$

Again we can obtain a nonlinear GL-equation by minimizing the free energy, which contains an extra term with the magnetic vector potential $\vec{A}$,

$$-\frac{\hbar^2}{2m^*}(\nabla + \frac{2ei}{\hbar}\vec{A})^2\psi(\vec{r}) + (a(T) + b(T)|\psi(\vec{r})|^2)\psi(\vec{r}) = 0. \tag{3.16}$$

In fact the GL order parameter has both an amplitude and a complex phase (see Eq. 3.5). For a bulk superconductor with a constant order parameter, ψ, there must be a constant magnitude, $|\psi|$, and a fixed phase $\theta(r)$. With these assumptions the supercurrents due to the magnetic field can be obtained from a functional derivative of the free energy

$$\vec{J}_s = -\frac{\partial F_s[\vec{A}]}{\partial \vec{A}(r)} = -\frac{(2e)^2}{2m_e}|\psi|^2\vec{A}. \tag{3.17}$$

The expression Eq. 3.17 is exactly the same as the London equation (Eq. 3.2). The London superfluid density is $n_s = 2|\psi|^2$ and the effective mass in the GL theory is $m^* = 2m_e$. These results correspond to the BCS theory with $|\psi|^2$ representing the density of Cooper pairs in the ground state and n_s the density of the electrons belonging to the Cooper pairs. Furthermore with $n_s = 2|\psi|^2$ and Eq 3.8 the penetration depth in Eq. 3.4 can be rewritten as

$$\lambda(T) = \left(\frac{m_e b}{2\mu_0 e^2 \dot{a}(T_c - T)}\right)^2. \tag{3.18}$$

It is clear that both parameters λ and ξ are temperature dependent and diverge at the critical temperature T_c due to the term $(T_c - T)$ (see Eq. 3.14 and Eq. 3.18). The ratio of these two characteristic lengths defines a new parameter

$$\kappa = \frac{\lambda(T)}{\xi(T)} \tag{3.19}$$

which is temperature independent. It is called the Ginzburg-Landau parameter. κ is a key parameter to distinguish type I and type II superconductors.

3.2.2 Type I and type II superconductors

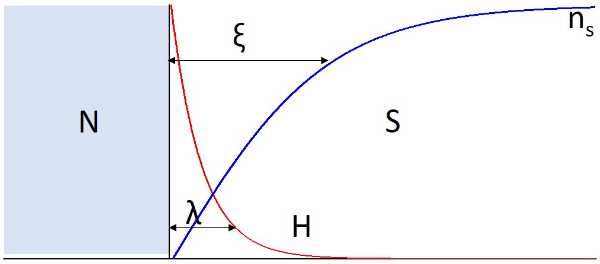

Figure 3.1: Spatial variation of the density of the superfluid electrons n_s and of the applied field H near the interface.

The London equation demonstrated that the applied field can not be completely screened out, it penetrates into the superconductor over a distance of λ (Eq. 3.3). Meanwhile the density of the superfluid electrons $n_s = 2|\psi(r)|^2$ can not disappear abruptly at the interface and must approach zero over a distance of ξ (Eq. 3.13). Let us assume a situation of a domain wall between a normal phase (N) and a superconducting phase (S), and plot both the density of the superfluid electrons n_s and the applied field H_a as a function of the spatial coordinate r as depicted in Fig. 3.1. Due to the presence of the normal state, the superconducting phase, per unit area of interface, gives a positive contribution to the wall energy which is approximately equal to $(\mu_0 H_c^2/2)\xi$ (Eq. 3.6). On the other hand the magnetic field that suppresses the superconducting phase near the interface will result in a reduction of the condensation energy. This loss of energy per unit area is about $(\mu_0 H_c^2/2)\lambda$. Therefore the wall energy E_{dw} can be defined as [85]

$$E_{dw} = \mu_0 \frac{H_c^2}{2}\delta \tag{3.20}$$

where $\delta = \xi - \lambda$ is referred to as the domain wall energy parameter. From Eq. 3.20 we draw the conclusion that for $\xi > \lambda$ the wall energy E_{dw} is positive. The material with $E_{dw} > 0$ in an applied field is classified as a type I superconductors. Conversely for $\xi < \lambda$ the wall energy E_{dw} is negative. Materials with $E_{dw} < 0$ are called type II superconductors. In this case it is energetically more favorable to have a superconducting/normal domain configuration.

A more stringent criteria of this boundary problem is given by Abrikosov. By solving the linearized GL equation he gave the dimensionless ratio κ a value to determine the class of the superconductor [79]. A new type of superconductor was found with a second-order thermodynamic phase transition at a certain critical field H_{c2}. Therefore the magnitude of the GL order parameter $|\psi|$, the magnetization M and the supercurrent J_s for the new type of superconductors obtain small values just below H_{c2} and become zero exactly at H_{c2}. In this case just below H_{c2} the GL equation becomes linearized [81]

$$(-\frac{\hbar^2}{2m^*}\nabla^2 - \hbar\omega_c ix\frac{\partial}{\partial y} + \frac{m^*\omega_c^2}{2}x^2)\psi(\vec{r}) = |a|\psi(\vec{r}) \tag{3.21}$$

where $\omega_c = \frac{2eB}{m^*}$ is the cyclotron frequency. With the well known Landau level solution H_{c2} can be derived as

$$H_{c2} = \frac{2m^*\dot{a}(T_c - T)}{\mu_0\hbar^2}\frac{\hbar}{2e} \tag{3.22}$$

$$= \frac{\Phi_0}{2\pi\mu_0\xi(T)^2}. \tag{3.23}$$

Here $\Phi_0 = h/2e$ is the flux quantum. Note the solution is obtained by assuming a homogenous system where surface states are neglected. H_{c2} is normally referred to as the bulk nucleation field as its physical significance. If we compare the expression of H_{c2} (Eq. 3.22) to the thermodynamic critical field H_c (Eq. 3.10), then we find that

$$H_{c2} = \sqrt{2}\kappa H_c. \tag{3.24}$$

From Eq. 3.24 it is clear that for a superconductor with $\kappa > 1/\sqrt{2}$ we have $H_{c2} > H_c$, and the superconductor is defined as type II. The critical field of a type II superconductor H_{c2} is named the upper critical field. Otherwise for superconductors with $\kappa < 1/\sqrt{2}$ we have $H_{c2} < H_c$, and H_{c2} can not be observed. These are defined as type I superconductors. Therefore type I and II superconductors can be distinguished by

$$\kappa = \frac{\lambda}{\xi}\begin{cases} < \frac{1}{\sqrt{2}} & \text{type I superconductor,} \\ > \frac{1}{\sqrt{2}} & \text{type II superconductor.} \end{cases} \tag{3.25}$$

In fact for type II superconductors there is another critical field H_{c1} which is smaller than H_c, called the lower critical field. We will discuss it in the following section.

3.2.3 Type II/1 superconductors

In the last section we have given the criteria of κ for determining the class of superconductors. In fact there is one more category of marginal superconductors whose

Ginzburg-Landau parameter κ is close to $1/\sqrt{2}$, named type II/1 superconductors. Here we introduce a new parameter, the Ginzburg-Landau-Maki parameter $\kappa_1(T)$ [86] which is used to characterize κ in superconducting alloys and coincides with κ at T_c. κ_1 is temperature dependent and is the key parameter for determining the transition from type I to type II in type II/1 superconductors. In a magnetic field and increasing temperature κ_1 will move from $\kappa_1 < 1/\sqrt{2}$ to $\kappa_1 > 1/\sqrt{2}$, and the superconductor will change from type I to type II [87]. Different from the domain configuration of both type I and type II superconductors, type II/1 superconductors have a typical Meissner mixed state (or intermediate mixed state). This results from an attractive interaction between the flux lines [87]. When the magnetic field is just above the lower critical field, the flux lines attract each other and there is no flux lattice. If the temperature/magnetic field increases to T^*/B^* where $\kappa_1 = 1/\sqrt{2}$, the domain configuration starts following the magnetic behaviour of type II superconductors. A trigonal flux lattice is formed with a lattice parameter d_0, the flux penetrates throughout the sample and the attractive interaction between the flux lines changes to a repulsive one. The state where the mixed state and the Meissner state coexist is the Meissner mixed state (or intermediate mixed state). Here T^*/B^* is referred as the conversion temperature/field. B^* is related to d_0 by [81]

$$B^* = \frac{2\Phi_0}{\sqrt{3}d_0^2}. \tag{3.26}$$

This superconductivity type can be distinguished by specific heat [88, 89] and magnetization measurements [89].

3.3 Type I superconductivity

In Section 1.2.2 we have shown that superconductors with the GL parameter $\kappa < 1/\sqrt{2}$ belong to the group of type I superconductors. H_c is denoted as the critical field of type I superconductors. In the following we will discuss the general properties of the intermediate state that occurs for a finite demagnetization factor N, the calculation of the volume fraction of the superconducting-normal (S-N) domain wall and the differential paramagnetic effect. Lastly, there will be a discussion about demagnetization factors.

3.3.1 Intermediate state

In an ideal case, that is when the applied field is equal to the field near the surface, type I superconductors demonstrate perfect diamagnetism, which is continued until H_c. At H_c superconductivity is suddenly destroyed, since type I superconductors have a first order transition in field (but a second order phase transition when the

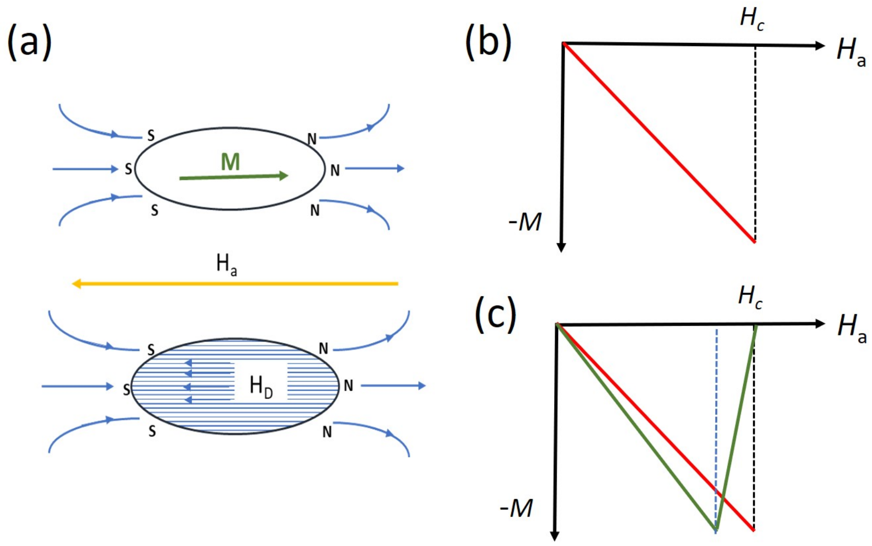

Figure 3.2: (a) Schematic illustration of the demagnetization field H_D generated in a type I superconductor ($N \neq 0$) in magnetic fields. (b) The field dependence of the magnetization in a type I superconductor with $N = 0$.(c) The magnetization in a type I superconductor with $N \neq 0$.

field is zero). This is illustrated in Fig 3.2(b) by the magnetization M as a function of the applied field H_a. We have the magnetic induction B and susceptibility χ as follows

$$B = \mu_0(M + H) = 0 \tag{3.27}$$

$$\chi_M = \frac{dM}{dH}|_{H\to 0} = -1 \tag{3.28}$$

In reality, the existence of a demagnetization field makes matter more complicated, as it gives rise to shape anisotropy in superconductors. Let us assume an ellipsoid ally shaped superconductor is placed in a magnetic field H_a. Then the magnetization will be in the opposite direction as depicted in Fig. 3.2(a). For a magnetized material there will be magnetic poles (north pole (N) and south pole (S)) produced on the surface whose distributions turn itself into another source of magnetic field. This magnetic field produced by surface poles is called the demagnetization field H_D. It has an opposite direction with respect to its parent magnetization. The demagnetization field H_D is related to the magnetization M by $H_D = -NM$, where $0 \leq N \leq 1$ is the demagnetization factor. Therefore the magnetic induction and susceptibility with a finite value N can be written as

$$B = \mu_0(M + H_a + H_D) = 0, \tag{3.29}$$

$$H_a = -(1 - N)M, \tag{3.30}$$

$$\chi_M = \frac{dM}{dH}|_{H\to 0} = -\frac{1}{1-N}. \tag{3.31}$$

From Eq. 3.30 and Eq. 3.31 it is clear that the net magnetization ($M_n = H_a + H_D$) does not correspond to H_a but has a higher value $H_{eff} = H_a/(1 - N)$. Obviously when $H_{eff} < H_c$, *i.e.* $H_a < (1 - N)H_c$, the superconductor will remain in the Meissner state. When the field $H_a > (1-N)H_c$ the sample lowers its free energy by partially allowing penetration of the external field into the interior. Consequently it splits up into normal and superconducting domains (see Fig. 3.3(a)). This domain configuration is called the intermediate state. One point we should keep in mind is that the critical field $H_c(T)$ is the maximum field the superconducting state can support. Once the superconducting state is destroyed, there is no magnetization as well as demagnetization field. Therefore, the magnetic field in the normal domains is always equal to the critical field H_c, whereas in superconducting domains it remains zero (see Fig 3.3(a)).

Calculation of the volume fraction of the domain wall

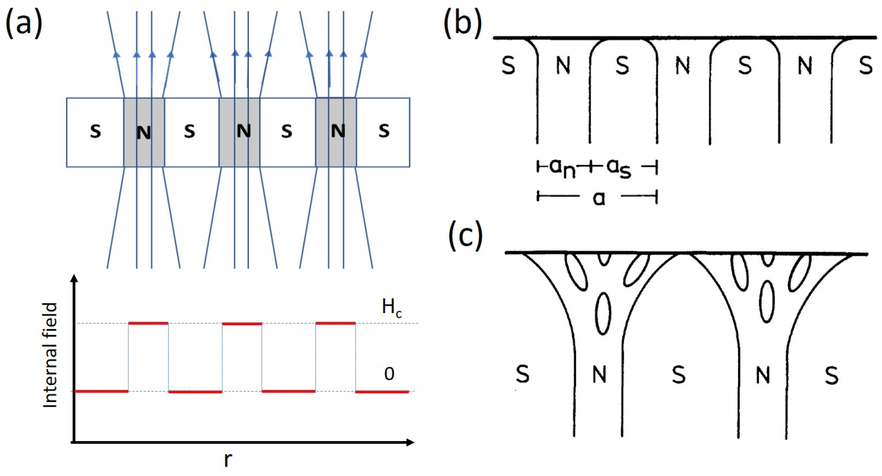

Figure 3.3: (a) Field distribution of the intermediate state in a type I superconductor with demagnetization factor $N \neq 0$. (b) Scheme of the Landau domain structure in the case of (a). (c) Scheme of the Landau branching model in the case of (a). Figures (b) and (c) are taken from Ref. [85].

The volume fraction of the superconducting-normal domain wall is closely related to the superconducting and normal domain pattern. The first theoretical treatment of the domain structure in the intermediate state is given by Landau. In his theory an infinite superconducting plate of thickness $d \gg \lambda$ is placed in a perpendicular magnetic field H_a. The intermediate state is assumed to be a periodic arrangement of superconducting and normal domains (laminar model) [84]. Here the width of the superconducting and normal domains is denoted by a_s and a_n, respectively and the sum of both widths is the periodicity length $a = a_s + a_n$ (see Fig 3.3(b)). Since the volume fraction of the domain walls can be estimated by $f_{dw} = 2\delta/a$, the periodicity length a is the quantity to calculate. An important quantity in determining the periodicity length of the laminar pattern is the energy of the intermediate state, which can be given by [85]

$$F = \mu_0 H_c^2 [\frac{\delta d}{a} + a f(\tilde{h})]. \tag{3.32}$$

Here $f(\tilde{h})$ represents a numerical function of the reduced field $\tilde{h} = H_a/H_c$, Note F is the energy of the intermediate state per unit area. By minimizing the energy F the periodicity length can be obtained [85]

$$a = [\delta \cdot d/f(\tilde{h})]^{1/2}. \tag{3.33}$$

A refinement of this model was later carried out by Landau assuming the branching of the normal domains continuously into smaller portions near the surface (see Fig 3.3). This refined model is called the branching model, while the former one is the nonbranching model. Further it is reported that if the thickness of the sample d is above the critical thickness d_s [90], the branching domain structure is energetically more stable. The Landau branching model yields a new periodicity length a [85],

$$a = [(2\sqrt{2} - 2)^2 \frac{d^2 \delta}{\tilde{h}(1 - \tilde{h}^2)}]^{\frac{1}{3}} \tag{3.34}$$

The branched model contains amounts of branches and corrugations, which can dramatically extend the volume fraction of the domain wall.

Differential paramagnetic effect

The differential paramagnetic effect (DPE) is usually taken as another hallmark of type I superconductivity since it provides information about the Meissner effect and hence the superconducting volume fraction of the sample [91]. The term differential paramagnetic effect comes from the differential susceptibility $(\triangle M/\triangle H)_{H_a}$. Because this differential susceptibility exhibits an excessive paramagnetism, namely a positive peak over a finite range of temperature in an applied field lower than the critical field, the effect is referred to as the differential paramagnetic effect. The DPE is ascribed to the positive $(\triangle M/\triangle H) = N$ in the intermediate state. It is only observable provided the sample has a good Meissner effect, since the intermediate state is closely related to the Meissner effect.

3.3.2 Determination of the demagnetization factor

In practice the demagnetization effect can not be neglected especially when the field is oriented perpendicular to the plane of a thin sample. Therefore an estimate of the demagnetization factor from a theoretical calculation or an experiment becomes important. The value of the demagnetization factor mainly depends on the geometry of the specimen, but also on the susceptibility of the sample.

In the calculations there are three specific values of the susceptibility that are usually taken as constant [92]: $\chi = -1$, corresponding to a superconductor in a perfect diamagnetic state; $\chi \approx 0$, corresponding to a paramagnetic material; and $\chi = \infty$ corresponding to a very soft magnetic state. D.-X. Chen *et al.* [93, 94, 95] presented three papers containing results of the demagnetization factors for a range of susceptibility values as well as different sample geometries. In an experiment the demagnetization factor can be determined by the magnetization curve. In fact Eq. 3.31 shows the susceptibility χ depends on the demagnetization factor N. Additionally, since it is assumed that in the intermediate state the volume fraction of the normal phase f_N changes linearly with increasing external field [96, 97]:

$$f_N(H_a) = \frac{H_a - (1-N)H_c}{NH_c}, \tag{3.35}$$

N also can be derived from the plot of the volume fraction of the normal phase as a function of the external field by $N = (H_c \cdot \frac{df_N}{dH_a})^{-1}$ (see Chapter 6).

3.4 Type II superconductivity

Different from type I superconductors, type II superconductors have $\kappa > 1/\sqrt{2}$, thus a bulk nucleation field $H_{c2} > H_c$. As a consequence for type II superconductors there are two critical fields: 1) H_{c1}, the lower critical field below which the sample stays in the Meissner state $H_{c1} < H_c$; 2) H_{c2}, the upper critical field where superconductivity is suppressed completely. In the field range from H_{c1} to H_{c2} the flux enters the specimen in the form of individual flux lines, each carrying a single flux quantum Φ_0 (see Fig 3.4). The state with flux lines throughout the type II superconductor is called the mixed state. The distribution of the flux lines is mostly in the form of a triangular flux-line lattice [85].

3.4.1 Flux pinning

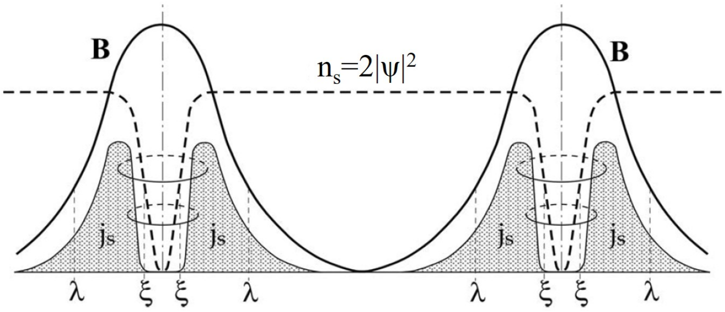

Figure 3.4: Evolution of the field and superconducting order parameter between vortices. The figure is taken from Ref. [92].

In an ideal type II superconductor (N=0, perfect crystal) below H_{c1} the magnetic flux is completely expelled, we have the magnetization $M = -H_a$; at H_{c1} the flux lines start to pass through the sample to form single-quantum vortex lines. This is because the S-N wall energy in a type II superconductor is negative, more vortices with a gradual increase of the field are energetically favorable. In the mixed state the magnetization disappears continuously at H_{c2} showing a second order phase transition. However in a practical type II superconductors the flux lines cannot always move freely, they are pinned by the interactions with defects (pinning centers) which characterizes the microstructure of the specimen [92]. The behaviour of the flux pinning can be explained by the Bean critical state model [98].

3.4.2 Upper critical field-H_{c2}

The upper critical field is the magnetic field where type II superconductivity is completely suppressed and it provides important insights into the Cooper-pair breaking behaviour in the magnetic field. Abrikosov [79] first derived H_{c2} from the GL theory (see Eq. 3.23). Subsequently Gor'kov [99] reported a Green's function reformulation of the microscopic theory of superconductivity (BCS), with which one can derive equations [100] identical in form to those from the GL theory. Afterwards several studies have been made for a more complete theory of H_{c2} by solving the linearized Gor'kov equation with more interactions and constraints.

H_{c2} is predominately effected by the magnetic field via two mechanisms: orbital and spin/paramagnetic effects. The orbital pair breaking is caused by the Lorentz force due to the interaction of the charge motion of the Cooper pair with magnetic fields. The paramagnetic effect is contributed by spin alignment in Cooper pairs driven by magnetic fields [101]. This effect is also explained as Zeeman splitting of spin-singlet Cooper pairs or Pauli pair breaking.

Under the assumption that the interactions between electrons is within the weak coupling BCS model and a spherical Fermi surface, Werthamer, Helfand and Hohenberg (WHH) took account of both orbital [102] and spin [103] effects into the linearized Gor'kov equation to predict the universal behaviour of H_{c2} in superconductors. The relative importance of these two effects for the Cooper-pair breaking behaviour can be scaled by the Maki parameter α, a fitting constant in the WHH model formalism. When $\alpha > 1$ the upper critical field is mainly dominated by the orbital effect, conversely when $\alpha < 1$ it is dominated by the paramagnetic effect [104]. According to the WHH approach [103], the orbital limiting field $B_{orb}(T)$ at $T = 0$ K can be given by

$$B_{orb}(0) = -\zeta T_c (dB_{c2}/dT)|_{T_c}, \tag{3.36}$$

where ζ is a pre-factor for determining the clean limit ($\zeta = 0.69$, $l \gg \xi$, l is the mean free path) and dirty limit ($\zeta = 0.72$, $l \ll \xi$). The Pauli limiting field derived from the Zeeman energy level splitting theory [105] and the BCS gap E_g [106] can be written as

$$B_{Pauli}(0) = 1.86 \times T_c. \tag{3.37}$$

With the condition $F_s = F_n$ the upper critical field can be obtained as

$$B_{c2}(0) = \frac{B_{orb}(0)}{\sqrt{1+\alpha}} \tag{3.38}$$

and the Maki parameter is [104]

$$\alpha = \sqrt{2} B_{orb}(0)/B_{Pauli}(0). \tag{3.39}$$

3.5 Saint James and De Gennes Model-H_{c3}

In Section 1.2.2 we have derived the nucleation field in the bulk $H_{c2} = \sqrt{2}\kappa H_c$ (Eq. 3.24). This result is derived under the assumption that the specimen is an infinite superconductor where the effect of the surface can be neglected. Practically a surface represents an inhomogeneous system. The nucleation field on the surface is expected to be higher than the one in the interior of the bulk (H_{c2}) in a decreasing field. Saint James and De Gennes [107] gave a quantitative treatment of this nucleation problem. It is assumed the surface is electrically insulating and the field applied parallel to the surface is reduced from a value higher than Maximum$\{H_{c2}, H_c\}$. By solving the linearized GL equation (Eq. 3.21) with specific constraints, they have shown that during a reduction of the applied field the superconducting state was first generated in a surface layer of thickness $\sim \xi(T)$. This occurs at a field $H_{c3} = 2.4\kappa H_c = 1.69 H_{c2}$ where H_{c3} is the surface critical field. Therefore $\kappa = 0.42$ presents a boundary value where above the surface state can be observed. The relation following regions can be given

$$\begin{cases} \kappa < 0.42 & \text{type I superconductor, } H_{c3} \text{ not observed,} \\ 0.42 < \kappa < 1/\sqrt{2} & \text{type I superconductor, } H_{c3} \text{ observed,} \\ \kappa > 1/\sqrt{2} & \text{type II superconductor, } H_{c3} \text{ observed.} \end{cases} \tag{3.40}$$

Later the angular dependence of the surface nucleation field was studied [108, 109]. The measured values of the nucleation field H_θ as a function of the angle θ between the field direction and the plane of the thin sample was reported as

$$\left(\frac{H_\theta \cos\theta}{H_{c\|}}\right)^2 + \frac{H_\theta \sin\theta}{H_{c\perp}} = 1 \tag{3.41}$$

where $H_{c\|} = H_{c3}$ is the nucleation field in the direction of the field parallel with the surface and $H_{c\perp} = H_{c2}$ perpendicular with the surface. This effect may explain some apparent measurement discrepancies of the transition field between magnetization measurements (determining H_{c2}) and resistivity measurements (determining H_θ).

3.6 The principle of the pressure effect on T_c

High pressure has been shown to be a clean and powerful technique for generating novel physical states, and is particularly effective in tuning the superconducting transition temperature T_c [110, 111]. T_c can be tuned by changing the principal parameters, such as the electronic density of states at the Fermi level $N(E_F)$, the characteristic phonon frequency ω_D (Debye frequency) and the electron-phonon coupling constant λ_{e-p}. Moreover, in a few superconductors pressure-induced changes of the Fermi surface topology also have an effect on T_c [112, 113]. The application of the external pressure tunes the related physical properties by directly changing the distance of the atoms in the crystal lattice. Since the atoms are concentrated under pressure, the overlap of the wavefunctions of the neighboring atoms is strengthened. As a consequence the overlap integral is enhanced which leads to a higher degree of delocalization of the electrons, a broadening of the electronic bands and sometimes a modification of the crystal structure [114].

The superconducting transition temperature T_c can be estimated based on microscopic theories of phonon-mediated superconductivity such as the weak-coupling BCS model [106] or the Eliashberg model of strong-coupling superconductivity [115].

According to the weak-coupling ($\lambda_{e-p} < 1$) BCS theory T_c is expressed by [106]

$$T_c \approx 1.13 \frac{\hbar\omega_D}{k_B} \exp(-\frac{1}{\lambda_{e-p}}), \tag{3.42}$$

where k_B and $\hbar$ are Boltzmann's and Planck's constant, respectively, and $\lambda_{e-p} = N(E_F)V_{eff}$ where V_{eff} is the effective attractive interaction between the electrons mediated by the phonons. Generally the transition temperature is observed to decrease under pressure. As we know commonly ω_D increases with pressure, then from Eq. 3.42 the decrease of T_c must be attributed to λ_{e-p}. The electrons density of states is expected to reduce under pressure due to the pressure-induced band broadening effect [111]. But the pressure dependence of $N(E_F)$ can be very different, and it also depends on the details and the topology of the Fermi surface in the particular compound. The pressure dependence of V_{eff} is more difficult to estimate, a microscopic treatment of the coupled system of electrons and phonons is required.

For superconductors with an intermediate to strong electron-phonon coupling ($\lambda_{e-p} \geq 1$), the pseudopotential treatment of the screened Coulomb interaction is induced. The T_c can be derived from the Allen-Dynes-modified McMillan equation [116, 117]

$$k_B T_c = \frac{\hbar < \omega >}{1.2} \exp(-\frac{1.04(1 + \lambda_{e-p})}{\lambda_{e-p} - \mu^* - 0.62\lambda_{e-p}\mu^*}), \tag{3.43}$$

where μ^* is the Coulomb pseudopotential which is given by [118]

$$\mu^* = \frac{N(E_F)V_c}{1 + N(E_F)V_c \ln \frac{E_B}{\hbar\omega_0}} \tag{3.44}$$

V_c is the matrix element of the screened Coulomb interaction averaged over the Fermi surface, E_B is the electronic bandwidth and ω_0 is the maximum phonon frequency. The electron-phonon coupling constant λ_{e-p} can be obtained by [118]

$$\lambda_{e-p} = 2 \int \frac{\alpha^2(\omega)F(\omega)}{\omega} d\omega = \frac{N(E_F) < I^2 >}{M < \omega^2 >}. \tag{3.45}$$

$\alpha(\omega)$ is the strength of an average electron-phonon interaction and $F(\omega)$ is the phonon density of states. The displacement of an atom induces a change of the crystal potential where $< I^2 >$ is the average over the Fermi surface of the square of the electronic matrix element. M stands for the atomic mass. $< \omega^n >$ in Eq. 3.43 (n=1), and Eq. 3.45 (n=2), is the n-th moment of the normalized weight function: [111]

$$< \omega^n > = \frac{2}{\lambda_{e-p}} \int d\omega \alpha^2(\omega) F(\omega) \omega^{n-1} \tag{3.46}$$

Apparently the pressure dependence of T_c is more complex. It can be reduced to two parameters, the density of the states $N(E_F)$ and the average phonon energy $< \omega >$ (or $< \omega^2 >$) since the pressure effects on μ^* and $< I^2 >$ are frequently neglected [111]. Eq. 3.43 is generally used to derive $T_c(P)$ from first principle calculations of the pressure effect on the band structure and the phonon spectrum.

3.7 The principle of μSR

In section 2.5 several key features of the muon and the μSR technique have been discussed. We know the quantity $A(t)$ (or $P(t)$) contains all the information about the spatial and temporal distribution of the magnetic fields at the muon site. In this section, the muon depolarization function $A(t)$ (or $P(t)$) in different experimental configurations (*i.e.* ZF and TF) will be discussed. The time evolution of the muon spin polarization is defined as

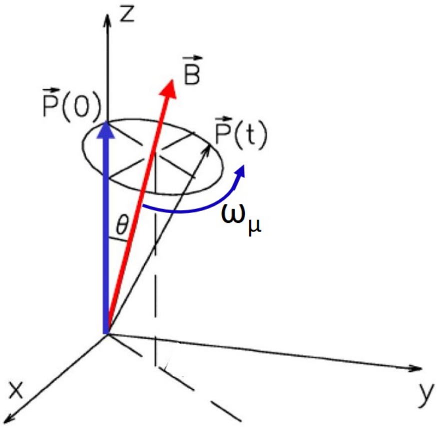

Figure 3.5: Muon spin precession in a constant field ($\vec{B}$). The initial polarization is along the z-axis, which is also the observation direction. This sketch is taken from Ref. [67].

$$P(t) = \frac{\langle \vec{I}(t) \cdot \vec{I}(0) \rangle}{|\vec{I}(0)|^2}, \tag{3.47}$$

where $\vec{I}(t)$ is the beam intensity at time t. Assume a muon ensemble is implanted into a sample at a constant field. Then the time polarization in a specific magnetic field along the initial muon spin direction will be

$$\begin{aligned} P(t) = P_z(t) \equiv P_{\vec{B}}(t) &= P_z(0)[\frac{{B_z}^2}{B^2} + \frac{{B_x}^2 + {B_y}^2}{B^2} cos(\gamma_\mu B t)] \\ &= P_z(0)[\cos^2\theta + \sin^2\theta \cos(\omega_\mu t)]. \end{aligned} \tag{3.48}$$

Here $P_z(0)$ is the initial polarization, θ is the polar angle and ω_μ is the angular frequency the muon processes with (see Fig. 3.5). If the field distribution $p(B)$ in the domain probed by the muon ensemble is given, the corresponding polarization function can be determined as:

$$P_z(t) = \frac{\int P_{\vec{B}}(t) p(\vec{B}) d^3B}{\int p(\vec{B}) d^3B}. \tag{3.49}$$

From Eq. 3.48 and Eq. 3.49 the muon spin polarization in several special cases can be deduced. Generally both Gaussian and Lorentzian distribution are used to describe the field distribution. In this thesis we only discuss the muon spin polarization function with Gaussian field distribution in static field which we used in the experimental data analysis. Furthermore we restrict ourselves to ZF and TF geometries. More details can be found in Ref. [67].

3.7.1 Zero field μSR

In a zero field μSR experiment the time dependence of the polarization of the muons in a sample can be measured under the action of internal magnetic fields. These local fields can be a result of either electronic origin (for instance spontaneous magnetization) or the nuclear moments. Both will be discussed in the following section.

Internal field from spontaneous magnetization

In the simplest case that the field from the spontaneous magnetization in a single crystal is in a given direction θ (*e.g.* ferromagnetic or antiferromagnetic materials), the muon polarization can be depicted as:

$$P_z(t) = \cos^2\theta + \sin^2\theta \cos(\omega_\mu t), \tag{3.50}$$

where $\cos^2\theta$ is called the static term, and $\sin^2\theta\cos(\omega_\mu t)$ is the oscillating term. In an ideally polycrystal or powder sample, the value of the internal field is constant and the direction is isotropically distributed. In this case:

$$P(t) = \frac{1}{4\pi}\int (\cos^2\theta + \sin^2\theta\cos(\omega_\mu t)) d(cos\theta) d\phi = \frac{1}{3} + \frac{2}{3}\cos(\gamma_\mu B_\mu t), \tag{3.51}$$

where ϕ is the azimuthal angle. As we mentioned the internal field is randomly and isotropically distributed. Therefore the 1/3 and 2/3 components can be qualitatively understood by assuming about 1/3 is parallel or antiparallel to the initial muon spin direction and about 2/3 is perpendicular.

Note in Eq. 3.51 it is assumed that all muons probe the same constant field. However in a real crystal the magnetic field structure always has some disorder with a distribution of the fields around a mean $\langle B_\mu \rangle$. If we assume the distribution is Gaussian, we have

$$p(B) = \frac{1}{\sqrt{2\pi\langle \Delta B^2 \rangle}} exp[-\frac{(B - \langle B_\mu \rangle)^2}{2\langle \Delta B^2 \rangle}], \tag{3.52}$$

where $\langle \Delta B^2 \rangle$ is the second moment of the distribution

$$\langle \Delta B^2 \rangle = \int (B - \langle B_\mu \rangle)^2 p(B) dB. \tag{3.53}$$

If we introduce the Gaussian field distribution Eq. 3.52 and Eq. 3.50 into Eq. 3.49, and integrate for the time dependence of the polarization, we obtain

$$\begin{aligned} P_z(t) &= \frac{1}{3} + \frac{2}{3}\cos(\gamma_\mu \langle B_\mu \rangle t) exp[-\frac{1}{2}{\gamma_\mu}^2 \langle \Delta B^2 \rangle t^2] \\ &= \frac{1}{3} + \frac{2}{3}\cos(\gamma_\mu \langle B_\mu \rangle t) exp[-\frac{\sigma^2 t^2}{2}], \end{aligned} \tag{3.54}$$

where we define the depolarization rate $\sigma = \sqrt{{\gamma_\mu}^2 \langle \Delta B^2 \rangle}$.

Internal field from nuclear moment

As we discussed in section 2.5, the muon is a very sensitive magnetic probe and capable to detect magnetic moments of the order of the nuclear magneton. Here we will discuss the time dependence of the muon polarization due to nuclear moments at zero field. A Gaussian distribution of fields can be obtained in the case of a dense arrangement of randomly oriented nuclear moments.

If a field distribution at the muon site is centred around zero and the field is distributed in the x, y and z direction we have

$$\begin{aligned} &\langle B_i \rangle = 0 \qquad\qquad i = x, y, z \\ &\langle \Delta B_i^2 \rangle = \rangle (B_i - \langle B_i \rangle)^2 = \langle B_i^2 \rangle - \langle B_i \rangle^2 = \langle B_i^2 \rangle = \frac{\sigma^2}{\gamma_\mu^2}. \end{aligned} \tag{3.55}$$

For the direction i ($i = x, y, z$), a Gaussian field distribution occurs with

$$p(B_i) = \frac{1}{\sqrt{2\pi\langle \Delta B^2 \rangle}} exp[-\frac{B_i^2}{2\langle \Delta B_i^2 \rangle}], \tag{3.56}$$

where $\langle \Delta B_i^2 \rangle$ is the second moment of the field distribution along each direction. Then we have

$$p(\vec{B}) = p(B_x)p(B_y)p(B_z) = \frac{p(|\vec{B}|)}{4\pi B^2}. \tag{3.57}$$

The distribution function for the absolute value of the field is given by the Maxwell distribution

$$p(|\vec{B}|) = \frac{1}{\sqrt{(2\pi\langle B_i^2\rangle)^3}} 4\pi B^2 exp[-\frac{B^2}{2\langle B_i^2\rangle}]. \tag{3.58}$$

Here again, we use Eq. 3.50 and introduce the Maxwell field distribution Eq. 3.58 into Eq. 3.49 for the time dependence of the polarization. We get [119]

$$\begin{aligned} P_z(t) &= \frac{1}{3} + \frac{2}{3}(1 - \gamma_\mu^2\langle B_i^2\rangle t^2) exp[-\frac{1}{2}\gamma_\mu^2\langle B_i^2\rangle t^2] \\ &= \frac{1}{3} + \frac{2}{3}(1 - \sigma^2 t^2) exp[-\frac{\sigma^2 t^2}{2}], \end{aligned} \tag{3.59}$$

where again we define $\sigma^2 = \gamma_\mu^2\langle B_i^2\rangle$. This function is the well-known Kubo-Toyabe relaxation function. And the 1/3 and 2/3 components again can be qualitatively understood by assuming about 1/3 is parallel to the initial muon spin direction and about 2/3 is perpendicular.

3.7.2 Transverse field μSR

In the transverse field configuration the external magnetic field is applied perpendicular to the initial muon polarization (the z direction). With Eq. 3.50 and $\theta = 90°$, we can rewrite the time dependence of the polarization with external field as

$$P_z^x(t) = \cos(\gamma_\mu B_{ext} t). \tag{3.60}$$

Here it is assumed that the external field is along the x direction. Then the Gaussian field distribution in the x direction is modified to:

$$p(B_{ext}) = \frac{\gamma_\mu}{\sqrt{2\pi}\sigma} exp(-\frac{\gamma_\mu^2(B_{ext} - B_x)^2}{2\sigma^2}). \tag{3.61}$$

Since $|\vec{B}_{ext}| \gg \frac{\sigma}{\gamma_\mu}$, the applied field is much larger than the internal field broadening. Therefore only the applied field in the x-direction comes into play, and we can write

$$\begin{aligned} P(t, B_{ext}) &= \int P_z^x(t) p(B_{ext}) dB_{ext} \\ &= \frac{\gamma_\mu}{\sqrt{2\pi}\sigma} \int exp(-\frac{\gamma_\mu^2(B_{ext} - B_x)^2}{2\sigma^2}) cos(\gamma_\mu B_{ext}) dB_{ext} \\ &= \cos(\gamma_\mu B_{ext} t) exp[-\frac{1}{2}\gamma_\mu^2\langle\Delta B_{ext}^2\rangle t^2], \end{aligned} \tag{3.62}$$

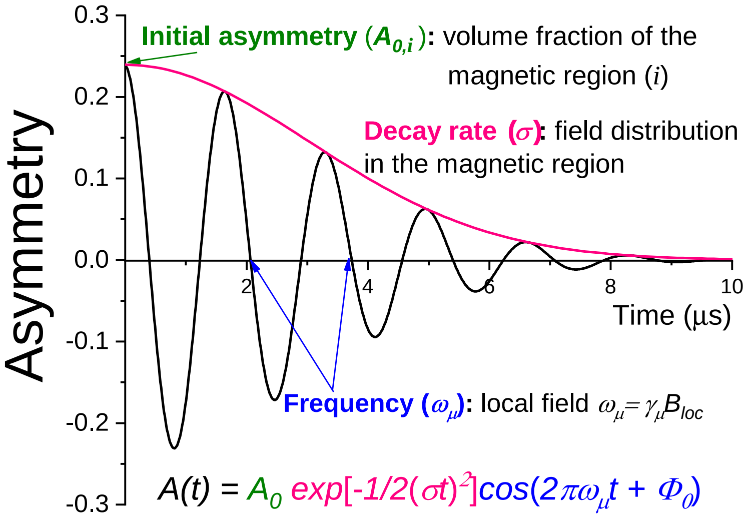

Figure 3.6: Schematic illustration of the information the function $A(t)$ contains about the spatial and temporal distribution of the magnetic fields at the muon site.

where we again define $\sigma = \sqrt{\gamma_\mu^2 \langle \Delta B_{ext}^2 \rangle}$. Then we can write the time evolution of the polarization for a Gaussian broadening as

$$P(t, B_{ext}) = \cos(\gamma_\mu B_{ext} t) exp(-\frac{\sigma^2 t^2}{2}). \tag{3.63}$$

In Eq. 3.63, the oscillation frequency gives the external field and the damping rate gives a direct measure of the second moment of the field distribution (see Fig. 3.6). Additionally as we discussed in section 2.5, the volume fraction in a certain magnetic region ($Frac_i$) can be obtained by the formula $Frac_i = A_{0,i}/\sum A_{0,i}$. Generally it is assumed that the average field sensed by the muon is the external field B_{ext}. In fact, the external field does not always play the role of the average field. It can be modified in some specific cases, *i.e.* for a type I superconductor the shape of the sample will play a role through the demagnetization factor (see Chapter 6). In addition, for a type II superconductor when determining the penetration depth by μSR, the field probed by the muons will be modified by the so-called vortex lattice (see Chapter 7).

Chapter 4

Type I superconductivity in the Dirac semimetal $PdTe_2$

The superconductor $PdTe_2$ *was recently classified as a type II Dirac semimetal, and advocated to be an improved platform for topological superconductivity. Here we report dc-magnetization, ac-susceptibility and transport measurements conducted to determine the nature of the superconducting condensate. Surprisingly, we find that* $PdTe_2$ *is a conventional type I superconductor with* $T_c = 1.64$ *K and a critical field* $\mu H_c(0) = 13.6$ *mT. Our crystals also show the intermediate state as demonstrated by the differential paramagnetic effect in the ac-susceptibility. For fields exceeding* H_c *we observe additional superconducting screening signals below 1.3 K that can be related to surface superconductivity.*

This chapter has been published as Phys. Rev. B 96, 220506(R) (2017).

4.1 Introduction

Recently the transition metal dichalcogenide PdTe$_2$ was reported to be a type II Dirac semimetal [120, 121, 122]. Topological Dirac semimetals form a new class of topological materials, where non-trivial surface states arise due to the topology of the bulk band structure (for recent reviews see [123, 124, 125]). Dirac semimetals are the 3D analog of graphene and have a cone-shaped linear energy dispersion around the Dirac point with massless fermions [126]. The bands have a double degeneracy that can be lifted by a magnetic field resulting in a pair of Dirac cones. In the closely related class of Weyl semimetals the degeneracy is naturally lifted by breaking time reversal and/or inversion symmetry [127]. The set of Dirac cones can give rise to distinct properties, such as Fermi arcs at the surface, quantum anomalous Hall effect and chiral magnetotransport [124, 125]. Type I Dirac semimetals are like graphene and the valence and conduction bands meet at the Dirac point and Lorentz invariance is obeyed. In type II Dirac semimetals an extra momentum dependent term in the Hamiltonian breaks Lorentz invariance [128, 129, 130]. This can be accomplished by tilting the Dirac cone, where the Dirac point is now the touching point of the electron and hole pockets. This gives rise to a number of new physical phenomena, such as an angle dependent chiral anomaly and topological Lifshitz transitions [124, 125].

Superconductivity in PdTe$_2$ with a transition temperature T_c of 1.5 K was discovered in 1961 [131]. The recent detection of topological features in the band structure raises the question whether superconductivity has also a topological nature [120, 121, 132]. Notably, it has been advocated that PdTe$_2$ is an improved platform for topological superconductivity [121]. Topological superconductors attract much attention because they are predicted to host protected Majorana zero modes at their surface (for recent reviews see [133, 134]). This offers a unique design route to produce future devices for topological quantum computation. Unfortunately, the number of materials in which topological superconductivity has been realized - or is under debate - is very small [134]. Majorana modes, that appear as gapless nodes in the bulk superconducting gap, are in general not stable in a Type I Dirac semimetal [134]. However, in a type II semimetal the situation is different because of the tilted dispersion. Moreover, the abundancy of states in the electron and hole pockets near the type II Dirac point favours a larger carrier concentration and superconductivity [121].

Hitherto, the superconducting state of PdTe$_2$ has not been studied in detail. The early determination of T_c by Guggenheim *et al.* [131] was confirmed by others with T_c values ranging from 1.7 to 2.0 K [121, 135, 136, 137]. Fei *et al.* [121] investigated the depression of T_c in magnetic field and reported an anomalous upward curvature of the upper critical field $H_{c2}(T)$ with $\mu_0 H_{c2} = 0.32$ T for $T \to 0$. In view of the proposed topological nature of the superconducting state [121, 120, 132] an in depth characterization of the superconducting phase is a matter of great urgency. Here we report magnetic and transport measurements on single crystals that unambiguously show $PdTe_2$ is a type I superconductor. This makes $PdTe_2$ the first topological material where superconductivity is of type I. This is a surprising results, also because the number of known binary and ternary systems with type I superconductivity is very small (see for instance Refs. [138, 139, 140] and references therein). Our crystals also show enhanced superconductivity of the surface sheath in fields exceeding the critical field H_c. The surface superconductivity does not obey the standard Saint-James-de Gennes behavior with critical field $H_{c3} = 1.69 \times H_c$ [141]. We discuss these unusual results in view of the presence of topological surface states [120, 132].

$PdTe_2$ crystallizes in the trigonal CdI_2 structure (space group P$\bar{3}$m1) [142]. It belongs to the family of transition metal dichalcogenides, which is intensively studied because of the remarkable physical properties [143]. Its normal-state electronic properties have been investigated in the 1970s by quantum oscillation experiments and band structure calculations [144, 145, 146]. The topological nature of the electronic band structure was reported recently [121, 120, 132]. Notable angle resolved photoemission spectroscopy (ARPES) combined with *ab initio* band structure revealed $PdTe_2$ is a type II Dirac semimetal [120], which finds further support in a non-trivial Berry phase originating from a hole pocket formed by a tilted Dirac cone [121]. The fundamental electronic properties of $PdTe_2$ were revisited recently by transport, magnetic and thermal measurements [147].

4.2 Experimental

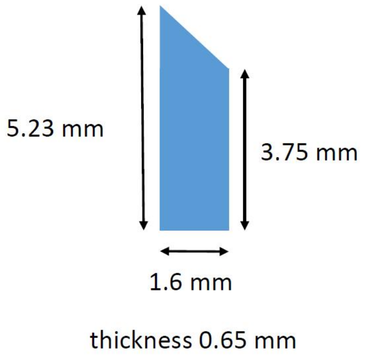

Figure 4.1: Dimensions and shape of the $PdTe_2$ single crystal s2

For our study of the superconducting properties of $PdTe_2$ we prepared a single crystal by a modified Bridgeman technique [59]. Powder X-ray diffraction confirmed the CdI$_2$ structure. Scanning Electron Microscopy (SEM) with Energy Dispersive X-ray (EDX) spectroscopy showed the proper 1:2 stoichiometry within the experimental resolution of 0.5 % (see Chapter 3.1). Laue back-scattering was used to orient the crystal. Single crystalline bars, typically a few mm long, were cut along the crystallographic a-axis by means of a scalpel blade and/or spark erosion. Standard four-point resistance measurements were carried out in a Physical Property Measurement System (Quantum Design) at temperatures down to 2 K and in a helium-3 refrigerator (Heliox, Oxford Instruments) down to 0.3 K. Dc-magnetization, $M(T,H)$, and ac-susceptibility, $\chi_{ac}(T,H)$, measurements were made using a low field SQUID magnetometer developed at the Néel Institute. The magnetometer is equipped with a miniature dilution refrigerator making possible absolute value measurements by the extraction technique. A MuMetal and superconducting shield combination results in a residual field of a few milliOersted at the sample position when cooled. As regards χ_{ac}, the in-phase, χ'_{ac}, and out-of-phase, χ''_{ac}, signals were measured in driving fields $\mu_0 H_{ac} = 0.0005 - 0.25$ mT with low frequencies $f_{ac} = 2.3 - 13$ Hz. The dimensions and shape of the PdTe$_2$ crystal used for the magnetization measurements are reported in Fig. 4.1. The magnetic field was applied along the long direction (a-axis). In order to estimate the demagnetization factor, N, we approximated the shape by a bar with dimensions 4.4×1.6×0.65 mm^3 (shown in Fig. 4.1). We calculate N = 0.10 [148].

4.3 Results and analysis

4.3.1 Type I superconductivity in PdTe$_2$

In Fig. 4.2 we show the dc-magnetization as a function of the applied field H_a in the temperature range $0.31 - 1.50$ K. The $M(H_a)$-curves follow the behavior of a Type I superconductor with a Meissner phase up to $\mu_0 H_a = 12$ mT and the intermediate state for $12 < \mu_0 H_c < 13.6$ mT, where H_c is the critical field. The large value of the measured initial slope $\chi_m = dM/dH_a = \chi/(1+N\chi) = -1.13$ is in agreement with bulk superconductivity. Here N is the demagnetization factor and $\chi = -1$ the ideal susceptibility [149]. From the initial slope we calculate $N = 0.12$ which is close to the estimated value ~ 0.10 based on the sample shape (see Fig. 4.1). We remark the rounding of the curves is due to the non-uniform magnetization at the sample edges. However, a clear kink and tail is observed in the data just above H_c (see inset). We will return to this point later. We have determined $H_c(T)$ by extrapolating the idealized linear $M(H_a)$-curves to $M = 0$, as shown by the dash-dotted line for $T = 0.31$ K in Fig. 4.2. The critical field follows the standard BCS quadratic temparature variation $H_c(T) = H_c(0)[1 - (T/T_c)^2]$, with $\mu_0 H_c = 13.6$ mT and $T_c = 1.64$ K, see Fig. 4.7.

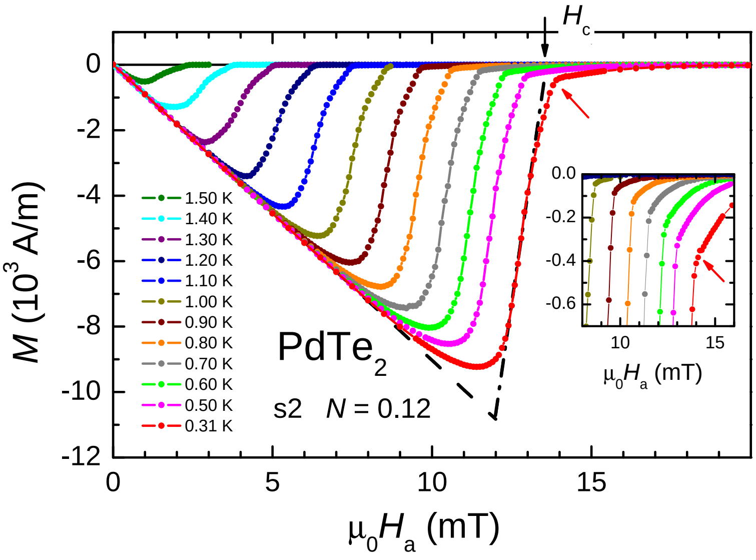

Figure 4.2: Dc-magnetization per unit volume (S.I. units) as a function of applied field for PdTe$_2$ at temperatures from 0.31 K (right) to 1.50 K (left) as indicated. The initial slope $\chi_m = dM/dH_a$ accounts for a superconducting sample volume of 100 % with $N = 0.12$ (dashed line). The dash-dotted line indicates the idealized $M(H_a)$-curve with slope $1/N$ in the intermediate state at $T = 0.31$ K. The black arrow indicates H_c at $T = 0.31$ K. The red arrow points to a kink and start of a tail in $M(H_a)$. Inset: Zoom of the kink-feature at a few selected temperatures.

The temperature variation of the dc-susceptibility, $\chi_{dc}(T)$, in applied fields ≤ 10 mT is shown in Fig. 4.3. The data are taken after cooling in zero field (ZFC) and field cooled (FC). The FC data at low applied dc-fields ($\mu_0 H_a = 1$ mT) demonstrate a large Meissner effect with a flux expulsion of 93 %. Ac-susceptibility measurements in an ac-driving field $\mu_0 H_{ac} = 0.25$ mT for dc-fields up to 10 mT are reported in Fig. 4.4 a,b. At low temperatures χ'_{ac} shows a full superconducting screening signal. Upon increasing the temperature χ'_{ac} does not show the usual smooth increase to zero. Instead the signal becomes positive and shows a large peak before the normal state is reached at T_c. This is known as the differential paramagnetic effect (DPE) [150]. It results from the positive $\partial M/\partial H_a$ below H_c in the intermediate state (see Fig. 4.2), *i.e.* in between $(1 - N)H_c$ and H_c, and has been observed in other type I superconductors as well [138, 140]. $H_c(T)$-data points extracted from the dc and ac-susceptibility data in fixed fields have been collected in Fig. 4.7 as well.

The dc-magnetization, the ac-susceptibility with DPE and the extracted T^2-variation of H_c, all provide solid evidence PdTe$_2$ is a type I superconductor. This tells us the Ginzburg-Landau parameter $\kappa = \lambda/\xi < 1/\sqrt{2}$. An estimate for the

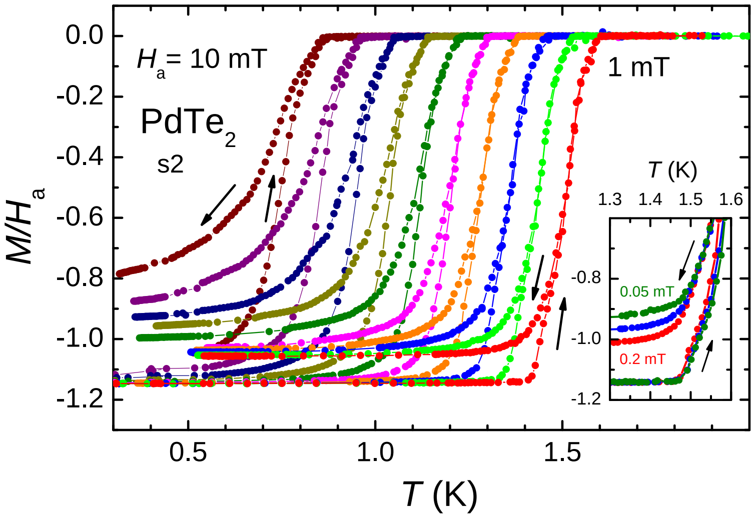

Figure 4.3: Dc-susceptibility, M/H_a, in S.I. units, as a function of temperature in fields $\mu_0 H_a$ from 1 mT (right) to 10 mT (left) in steps of 1 mT. Data are taken after cooling in zero field (ZFC) and field cooled (FC) as shown by the arrows. Inset: Part of the ZFC-FC curves in applied fields of 0.2 (red), 0.1 (blue) and 0.05 mT (green).

magnetic penetration depth, λ, can be obtained using the London equation $\lambda = (m^*/\mu_0 n_s e^2)^{1/2}$, where m^* is the effective mass, n_s the superfluid density and e the elementary charge. With a carrier density $n = 5.5 \times 10^{27}$ m^{-3} determined by Hall effect measurements on our crystals, and $m^* \approx 0.3 m_e$ [145, 137] (here we use an average value m^* and m_e is the free electron mass) we calculate $\lambda \sim 39$ nm. A value for the superconducting coherence length, ξ, can be derived from the Ginzburg-Landau relation $\xi = \Phi_0/(2\sqrt{2}\pi\mu_0 H_c \lambda)$ [151], here Φ_0 is the flux quantum. With the measured value $H_c(0) = 13.6$ mT we obtain $\xi \approx 439$ nm, and calculate $\kappa \approx 0.09$. We remark that realistic errors margins in the values of n and m^* will not affect the result $\kappa < 1/\sqrt{2}$. Since $-\mu_0 H_c^2/2$ is the condensation energy per unit volume we can use thermodynamic relations to calculate H_c from the step-size of the specific heat at T_c using the relation $\Delta C|_{T_c} = 4\mu_0 H_c(0)^2/T_c = 1.43 \times \gamma T_c$ [149], assuming PdTe$_2$ is a weak coupling BCS superconductor [152]. Here γ is the Sommerfeld coefficient. With the experimental value $\gamma = 138$ J/K^{2}m^3 [147, 152] (the molar volume is 4.34×10^{-5} m^3/mol), we calculate $\mu_0 H_c(0) = 12.6$ mT, which is close to the measured value reported in Fig. 4.7.

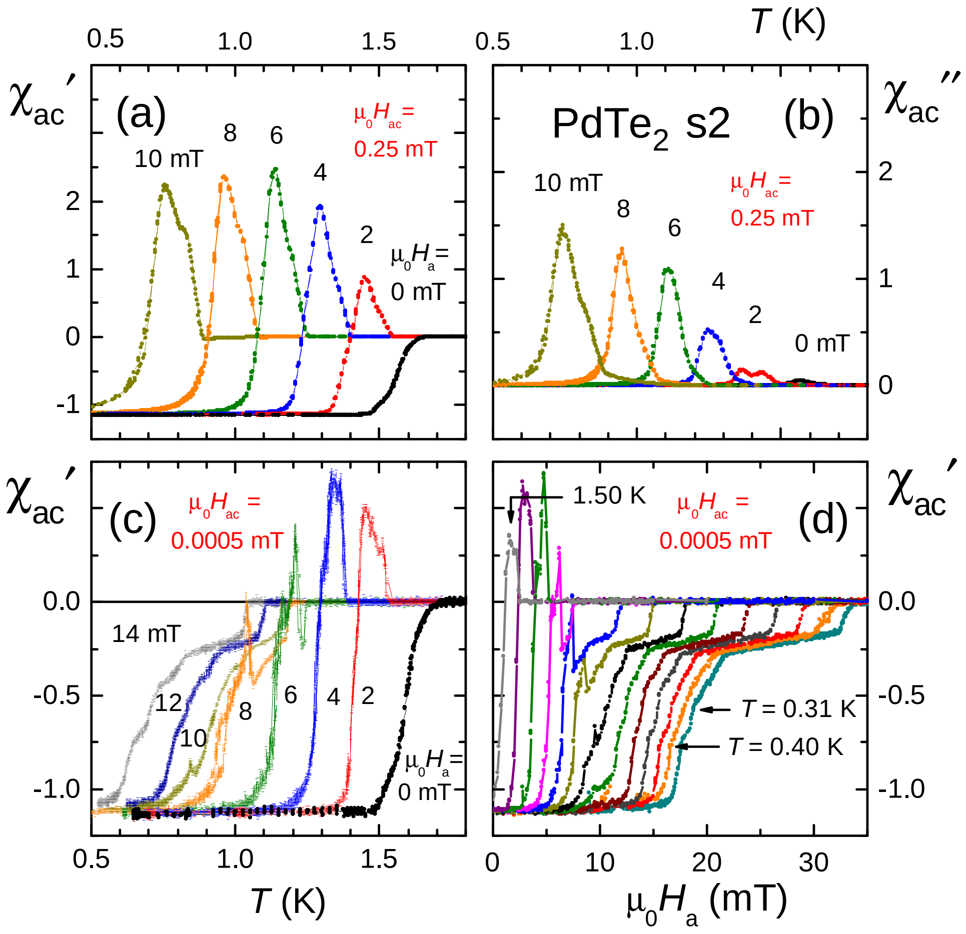

Figure 4.4: Ac-susceptibility of PdTe$_2$. Upper panels (a) and (b): In phase and out-of-phase component of the ac-susceptibility for an ac-driving field $\mu_0 H_{ac} = 0.25$ mT. Data are taken in dc fields $\mu_0 H_a = 0 - 10$ mT, as indicated. The large peaks in χ'_{ac} when a dc field is applied are due to the differential paramagnetic effect. Lower panels: Ac-susceptibility in a small ac-driving field $\mu_0 H_{ac} = 0.0005$ mT. Panel (c): As a function of temperature at dc-fields from 0 to 14 mT as indicated. Panel (d): As a function of applied field at a temperature of 0.31 K, and from 0.40 K to 1.50 K in steps of 0.1 K.

4.3.2 Superconductivity of the surface sheath

Having established that PdTe$_2$ is a bulk type I superconductor, we next turn to superconductivity of the surface sheath. A close inspection of the $M(H)$ isotherms reported in Fig. 4.2 reveals a clear kink in the data close to H_c and a long tail for $M(H) \to 0$ (see inset). Thus superconductivity survives above H_c. This is also most clearly observed in the ac-susceptibility data measured in a small driving field $\mu_0 H_{ac} = 0.0005$ mT reported in Fig. 4.4(c)(d). For small fields ($\mu_0 H_a \leq 4$ mT) the $\chi'_{ac}(T)$-data (panel c) show the same behavior as reported in Fig. 4.4(a) ($\mu_0 H_{ac} = 0.25$ mT). However, for $\mu_0 H_a \geq 6$ mT the DPE peak progressively reduces and screening persists even for fields exceeding H_c. The $\chi'_{ac}(H_a)$-data (panel d) show that at the lowest temperature (0.31 K) screening of the full superconducting volume takes place till ~ 17 mT. By further increasing H_a the screened volume is reduced in a step-wise fashion, until finally at 33 mT the diamagnetic signal disappears completely. Since the $\chi'_{ac}(T, H_a)$-data show a full screening signal above H_c this signal must come from the superconducting surface layer. This also explains why the large peak due to the DPE located just below H_c becomes smaller and smaller with increasing applied field (panel c) or decreasing temperature (panel d): the bulk is screened by the surface layer [153].

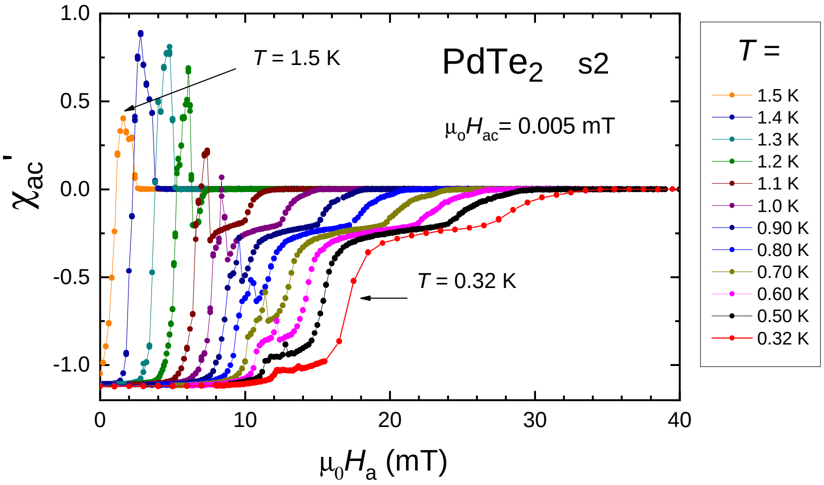

Figure 4.5: Ac-susceptibility of PdTe$_2$ (crystal s2) as a function of the applied field, H_a, in a driving fields $\mu_0 H_{ac} = 0.005$ mT at temperatures in the range $T = 0.32 - 1.5$ K as indicated. Here H_{ac} is 10× larger than in Fig.4.4(d).

The screening efficacy of the surface layer strongly depends on the amplitude of H_{ac}. In Fig. 4.4(a) $\mu_0 H_{ac} = 0.25$ mT and the screening is weak, while in Fig. 4.4(c) $\mu_0 H_{ac} = 0.0005$ mT and the screening is large. In Fig. 4.5 we show the field variation $\chi_{ac}(H_a)$ for $\mu_0 H_{ac} = 0.005$ mT at different temperatures. Here the driving field is 10 times larger than H_{ac} used to take the data presented in Fig. 4.4(d). The weaker screening in Fig. 4.5 is obvious and the DPE peak remains visible even at the lowest temperature. In Fig. 4.6 we show the low frequency ac-susceptibility of PdTe$_2$ (crystal s2) at $T = 0.60$ K as a function of applied field, H_a, measured for 5 different amplitudes of the ac-driving field, H_{ac}. For the largest amplitude, $\mu_0 H_{ac} = 0.25$ mT, the peak due to the differential paramagnetic effect (DPE) below H_c is very pronounced. For fields $H_a > H_c$ (0.6K) = 12 mT a diamagnetic signal is still visible. Upon reducing the amplitude of H_{ac} the extra diamagnetic signal grows progressively and screens the peak due to the DPE more and more. For the lowest amplitude of the ac-driving field, $\mu_0 H_{ac} = 0.0005$ mT, the DPE peak is completely screened and a full screening signal (100 % sample volume) persists till 14 mT. This can only be caused by superconductivity of the surface layer (which is present already above H_c). For higher applied fields flux penetrates the crystal in a step-wise fashion, which indicates an intricate flux pinning process at the surface. Flux penetrates more easily when the amplitude of H_{ac} is increased. From our ac-susceptibility study we conclude that superconductivity of the surface layer accompanies bulk superconductivity. The efficacy of the surface layer to pin flux strongly depends on the amplitude of the ac-driving field, and is already strongly reduced for $\mu_0 H_{ac} = 0.25$ mT. It also tells us flux pinning in the surface sheath is extremely weak and can be overcome by a driving field of typically 0.25 mT. The weak pinning at the surface of the crystal also explains why the FC dc-susceptibility measured in very small dc-fields ≤ 0.2 mT shows less flux expulsion than for fields ≥ 1.0 mT (see inset Fig. 4.3).

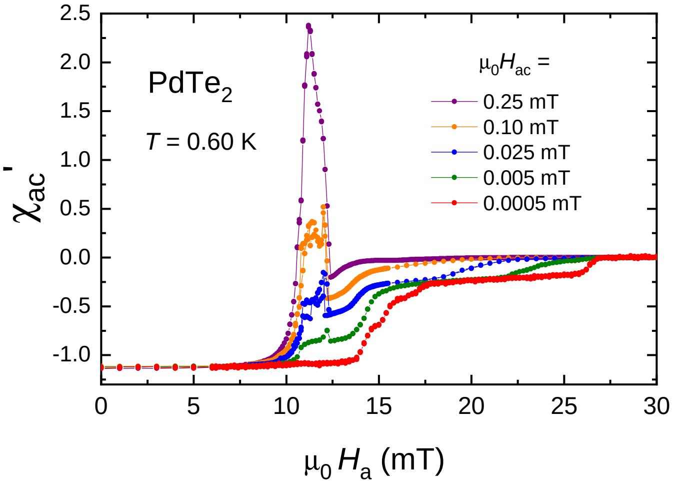

Figure 4.6: Ac-susceptibility of $PdTe_2$ (crystal s2) at $T = 0.60$ K as a function of the applied field, H_a, in driving fields, $\mu_0 H_{ac}$, ranging from 0.0005 mT to 0.25 mT as indicated.

4.3.3 Superconducting phase diagram

Next we present the superconducting phase diagram derived from the magnetic and transport measurements (Fig. 4.7). Superconductivity of the bulk is found below

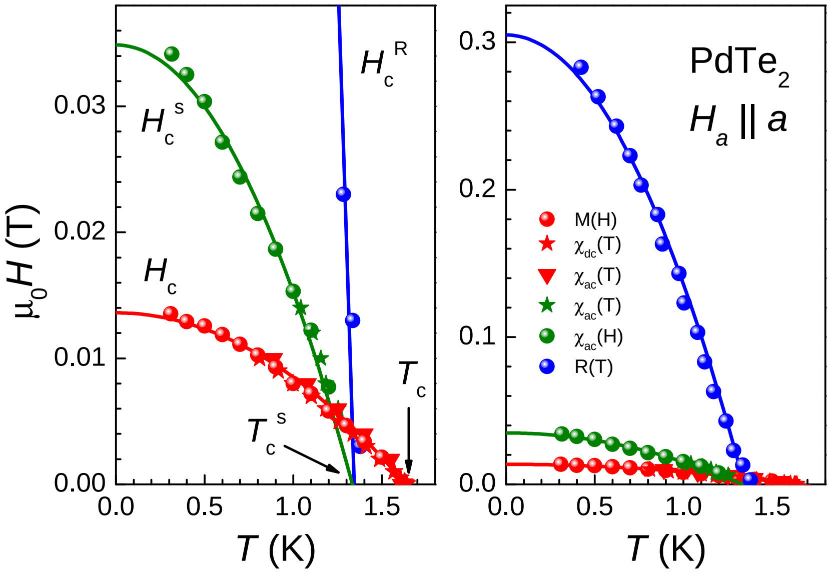

Figure 4.7: Superconducting phase diagram of PdTe$_2$ for $H_a \parallel a$-axis. Bulk superconductivity is found below $H_c(T)$ as determined by dc-magnetization and χ'_{ac}. The red line represents a fit to $H_c(T) = H_c(0)[1-(T/T_c)^2]$, with $\mu_0 H_c(0) =$ 13.6 mT and $T_c = 1.64$ K. Surface superconductivity is found below $H_c^s(T)$ as determined by χ'_{ac} for a small amplitude of H_{ac} (see text). The green line represents a fit to $H_c^s(T) = H_c^s(0)[1-(T/T_c^s)^2]$, with $\mu_0 H_c^s(0) = 34.9$ mT and T_c^s =1.33 K. The blue symbols denote $H_c^R(T)$ and are taken from the superconducting transition measured by resistance. The blue line compares $H_c^R(T)$ with the WHH model curve (see text).

the H_c-phase line. The critical field of the surface layer $H_c^s(T)$ is identified from the data in Fig. 4.4c,d by the field ($> H_c$) at which $\chi'_{ac}(H)$ or $\chi'_{ac}(T)$ reaches zero. We remark that for the small amplitude ac-field, $\mu_0 H_{ac} = 0.0005$ mT, $H_c^s(T)$ is well defined due to the step-like feature when $\chi'_{ac} \to 0$. For larger amplitudes of H_{ac} the step broadens. Obviously, $H_c^s(T)$ does not follow the standard relation for surface superconductivity $H_{c3} = 1.69 \times H_c$ [141]. Moreover, the extrapolation of $H_c^s(T)$ to $H \to 0$ reveals T_c^s of the surface layer is 1.33 K, which is lower than the bulk T_c (see Fig. 4.7). Here we fitted $H_c^s(T)$ to a quadratic temperature function, from which we infer $\mu_0 H_c^s(0) = 34.9$ mT. Remarkably, electrical resistance measurements for $H_a \parallel a$ on the same PdTe$_2$ crystal reveal superconductivity survives up to fields that are almost a factor 10 higher (see the right panel in Fig. 4.7 for details). The critical field determined by transport, $H_c^R(T)$, tracks the $H_c(T)$ curve for low fields, but increases rapidly below $\sim$ 1.3 K. This temperature coincides, within the error bar, with T_c^s, which strongly suggests the transport experiment probes superconductivity of the surface layer as well. The $H_c^R(T)$-curve compares quite well with the standard Werthamer-Helfand-Hohenberg (WHH) expression for a weak-coupling spin-singlet superconductor in the clean limit [154].

4.4 Discussion and conclusion

The phase diagram with type I superconductivity below $T_c = 1.64$ K and surface superconductivity below $T_c^s = 1.33$ K is at odds with the standard BCS behavior, but we stress it is a robust property of our $PdTe_2$ crystals. We have performed a number of checks. First of all SEM and EDX showed our crystals to have a homogeneous 1:2 composition and no foreign phases were detected (see Chapter 3). Secondly, and most importantly, after taking the M and χ'_{ac} data we carefully polished the surfaces of the crystal and remeasured the magnetic properties with essentially the same results for the bulk and surface. This provides compelling evidence surface superconductivity is not due to an impurity phase on the surface. We emphasize the large critical field $H_c^R(T)$ measured by resistance is a robust property of our crystals as well (see Appendix). Resistance measurements for $B \parallel a^*$- and c-axis on the same crystal, as well as on other crystals, all show similarly enhanced values of $H_c^R(T)$. The close to isotropic behavior for $B \parallel a$-, a^*- and c-axis indicates the superconducting transition in resistance is not due to filamentary superconductivity. Finally, we remark that Fei *et al.* [121] reported a large critical field ~ 0.32 T for $T \to 0$ deduced from resistance data too.

The unusual superconducting phase diagram of $PdTe_2$ shows some similarities with the diagrams reported for the Type I superconductors AuBe [155] and $LaRhSi_3$ [140]. For these materials also a surface critical field much larger than H_c is found. However, in both case it was attributed to a field induced change from type I to type II/1 superconductivity below a conversion temperature $T^* < T_c$, which is possible when κ is close to $1/\sqrt{2}$ [156]. We remark that for $PdTe_2$ $\kappa = 0.09 < 1/\sqrt{2}$ and we did not find any evidence for a conversion from Type I to Type II/1. On the other hand, both $LaRhSi_3$ and AuBe have a noncentrosymmetric crystal structure. Theory predicts the lack of inversion symmetry can possibly give rise to exotic superconducting properties due to the mixing of spin-singlet and triplet order parameters [157], as well as to unusual surface states. This possibly explains the measured critical fields are much larger than H_c.

The structure of superconducting states in Dirac semimetals was recently investigated by theoretical work [121, 158, 159, 160]. Depending on the different pairing potentials, topological odd-parity superconductivity in the bulk with gap nodes is a possibility. Since we find that $PdTe_2$ is a conventional BCS superconductor, such a scenario is most likely ruled out. On the other hand, ARPES measurements in the normal state reveal the presence of a topological surface state [120, 132]. Possibly, a superconducting gap opens in this topological surface state at T_c^s, below T_c of the bulk. Since, superconductivity of the surface layer, with two critical fields H_c^s and H_c^R, does not follow the standard BCS behavior, we speculate it could have a topological nature. This calls for an in depth examination of superconductivity in $PdTe_2$, by *e.g.* scanning tunneling probe techniques.

In summary, we have investigated the superconducting properties of the compound $PdTe_2$ that was recently reported to be a type II Dirac semimetal. Dc-magnetization and ac-susceptibility measurements clearly show $PdTe_2$ is a type I superconductor with $T_c = 1.64$ K and a critical field $\mu_0 H_c(0) = 13.6$ mT. Our crystals also show the intermediate state as is demonstrated by the differential paramagnetic effect observed in the ac-susceptibility. In addition, superconductivity of the surface layer is found below $T_c^s = 1.33$ K $< T_c$. It persists up to $\mu_0 H_c^s(0) = 34.9$ mT and does not follow the standard Saint-James-de Gennes behavior. Resistance data point to an even larger critical field for the surface layer $H_c^R(0) \approx 0.30$ T. $PdTe_2$ is the only topological material with type I superconductivity has been reported so far. This, together with the unusual superconducting phase diagram, calls for a close examination of superconductivity in $PdTe_2$, especially in view of the existence of topological surface states.

4.5 Appendix

4.5.1 Superconductivity measured by resistance

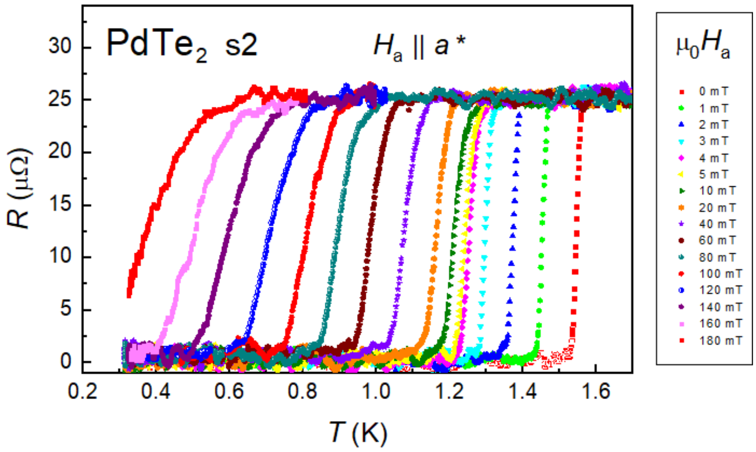

Figure 4.8: Temperature variation of the resistance of $PdTe_2$ measured in fixed applied magnetic fields $H_a \parallel a^*$ as indicated.

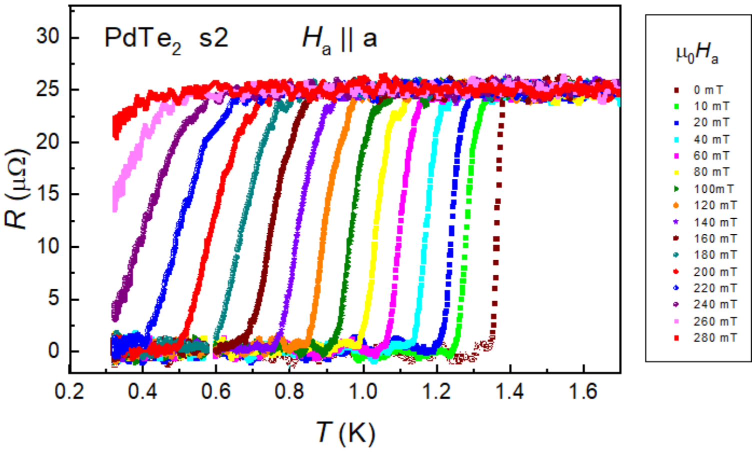

Figure 4.9: Temperature variation of the resistance of PdTe$_2$ in fixed fields $H_a \parallel a$ as indicated. We remark, in this experiment the field values are not corrected for the small remanent field of about 3 mT present in the superconducting magnet.

The depression of superconductivity in PdTe$_2$ was studied by measuring the resistance, $R(T)$, in fixed magnetic fields applied along the a-, a^*- and c-axis. Data for $H_a \parallel$ a are taken in the longitudinal configuration ($H_a \parallel I$), while data for $H_a \parallel a^*$ and $H_a \parallel c$ are taken in the transverse configuration ($H_a \perp$ I). In Figs. 4.8 and 4.9 we present the data for $H_a \parallel a^*$ and $H_a \parallel a$, respectively. Since the critical field for the Type I superconducting phase is low ($H_c = 13.6$ mT for $T \rightarrow 0$), special care was taken to reduce the remanent field in the superconducting magnet to close to zero (by reversing the field polarity while sweeping the field to zero) in the experiment for $H_a \parallel a^*$. The data for $H_a \parallel a^*$ show a sharp superconducting transition in the low field range (up to 4 mT), i.e. when the phase boundary of Type I superconductivity is probed (see inset Fig. 4.10). In higher applied fields the transition broadens gradually and superconductivity is depressed less rapidly. The measured $R(T)$-curves for $H_a \parallel c$ (not shown) are comparable to the ones for $H_a \parallel$ a. The field-depression of superconductivity was also measured on two other crystals with similar results.

By collecting the transition temperatures measured at fixed fields in the $H_a - T$ plane we construct the superconducting phase diagram determined by resistance shown in Fig. 4.10. Here we use the onset T_c for superconductivity. We remark that by defining T_c as the midpoint of the transition or at $R = 0$ the T_c values will be reduced to some degree, but this will not affect the main features of the diagram. In very low fields (up to 4 mT) we observe the depression of the bulk Type I superconducting phase (see inset in the left panel). However, superconductivity survives up to much larger fields. For $H_a \parallel a$ we find a critical field $\mu_0 H_c^R \approx 0.3$ T for $T \rightarrow 0$. We attribute the $R = 0$ state for fields exceeding 4 mT to supercon-

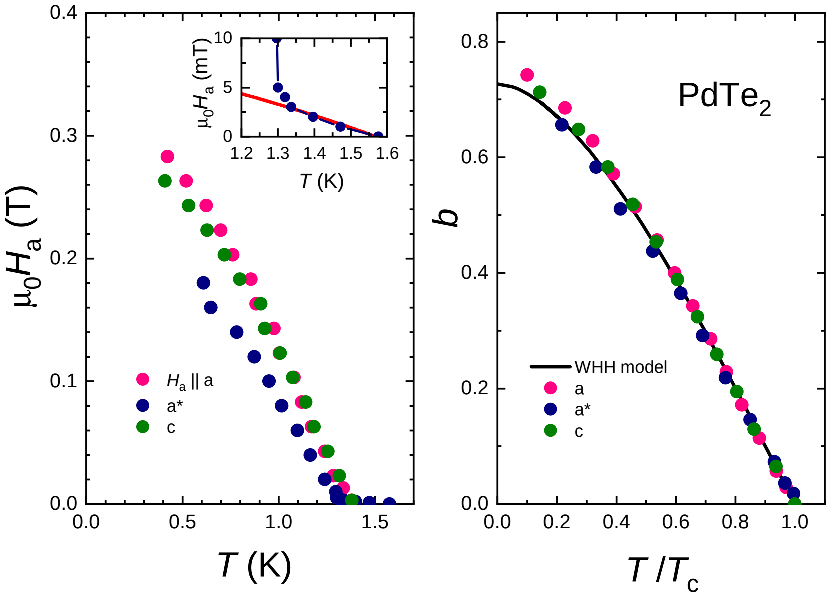

Figure 4.10: Left panel: Field-temperature phase diagram of superconductivity in PdTe$_2$ (crystal s2) measured by resistance. Data points are taken from T_{conset} in the $R(T)$-curves measured at fixed fields. The inset shows low-field data for $H_a \parallel a^*$ that initially follow the T^2-variation of H_c(T) (red line). Right panel: Reduced critical field, $b = H_c^R(T)/[-(dH_c^R/dT)|_{T_c} \times T_c]$ as a function of the reduced temperature T/T_c. The data are compared to the WHH model curve (black line).

ductivity of the surface. The H_c^R(T)-curves are remarkably isotropic with respect to the direction of the magnetic field. This rules out a scenario of filamentary superconductivity with filaments in the planes of the layered material. In this case one expects to observe a large anisotropy of H_c^R(T) for a field along and perpendicular to the c-axis. The presence of filaments perpendicular to the layer direction is highly unlikely. In the right panel of Fig. 4.10 we have traced the $H_c^R(T)$-data in a "universal" reduced plot $b(t)$, where $b = H_c^R(T)/[-(dH_c^R/dT)|_{T_c} \times T_c]$ and t= T/T_c. Here we take $T_c = T_c^s = 1.33$ K. The data compare well with the Werthamer-Helfand-Hohenberg model curve for an orbital-limited weak-coupling spin-singlet superconductor in the clean limit [154].

4.5.2 Superconductivity after polishing the crystal surfaces

The bar-shaped PdTe$_2$ crystal used for the magnetization study was cut from a bigger piece by a scalpel blade. The cuts along the ac-plane were made by spark erosion. In order to exclude that surface superconductivity is due to an impurity face due to the defected spark-cut layer, the crystal's surfaces were carefully

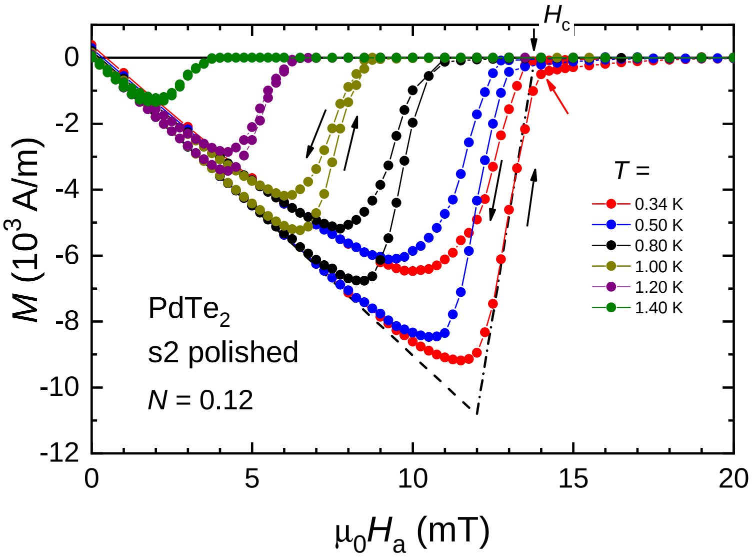

Figure 4.11: ZFC and FC dc-magnetization per unit volume as a function of applied field for PdTe$_2$ (crystal s2) after polishing at temperatures from 0.34 K (right) to 1.4 K (left) as indicated. The initial slope $\chi_m = dM/dH_a$ accounts for a superconducting sample volume of 100 % with $N = 0.12$ (dashed line). The dash-dotted line indicates the idealized $M(H_a)$-curve with slope $1/N$ in the intermediate state at $T = 0.34$ K. The red arrow points to the start of a tail in $M(H_a)$ indicating surface superconductivity

polished by 3 and 1 μm diamond paste till the surfaces appeared brilliant. Next, the dc-magnetization and ac-susceptibility measurements were repeated on the polished crystal. The results basically show that superconductivity of the surface sheath is not removed by polishing. In Fig. 4.11 we show the dc-magnetization. The data are close to identical to the data reported in Fig. 4.2. The tail in $M(H)$ for $H_a > H_c$, which is a signature of surface superconductivity, is reproduced. In Fig. 4.12 we show the dc-susceptibility, or rather M/H_a, as a function of temperature. Again the data are essentially identical to the data reported in Fig. 4.3. Also, the amount of expulsed flux decreases for the lowest dc-fields (0.10 and 0.01 mT). This was attributed to the weak pinning capability of the surface layer. In Figs. 4.13 and 4.14 we report ac-susceptibility measurements as a function of field in driving fields of 0.25 mT and 0.0005 mT, respectively. The latter data-set shows that the screening due to the surface is less effective compared to the data taken before polishing (Fig. 4.4 d). It indicates the polished surface is less effective in pinning the flux. On the other hand surface superconductivity persists to higher fields: 44 mT for the polished sample compared to 33 mT before polishing (at the lowest temperature of 0.31 K).

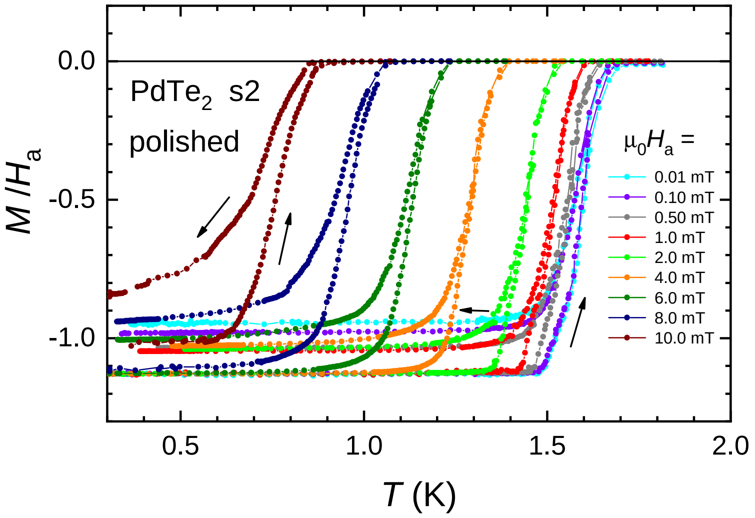

Figure 4.12: ZFC-FC dc-susceptibility, M/H_a, in S.I. units, as a function of temperature in fields $\mu_0 H_a$ from 0.01 mT (right) to 10.0 mT (left) as indicated. The data are taken on PdTe$_2$ (crystal s2) after polishing

In Fig. 4.15 we present the superconducting phase diagram for the polished PdTe$_2$ crystal. The data points are collected from dc-magnetization (Figs. 4.11 and 4.12) and ac-susceptibility (Figs. 4.13 and 4.14). The phase boundary for surface superconductivity, H_c^s(T), is obtained by identifying the field where χ'_{ac} loses its diamagnetic character ($\chi'_{ac} = 0$), see Fig. 4.14. Here we used the χ'_{ac}-data measured with the lowest amplitude of the ac-driving field $\mu_0 H_{ac} = 0.0005$ mT. The H_c^s(T)-curve lies above the curve reported in Fig. 4.7. After polishing $\mu_0 H_c^s(0) = 46.2$ mT, compared to $\mu_0 H_c^s(0) = 34.9$ mT before polishing. The values of T_c^s obtained by extrapolating $H_c^s(T)$ to zero field in the unpolished and polished case are identical within the error bar. We remark that the value of $H_c^s(0)$ depends on the amplitude of the ac-driving field, and that there are subtle effects of polishing on the pinning ability of the surface layer. But overall, the phase diagram before and after polishing is the same. We did not measure the H_c^R phase boundary by resistance on the PdTe$_2$ (crystal s2) after polishing. However, resistance measurements on two other crystals with freshly cleaved surfaces confirmed enhanced values $H_c^R \gg H_c$.

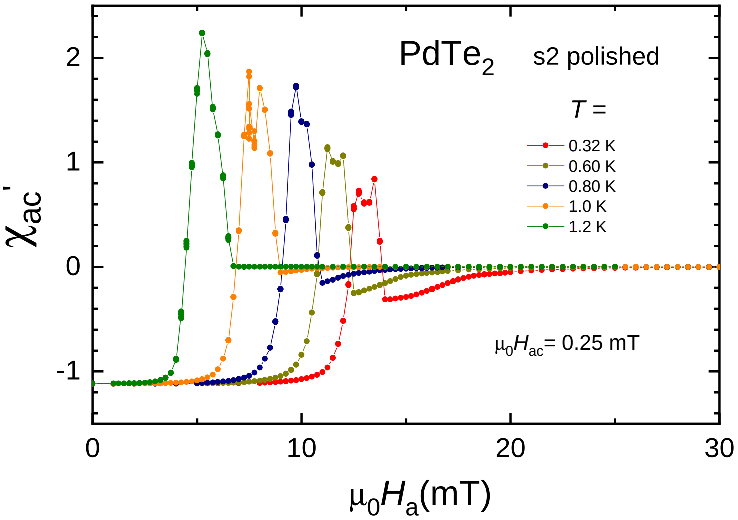

Figure 4.13: Ac-susceptibility as a function of applied field of PdTe$_2$ (crystal s2) after polishing. The driving field $\mu_0 H_{ac} = 0.25$ mT. Data are taken at temperatures from 0.32 K to 1.2 K as indicated. The diamagnetic contribution above the DPE peak, *i.e.* for fields $H_a > H_c$, signals surface superconductivity.

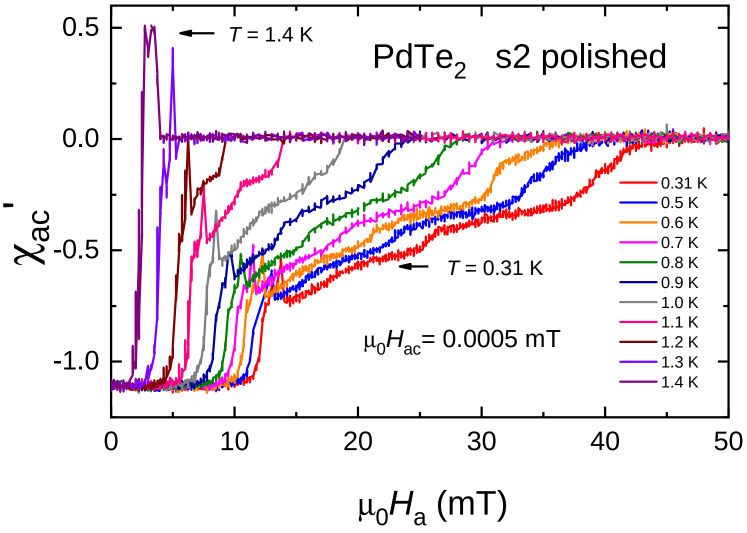

Figure 4.14: Ac-susceptibility of PdTe$_2$ (crystal s2) after polishing as a function of the applied field. Data were taken in a driving field $\mu_0 H_a = 0.0005$ mT at temperatures in the range $T = 0.31 - 1.4$ K as indicated.

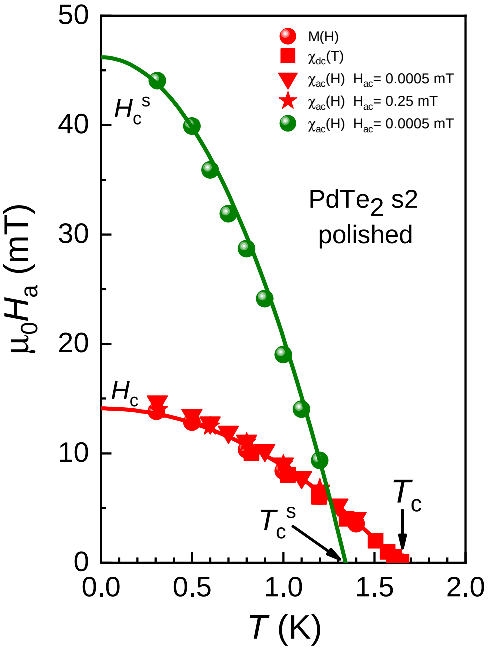

Figure 4.15: Superconducting phase diagram of PdTe$_2$ (crystal s2) after polishing. Data points are taken from dc-magnetization and ac-susceptibility as indicated. The solid red and green lines represent fits to the critical fields H_c for bulk superconductivity and H_c^s for surface superconductivity with a quadratic temperature function.

Chapter 5

Superconductivity under pressure in the Dirac semimetal $PdTe_2$

The Dirac semimetal $PdTe_2$ *was recently reported to be a type-I superconductor (*T_c *=1.64 K,* $\mu_0 H_c(0) = 13.6$ *mT) with unusual superconductivity of the surface sheath. We here report a high-pressure study,* $p \leq 2.5$ *GPa, of the superconducting phase diagram extracted from ac-susceptibility and transport measurements on single crystalline samples.* $T_c(p)$ *shows a pronounced non-monotonous variation with a maximum* T_c *=1.91 K around 0.91 GPa, followed by a gradual decrease to 1.27 K at 2.5 GPa. Surface superconductivity persists under pressure as demonstrated by the large superconducting screening signal for applied dc-fields* $H_a > H_c$*. Surprisingly, for* $p \geq 1.41$ *GPa the superconducting transition temperature at the surface* T_c^S *is larger than* T_c *of the bulk. Therefore surface superconductivity may possibly have a non-trivial topological nature. We compare the measured pressure variation of* T_c *with recent results from band structure calculations and discuss the importance of a Van Hove singularity.*

This chapter has been published as J. Phys.: Condens. Matter 32 025603 (2020).

5.1 Introduction

The family of layered transition metal dichalcogenides attracts much attention, because of the wide diversity of fascinating electronic properties. One of the present-day research interests is the possibility to realize novel quantum states as a result of the topological non-trivial nature of the electronic band structure [128, 129, 130, 161]. Especially, it has been proposed that these materials host a generic coexistence of type-I and type-II three dimensional Dirac fermion states [161]. An interesting example in this respect is PdTe$_2$ that has been classified as a type-II Dirac semimetal following a concerted examination of *ab-initio* electronic structure calculations and angle-resolved photoemission spectroscopy (ARPES) experiments [132, 120, 121, 161, 162]. In a type-II Dirac semimetal the Hamiltonian breaks Lorentz invariance because the energy dispersion relations, *i.e.* the Dirac cone, are tilted [128]. The Dirac point is then the touching point between the electron and hole pockets and a nearly flat band may form near the Fermi level. Moreover, PdTe$_2$ is a superconductor below 1.6 K [131, 163], which solicits the intriguing question whether superconductivity is promoted by the nearly flat band and consequently has a topological nature [121]. Topological non-trivial superconductors attract much interest since it is predicted these may host protected Majorana zero modes at the surface (for recent reviews see Refs. [133, 134]). This in turn offers a unique design route to make devices for topological quantum computation.

Superconductivity in PdTe$_2$ was discovered in 1961 (Ref. [131]), but was not investigated in detail until 2017, when Leng *et al.* [163] carried out comprehensive magnetic and transport experiments on single-crystals. Unexpectedly, dc-magnetization measurements, $M(H)$, revealed that PdTe$_2$ is a bulk type-I superconductor, which was further embodied by the observation of the differential paramagnetic effect in the ac-susceptibility measured in applied magnetic dc-fields. The critical field $H_c(T)$ follows the standard quadratic temperature variation with $\mu_0 H_c(0) = 13.6$ mT. The possibility of type-I superconductivity in Dirac materials was recently investigated by Shapiro *et al.* [164] employing a microscopic pairing theory for an arbitrary tilt parameter of the Dirac cone. For PdTe$_2$ these authors concluded type-I superconductivity is feasible for a tilt parameter $k = 2$. Another interesting aspect of PdTe$_2$ is the observation of surface superconductivity, as evidenced by large screening currents in the ac-susceptibility for applied dc-fields $H_a > H_c$ [163]. The critical field for surface superconductivity H_c^S does not follow the standard Saint-James - de Gennes expression $H_{c3} = 2.39 \times \kappa H_c$ [141], where κ is the Ginzburg-Landau parameter. This led to the proposal [163] that superconductivity of the surface sheath might have a topological nature and originates from topological surface states detected by ARPES [120, 132]. More recently, specific heat [165] and magnetic penetration depth [166, 167], measurements have been conducted. These confirm conventional weak-coupling Bardeen-Cooper-Schrieffer (BCS) superconductivity, with a full gap in the bulk. At the same time zero-field scanning tunneling microscopy (STM) and spectroscopy (STS) experiments [162, 168] lend further support for the absence of in-gap states, which seems to rule out topological superconductivity at the surface. Dominant s-wave superconductivity was also concluded from tunneling spectroscopy experiments on side junctions [169]. Nonetheless, the uncommon type-I behavior for a binary compound, and the unexplained superconductivity of the surface sheath, justify a further in-depth examination of the superconducting properties of $\mathrm{PdTe_2}$.

We here report the results of a high-pressure investigation of the superconducting phase diagram of $\mathrm{PdTe_2}$ single crystals ($p \leq 2.5$ GPa). Combined resistivity and ac-susceptibility measurements show T_c increases at low pressures, then passes through a maximum of 1.91 K around 0.91 GPa, and subsequently decreases at higher pressure. Under pressure superconductivity maintains its type-I character. Surface superconductivity persists under pressure as demonstrated by the large superconducting screening signal for applied dc-fields $H_a > H_c$. Interestingly, for $p \geq 1.41$ GPa the superconducting transition temperature of the surface, T_c^S, is larger than T_c of the bulk. Therefore surface superconductivity may possibly have a non-trivial topological nature. The initial increase of T_c with pressure is at variance with the smooth depression predicted by recent electronic structure calculations [170].

5.2 Experimental

The crystals used for our high pressure study were taken from the single-crystalline boule prepared by the modified Bridgman technique [59] and characterized in Ref. [163]. Powder X-ray diffraction confirmed the trigonal $\mathrm{CdI_2}$ structure (spacegroup $P\bar{3}m1$ [142]. Scanning electron microscopy (SEM) with energy dispersive x-ray (EDX) spectroscopy showed the proper 1:2 stoichiometry within the experimental resolution of 0.5%. Laue backscattering was used to orient the crystals. Standard four-point resistance measurements were performed in a Physical Property Measurement System (PPMS, Quantum Design) at temperatures down to 2 K. The resistivity, $\rho(T)$, of our crystals shows metallic behavior. A typical trace in the temperature range 2-300 K is shown in Fig. 5.1. The residual resistance ratio $R(300\mathrm{K})/R(2\mathrm{K}) = 30$.

Electrical resistance, $R(T,H)$, and ac-susceptibility, $\chi_{ac}(T,H)$, measurements under high-pressure were performed utilizing a clamp-type piston-cylinder cell, which has a double-layer made of Cu-Be and NiCrAl alloys. The single crystal sizes for $R(T,H)$ and $\chi_{ac}(T,H)$ were $\sim 2.3 \times 1.0 \times 0.18$ mm^3 and $\sim 2.9 \times 1.0 \times 0.67$ mm^3, respectively. Both samples were mounted on a plug and loaded into a Teflon

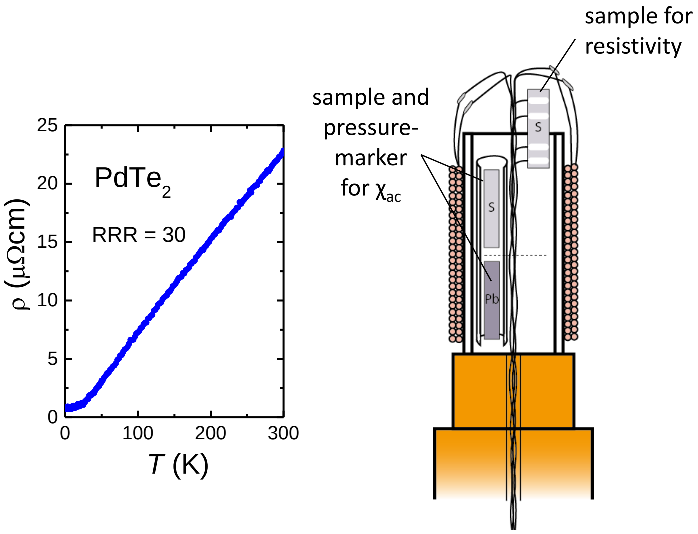

Figure 5.1: Left: Resistivity of PdTe$_2$ measured with the current in the basal plane. Right: Pressure plug with samples and χ_{ac} coils mounted (schematic).

capsule together with coils and a pressure-transmitting medium, Daphne oil 7373, for hydrostatic compression [62]. A schematic drawing of the plug with samples and coil is shown in Fig. 5.1. The generated pressure in the capsule relating to each load was estimated from the calibration data for this cell, which was obtained from the pressure variations of superconducting transition temperatures of lead and tin in previous experiments [63, 171]. We carried out the compression experiments on the crystals twice, first up to a pressure of 1.24 GPa and in a second run up to 2.49 GPa. Typical experimental conditions are as follows. The high-pressure cell was compressed at room temperature and then cooled down to about 0.3 K using a ^{3}He refrigerator (Oxford Instruments Heliox VL). Electrical resistivity was measured by a resistance bridge (Linear Research LR-700) using a low-frequency ac method with an excitation current $I = 300\mu$A. In order to investigate the field-suppression of T_c, a magnetic field was applied along the current, parallel to the a-axis. For ac-susceptibility measurements, a small cylinder, composed of an excitation coil and a pick-up coil in which the sample is situated, was prepared. The in-phase and out-of-phase signals were detected in the driving field $\mu_0 H_{ac} = 0.0047$ mT with a frequency of $f_{ac} = 313$ Hz using a lock-in amplifier (EG&G Instruments Model 7260). Measurements were made in zero field and in applied dc-fields using a superconducting magnet. Special care was taken to reduce the remnant field of the superconducting magnet to close to zero, since our PdTe$_2$ crystals show type-I superconductivity.

The Hall effect was measured on two $PdTe_2$ crystals in a piston-cylinder clamp cell developed for the Physical Property Measurement System (PPMS, Quantum Design) at nine different pressures up to 2.07 GPa. The sample space is 4.4 mm in diameter and ∼15 mm in height. Two crystals were placed in two stages along a compression axis perpendicular to the sample plane. The sample size (length × width × thickness) amounts to $2.8 \times 1.4 \times 0.08$ mm^3 and $2.9 \times 1.0 \times 0.19$ mm^3 for crystal 1 and 2, respectively. The current was applied in the basal-plane of the crystals, whereas the magnetic field was applied along the trigonal axis, perpendicular to the sample plane. Measurements were carried out for two field polarities, B^+ and B^-, and the Hall resistance, R_H, was obtained by symmetrizing: $R_H = (R_{B^+} - R_{B^-})/2$.

Overall the resistivity, $\rho(T)$, measured in the temperature range 2-300 K showed little variation with pressure and remained metallic. However, the absolute ρ-value at 300 K decreases smoothly with respect to pressure to about 80% of the ambient pressure value at the highest pressure 2.49 GPa.

5.3 Results

The overall results of the two pressure runs are reported in Fig. 5.2. In the first run data were taken at pressures of 0.25, 0.58, 0.91 and 1.24 GPa. Here the normal state resistance $R_N \simeq 70\ \mu\Omega$. For the second run new voltage contacts were made on the crystal resulting in $R_N \simeq 60\ \mu\Omega$. The applied pressures are 0.75, 1.08, 1.41, 1.74, 2.07 and 2.49 GPa. We remark the zero-pressure data were measured after releasing the pressure. Also, the value of the ac-susceptibility differed somewhat between different cool downs and between the two pressure runs. For clarity all the χ_{ac} data in the lower panel of Fig. 5.2 are normalized to -1 in the superconducting state.

At ambient pressure superconductivity is found with onset temperatures of 1.63 K and 1.59 K in $R(T)$ and $\chi_{ac}(T)$, respectively. The resistance curve shows a double structure at low pressures. We attribute this double structure in $R(T)$ to parts of the crystal responding somewhat differently to pressure. However, for $p \geq 1.08$ GPa the resistance curves show a single sharp superconducting transition. A similar behavior is observed in $\chi_{ac}(T)$ with relatively sharp, single transitions at pressures of 1.08 and 1.24 GPa. However, for $p \geq 1.41$ GPa the transition in $\chi_{ac}(T)$ becomes structured again. As we will demonstrate in the next section, at these pressures the initial screening step is attributed to surface superconductivity [163], while the ensuing second step with a full diamagnetic screening is attributed to bulk superconductivity.

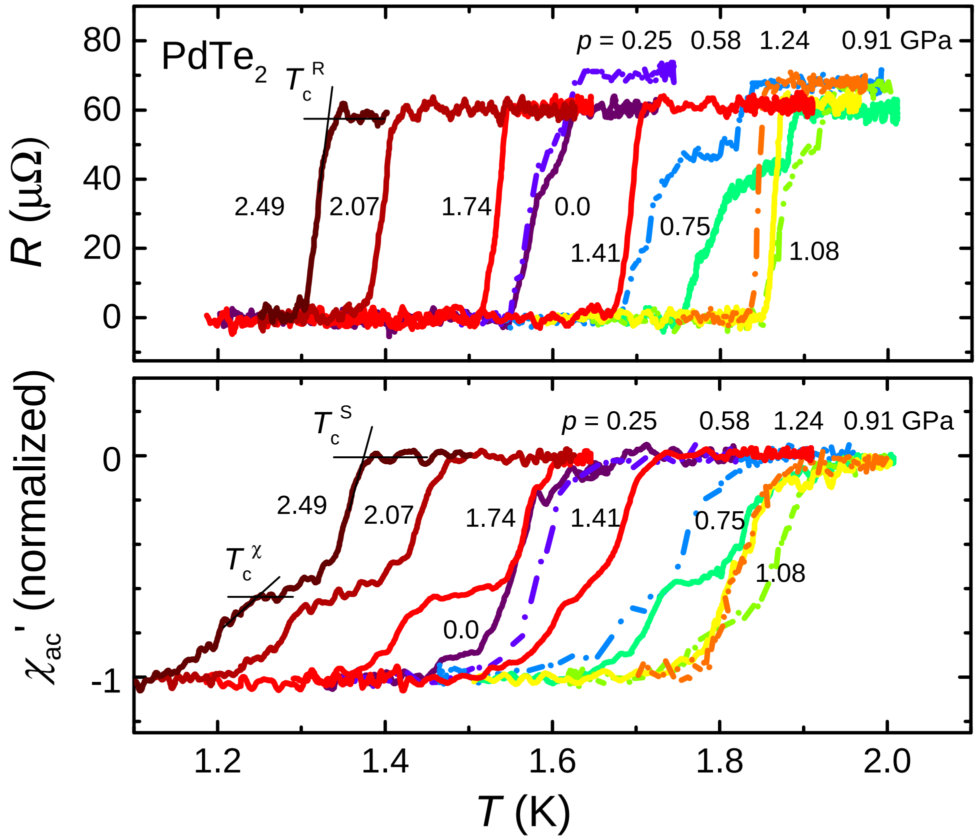

Figure 5.2: Resistance and ac-susceptibility (normalized to -1 in the superconducting state) of single-crystalline PdTe$_2$ as a function of temperature around T_c at pressures up to 2.49 GPa as indicated. The data were taken in two pressure runs (see text): dashed-dotted lines for the first run (p-values listed above the curves) and solid lines for the second run (red p-values listed adjacent to the curves). The curves at 0 GPa were measured after releasing the pressure in the second run. T_c^R is determined from the onset of superconductivity in $R(T)$ as indicated for $p = 2.49$ GPa by the thin solid lines. For $p \geq 1.41$ GPa the onset of diamagnetic screening in $\chi_{ac}(T)$ is attributed to surface superconductivity at T_c^S, and the further drop signals bulk superconductivity at T_c^χ, as indicated for $p = 2.49$ GPa. See text.

A first important conclusion from the data in Fig. 5.2 is that superconductivity is enhanced under pressure with a maximum $T_c = 1.9$ K at around 0.9 GPa. At higher pressures T_c is gradually depressed down to 1.3 K at 2.5 GPa. Before presenting the pressure-temperature ($p - T_c$) phase diagram we discuss the magnetic field variation of T_c at different pressures.

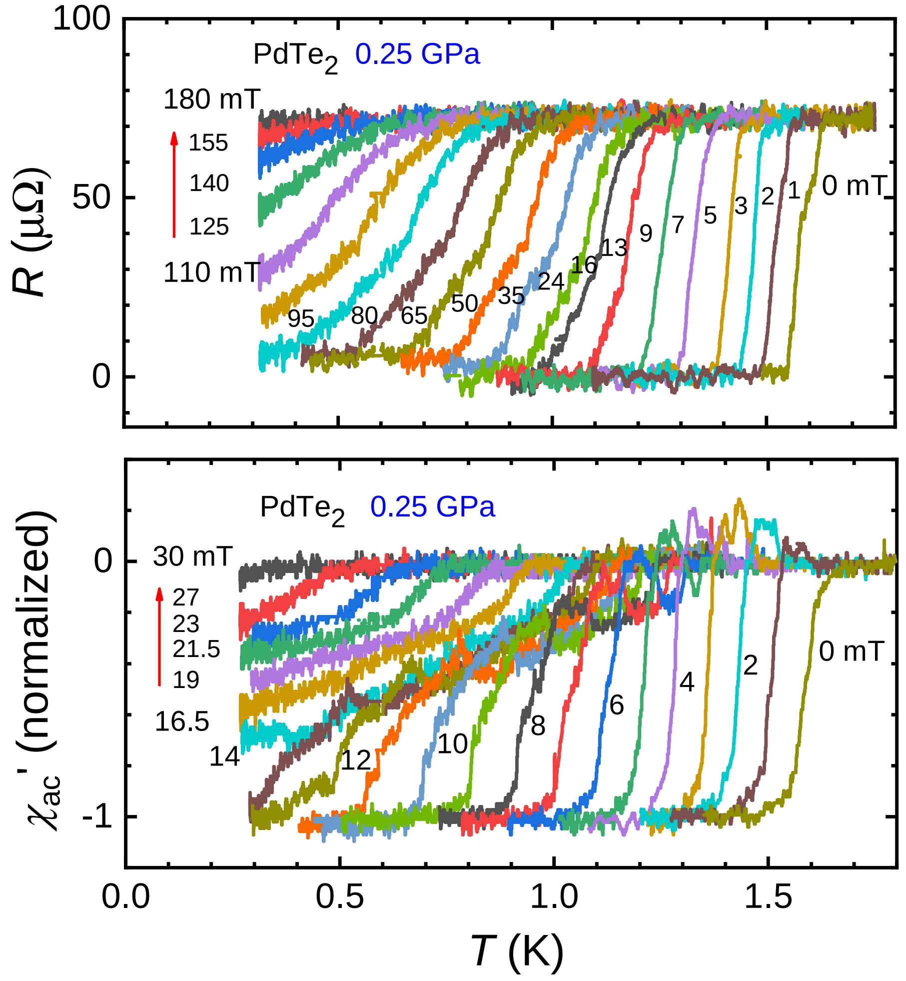

Figure 5.3: Upper panel: Resistance of PdTe$_2$ as a function of temperature at a pressure $p = 0.25$ GPa measured in applied magnetic fields $\mu_0 H_a \parallel I \parallel a$. Curves from right to left are taken in fields of 0, 1, 2, 3, 5, 7, 9, 13, 16, 24, 35, 50, 65, 80, 95, 110, 125, 140, 155 and 180 mT. Lower panel: Ac-susceptibility at $p = 0.25$ GPa measured in applied magnetic fields. Curves from right to left in 0 mT to 14 mT with 1 mT steps and in 16.5, 19, 21.5, 23, 27 and 30 mT.

5.3.1 T_c^χ and T_c^S: Field-temperature phase diagram from χ_{ac}

In order to investigate the pressure dependence of the superconducting phase diagram in the H-T plane we have measured at each pressure the resistance and ac-susceptibility in applied dc-fields, H_a. A typical data set taken at $p = 0.25$ GPa is shown in Fig. 5.3. In the lower panel, with χ_{ac}-data, the zero-field curve shows

$T_c^\chi = 1.63$ K. In small applied fields a peak appears just below T_c due to the differential paramagnetic effect (DPE). This peak signals the field induced intermediate state as discussed in Ref. [163]. It shifts to lower temperatures with increasing field and for higher fields is progressively depressed because of an additional screening signal that precedes the DPE peak. The additional screening is attributed to superconductivity of the surface sheath [163]. Partial screening is still visible at 27 mT, but has nearly vanished at $\mu_0 H_a = 30$ mT and 0.3 K. Consequently, in the limit $T \to 0$ $H_c^S(0) > H_c(0)$ ($= 14.7$ mT at 0.25 GPa).

Critical field of bulk superconductivity

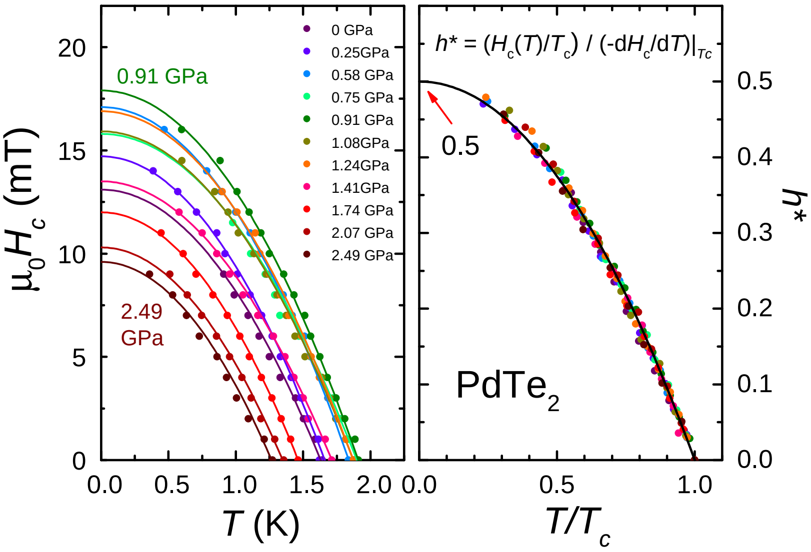

Figure 5.4: Left panel: Critical field $H_c(T)$ for type-I superconductivity in PdTe$_2$ at pressures between 0 and 2.49 GPa as indicated. The solid lines represent $H_c(T) = H_c(0)[1 - (T/T_c)^2]$ at different pressure, where $T_c = T_c^\chi$ is the bulk superconducting transition temperature extracted from the χ_{ac}-data in applied fields. Right panel: Reduced plot $h^* = (H_c(T)/T_c)/(-dH_c/dT)|_{T_c}$ *versus* T/T_c. The solid line represents $h^* = 0.5 \times [1 - t^2]$. See text.

In Fig. 5.4 we present the critical field for bulk superconductivity $H_c(T)$. Bulk superconductivity is identified by the onset of the DPE peak. We label this temperature by T_c^χ. The data are obtained by tracing the T_c^χ-values as a function of the applied field. The solid lines in Fig. 5.4 represent $H_c(T) = H_c(0)[1 - (T/T_c)^2]$ at different pressures, where $T_c = T_c^\chi$. The quadratic temperature variation is consistent with type-I superconductivity. In fact all the data under pressure collapse on one single curve, $h^*(t)$, as shown in the right panel of Fig. 5.4. Here the standard expression for plotting $H_c(T)$ in a reduced form is applied, with $h^* = (H_c(T)/T_c)/(-dH_c/dT)|_{T_c}$ where $t = T/T_c$ (Ref. [172]). For a type-I superconductor $h^*(0) = 0.5$. The collapsed curve $h^*(t)$ shows type-I superconductivity persists over the whole pressure range.

Critical field of surface superconductivity

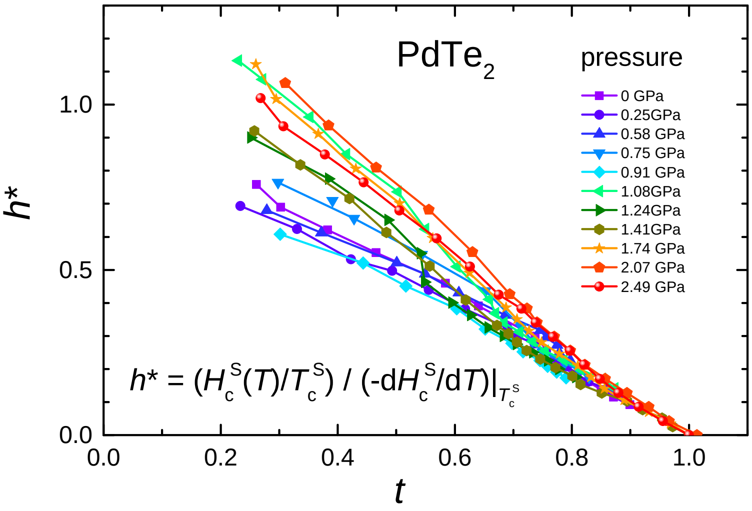

Figure 5.5: Critical field $H_c^S(T)$ for superconductivity of the surface sheath in PdTe$_2$ at pressures between 0 and 2.49 GPa as indicated. The data are plotted in the reduced form $h^* = (H_c^S(T)/T_c^S)/(-dH_c^S/dT)|_{T_c^S}$ *versus* $t = T/T_c^S$.

At each pressure we have constructed the $H_c^S(T)$ phase boundary. Here surface superconductivity is identified by the additional (partial) diamagnetic screening which persists at $H_a > H_c$. In an attempt to collapse all the $H_c^S(T,p)$-data on a single curve, a plot of $h^*(t)$ is presented in Fig. 5.5, where $h^* = (H_c^S(T)/T_c^S)/(-dH_c^S/dT)|_{T_c^S}$ and $t = T/T_c^S$. Note that for pressures up to 1.24 GPa T_c^S and the initial slope $-dH_c^S/dT|_{T_c^S}$ are determined by extrapolation, as shown in Fig.5.6 for 0.25 and 1.08 GPa. This introduces some uncertainty in the data, but the overall trend is that $h^*(0)$ increases as a function of pressure. This indicates the superconducting pairing interaction changes in a non-trivial way. Leng *et al.* [163] reported that the $H_c^S(T)$-curve for a different crystal at ambient pressure followed a quadratic temperature variation. This is not observed for the present crystal. Instead $H_c^S(T)$ rather shows a downward or upward curvature near $t = 0.7 - 0.8$.

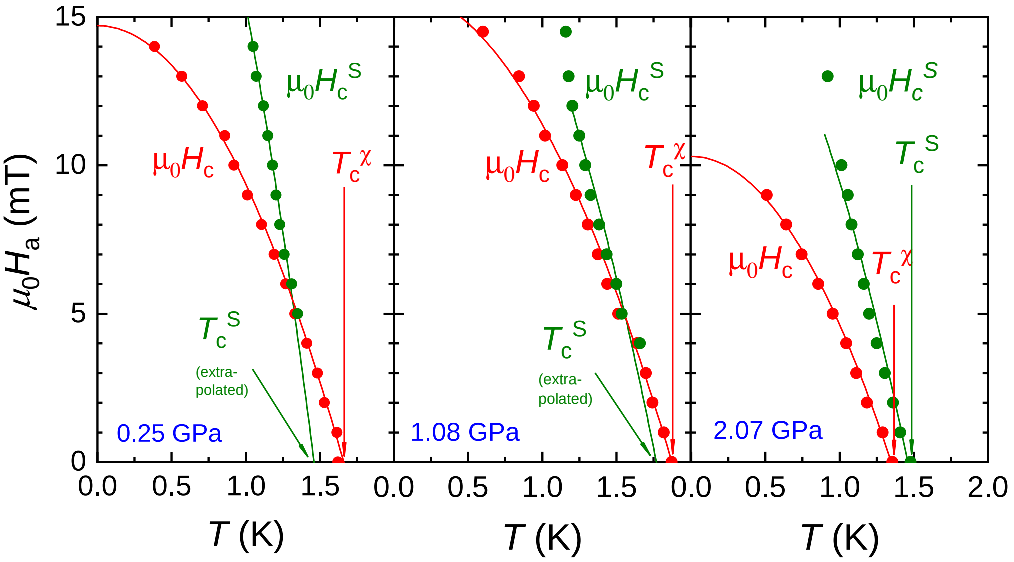

Figure 5.6: Superconducting phase diagram of PdTe$_2$ deduced from ac-susceptibility at a pressure of 0.25 GPa (left), 1.08 GPa (middle) and 2.07 GPa (right), for H_a directed in the basal plane. Bulk type-I superconductivity is found below the critical field $H_c(T)$. The data points (red solid symbols) follow the standard quadratic temperature variation $H_c(T) = H_c(0)[1 - (T/T_c^\chi)^2]$ (red lines). Surface superconductivity is found below $H_c^S(T)$ (green solid symbols). The transition temperature, $T_c^S(0)$, is determined by extrapolating $H_c^S(T)$ to $H_a = 0$ (green lines). The values of the bulk T_c^χ and surface T_c^S are indicated by arrows. Note that at 2.07 GPa $T_c^S > T_c^\chi$.

Phase diagram comparison between bulk and surface superconductivity

In Fig. 5.6 (left panel) we present the phase diagram for bulk and surface superconductivity at 0.25 GPa extracted from the ac-susceptibility data in Fig. 5.3. Bulk superconductivity is identified by the onset of the DPE peak. We label this temperature by T_c^χ. Its field variation is presented by the red symbols in the left panel of Fig. 5.6. $T_c^\chi(H)$ follows the standard quadratic temperature variation $H_c(T) = H_c(0)[1 - (T/T_c^\chi)^2]$ with $H_c(0) = 14.7$ mT. Surface superconductivity is identified by the additional (partial) diamagnetic screening which becomes visible at $H_a \approx 5$ mT in Fig. 5.3 (lower panel). We label this temperature by T_c^S. Its field variation $T_c^S(H)$ is traced by the green symbols in the phase diagram. By extrapolating $T_c^S(H)$ to zero field we obtain $T_c^S(0)$. We find $T_c^S(0) < T_c^\chi(0)$, just like reported previously at ambient pressure [163].

In the Appendix Fig. 5.12, we show the ac-susceptibility in applied dc-fields at 1.08 and 2.07 GPa. The superconducting phase diagrams extracted from these figures are shown in the middle and right panel of Fig. 5.6. Upon increasing the pressure, the phase lines $H_c(T)$ and $H_c^S(T)$ move apart and do no longer intersect at $p = 2.07$ GPa, in which case $T_c^S(0) > T_c^\chi(0)$. Now the DPE peak that signals bulk superconductivity shows up in the χ_{ac}-data, measured in applied dc-fields, at a temperature below the initial diamagnetic step due to surface superconductivity (see the Appendix Fig. 5.13).

5.3.2 T_c^R: Field-temperature phase diagram from transport

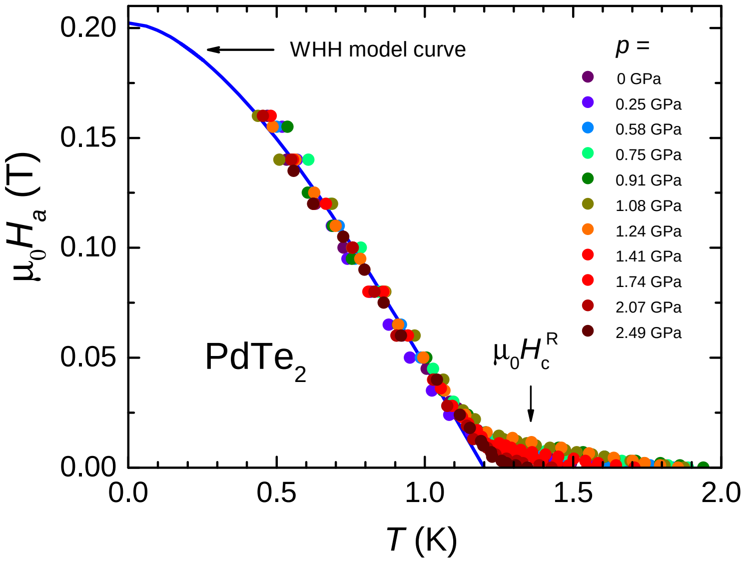

Figure 5.7: Superconducting phase diagram of PdTe$_2$ constructed from resistance measurements in the H-T plane at different pressures, as indicated. For 1.3-1.9 K the data points $H_c^R(T)$ denote bulk superconductivity. Below 1.3 K (partial) superconductivity persists resulting in a critical field $H_c^R(0)$ of ~ 0.2 T. The blue solid line compares the data to the Werthamer-Helfand-Hohenberg model (see text).

At each pressure we investigated the depression of superconductivity by measuring $R(T)$ in fixed applied fields. The $R(T)$-data for 0.25 GPa are shown in the upper panel in Fig. 5.3. Additional data sets at 1.08 and 2.07 GPa are reported in the Appendix. In all cases superconductivity is first depressed rapidly in small fields, and $H_c^R(T)$ tracks $H_c(T)$ for bulk superconductivity as deduced from χ_{ac} (see Fig.5.4). In Fig. 5.7 we show the H-T phase diagram determined from the transport data at pressures up to 2.49 GPa. The type-I quadratic temperature variation is restricted to the temperature range 1.3-1.9 K. Below 1.3 K the transition in $R(T)$ broadens and traces of superconductivity are visible up to ~ 0.2 T. The onset temperatures for superconductivity from $R(T)$ in fixed magnetic fields below 1.3 K are also plotted in Fig. 5.7. A steady increase of $H_c^R(T)$ is observed. A comparison with the Werthamer-Helfand-Hohenberg (WHH) model [154] indicates the data extrapolate to $H_c^R(0) \simeq 0.2$ T for $T \to 0$. We remark that for the crystal studied in Ref. [163] this value is somewhat larger (~ 0.3 T).

5.3.3 Pressure-temperature phase diagram

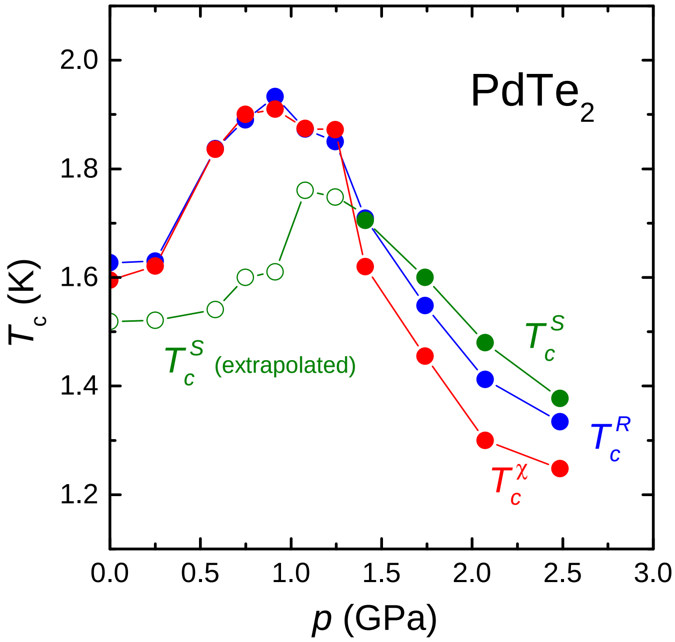

Figure 5.8: Pressure variation of the superconducting transition temperature, T_c^χ, as determined from χ_{ac} (red symbols). T_c^S denotes surface superconductivity (green symbols). The open symbols are obtained after extrapolation of $T_c^S(H)$ to zero field (see text). Note that for $p \geq 1.41$ GPa $T_c^S > T_c^\chi$. T_c^R (blue symbols) is determined by the onset temperature in $R(T)$.

The transition temperatures for bulk and surface superconductivity, T_c^χ and T_c^S, respectively, determined from the χ_{ac} measurements at eleven different pressures are reported in Fig. 5.8. For $p \leq 1.24$ GPa T_c^S is determined by extrapolation, as shown in Fig. 5.6 (left and middle frame), and is smaller than T_c^χ of the bulk, however, for $p \geq 1.41$ GPa $T_c^S > T_c^\chi$. We also plot in Fig. 5.8 the onset transition temperatures, $T_c^R(p)$, determined by extrapolation of the $R(T)$-curves just below

T_c to the normal state plateau values (see the 2.49 GPa curve in Fig. 5.2). At low pressures $T_c^R(p)$ agrees with T_c^X, while at higher pressure it is close to T_c^S.

5.4 Analysis and Discussion

The mechanical and electronic properties of $PdTe_2$ under pressure have been investigated theoretically by several groups [170, 173, 174]. The only experimental high-pressure study carried out so far is by Soulard *et al.* [173] who conducted high-pressure X-ray diffraction experiments at room temperature and 300 °C to investigate the possibility of a structural phase transition. They found that an abrupt change in the interatomic distances occurs above $p = 15.7$ GPa at room temperature, but the volume *versus* pressure curve exhibits no discontinuity. Under pressure the unit cell volume decreases by 17.6% at the maximum applied pressure of 27 GPa, and the c/a ratio decreases from 1.27 to 1.24 at 27 GPa. A bulk modulus, B_0, of 102 GPa was derived from the experimental data. This value is to be compared with 71.2 GPa (74.2 GPa) derived from first principle calculations by Lei *et al.* [174] at 300 K (0 K). Xiao *et al.* [170] computed the optimized lattice parameters as a function of pressure, which are slightly overestimated compared to the experimental data [173]. Overall, these studies indicate there is no structural transition in the modest pressure range up to 2.5 GPa in our experiments. For a layered material the change in the c/a-ratio is normally an important control parameter for the electronic properties. However, for $PdTe_2$ this change is very tiny and 0.2% at most up to 2.5 GPa [173]. In the following we focus on the superconducting properties.

5.4.1 Bulk superconductivity

A major result is the non-monotonous variation of T_c with pressure reported in Fig. 5.8. T_c first increases to 1.91 K at 0.91 GPa and then is gradually depressed. We first compare the experimental results with theoretical calculations. The evolution of superconductivity with pressure was investigated theoretically by Xiao *et al.* [170]. The authors used the Allen-Dynes-modified McMillan equation to calculate T_c, with the characteristic phonon frequency ω_{log}, the electron-phonon coupling constant λ and the Coulomb pseudopotential $\mu^* \simeq 0.1$ as input parameters. Combined electronic structure and phonon-density of states calculations show a gradual decrease of λ and an increase of ω_{log} (blue shift), but overall the calculated T_c decreases from 2.0 K at ambient pressure to 0.6 K at 10 GPa. Note the calculated T_c at $p = 0$ is larger than our experimental value of 1.6 K. While a decrease to 0.6 K at 10 GPa is within bounds of the extrapolation of $T_c(p)$ in Fig. 5.8, the calculations by Xiao *et al.* [170] clearly do not capture the initial in-

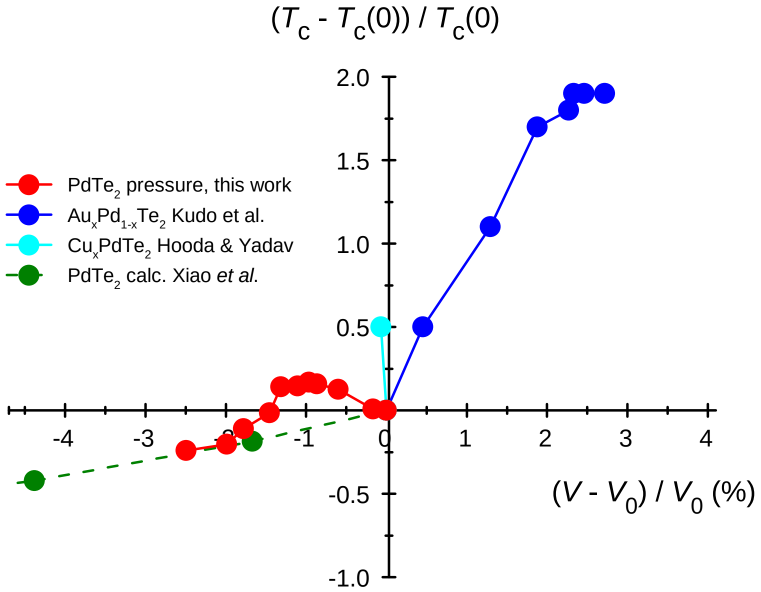

Figure 5.9: Relative change of the superconducting transition temperature, $(T_c - T_c(0))/T_c(0))$, as a function of the relative volume change $(V - V_0)/V_0$. Red symbols: $PdTe_2$ under pressure, this work; blue symbols: $Au_xPd_{1-x}Te_2$, Ref. [152]; magenta symbol: Cu_xPdTe_2, Ref. [147]; green symbols: calculated, Ref. [170].

crease of T_c and its maximum value at 0.91 GPa. The superconducting properties of $PdTe_2$ were also investigated by Kim *et al.* [175] employing the same McMillan formalism. Their phonon band structure calculations show the electron-phonon interaction is dominated by the optical $O_{1,2}$ and O_3 phonon modes. Furthermore, they emphasize the importance of a saddle-point van Hove singularity (vHs) close to the Fermi energy. The computed T_c is 1.79 K at ambient pressure. The importance of a vHs is further illustrated by the case of $PtTe_2$, which is isoelectronic with $PdTe_2$ but does not show superconductivity. Here the vHs-band has a broad dispersion along k_z leading to a lower density of states at the Fermi level and absence of superconductivity [175]. Calculations for $PdTe_2$ with a 15% volume contraction, which corresponds to a pressure of ~20 GPa, indicate the vHs band moves close to the Fermi level [175], which would produce a higher T_c. However, this is at variance with the experimental data presented in Fig. 5.8.

Another way to tune T_c besides pressure is via doping or substitution. Recently, it was demonstrated that Cu intercalation enhances T_c to a maximum value of 2.6 K in Cu_xPdTe_2 [132, 176, 147] for $x = 0.06$. Upon intercalation the volume contracts, but changes are minute: $\Delta V/V = -0.07\%$ for $x = 0.04$ [147], which corresponds to an applied pressure of 0.07 GPa. This shows Cu intercalation cannot be equated to chemical pressure in tuning superconductivity. The same holds for the substitution series $(\mathrm{Au}_x\mathrm{Pd}_{1-x})\mathrm{Te}_2$ [152]. Upon alloying with Au, T_c increases up to 4.65 K for $x = 0.40$. Simultaneously, the volume *increases* by 2.5%, which corresponds to a *negative* pressure of $\sim$2.5 GPa. The experimental and calculated variation of T_c with pressure and doping are summarized in Fig. 5.9. Here we trace the relative change of T_c as a function of the relative volume change, $(V - V_0)/V_0$, where a bulk modulus of 102 GPa is used [173]. Although T_c generally decreases with a smaller volume, the experimentally observed positive dT_c/dp for PdTe_2 up to 0.91 GPa is at odds with this trend.

In an attempt to shed further light on the pressure variation of T_c, we have conducted Hall effect measurements on two PdTe_2 crystals under pressure up to 2.07 GPa (see the Appendix). The Hall resistance, $R_H(B)$, is a non-linear function indicating the presence of several charge carrier bands. At the lowest pressure of 0.25 GPa the low-field dominant carrier concentration, n, amounts to 1.5-1.7×10^{22} cm^{-3} at 2 K. It varies quasi-linearly with pressure resulting in an increase of $\sim$20% at 2.07 GPa. Overall the $R_H(B)$-curves show a modest, smooth pressure variation, which tells us the nonmonotonous variation $T_c(p)$ is not accompanied by a related change in the carrier concentration.

The non-monotonous variation of T_c indicates the density of states and the electron phonon-coupling constant are affected in an intricate manner by doping and/or pressure. Possibly this is a result from band structure subtleties that have not been probed in the coarse-grained calculations carried out so far [170, 173, 174]. In order to access the electronic band structure under pressure, a quantum oscillations study is highly desirable. The feasibility to observe the Shubnikov - de Haas effect and the de Haas - van Alphen effect at ambient pressure has been demonstrated in Refs. [145, 121, 177]. In the same context, small structural modifications that might influence T_c, such as changes in the z-coordinate of Te atoms in the unit cell that would affect the $O_{1,2}$ and O_3 phonon modes, cannot be excluded based on the X-ray diffraction experiment with a first pressure point at 2.2 GPa [173]. This calls for high-precision low-pressure ($p \leq 2.5$ GPa) single-crystal X-ray diffraction measurements. Finally, we mention that a maximum in T_c is also predicted to occur at the topological phase transition from a Type-I to Type-II Dirac semimetal, *i.e.* when the Dirac cone tilt parameter k passes 1 [164, 178]. Indeed such a topological phase transition is predicted in the pressure range 4.7-6.1 GPa [170], but this is a factor $\sim$ 5 higher than the pressure (0.9 GPa) of the maximum T_c value.

5.4.2 Surface superconductivity

The distinct pressure variation of the superconducting transition temperature of the surface sheath, T_c^S, and of the bulk, T_c^χ, reported in Fig. 5.6 and Fig. 5.8, is an extraordinary result. We recall this feature is derived from the ac-susceptibility curves measured in fixed magnetic fields at eleven different pressures. The data show how type-I superconductivity in the bulk, probed by the DPE-peaks in small applied dc-fields, is progressively depressed with field, while surface superconductivity is observed for $H_a > H_c$ (see also Ref. [163]). Upon increasing the pressure, the DPE peak is more rapidly depressed compared to surface screening. At 2.07 GPa the DPE effect is - already in the lowest applied fields - almost completely screened by the surface. Hence for $p \geq 1.41$ GPa $T_c^S > T_c^\chi$. This is further underpinned by the observation that $H_c(T)$, defined by $T_c^\chi(H)$, follows the quadratic temperature variation at all pressures, characteristic for bulk type-I superconductivity (Fig. 5.4). Note that T_c^S is defined as the onset temperature for the diamagnetic signal due to surface superconductivity, while the transition itself may become very broad. $H_c^S(p)$ has a maximum near 0.9 GPa, similar to $H_c(p)$ (Fig. 5.14). When the $H_c^S(T, p)$ data are traced in a reduced form $h^*(t)$ the data do not collapse on a single curve, see Fig. 5.5. Instead the trend is that the values $h^*(t)$ increase with respect to pressure, which indicates the superconducting pairing interaction changes in a non-trivial way. The distinct $H_c(T)$- and H_c^S-curves and their dissimilar pressure dependence strongly suggest surface and bulk superconductivity are independent phenomena and not tightly connected, in contrast to the familiar Saint James - de Gennes surface superconductivity [141]. This complies with the estimated value of the Ginzburg-Landau parameter $\kappa = 0.08 - 0.28 < 0.42$ [163, 166]. It remains tempting to relate surface superconductivity in PdTe$_2$ to topological surface states detected by ARPES [120, 132, 162]. These surface states could possibly be investigated by STM experiments in small applied fields ($H_a > H_c$). The STM experiments performed so far were predominantly directed to probe bulk superconductivity [162, 168]. Moreover, for the spectra taken in a magnetic field the intermediate state, that occurs below H_c for a finite demagnetization factor, was not taken into account.

In the resistance measurements (partial) superconductivity is observed up to about 0.2 T for $T \rightarrow 0$ (Fig. 5.7), a value that largely exceeds $H_c(0)$ and $H_c^S(0)$. The enhanced $H_c^R(T)$-curves below 1.3 K are quasi pressure independent. By extrapolating the data in this field range to $H_a \rightarrow 0$ with the WHH function a pressure independent $T_c = 1.2$ K is found. Since T_c^S has a pronounced pressure variation the resistive superconducting transitions measured in this field range are not connected to surface superconductivity. Note that for the crystal studied in Ref. [163] it was concluded that the transport experiment does probe surface superconductivity, but these experiments were performed at ambient pressure only. The persistence of superconductivity in resistance measurements in field is puzzling. Possibly it is caused by filamentary superconductivity. Its pressure independence indicates it might not be an intrinsic property of PdTe$_2$.

5.5 Summary and conclusions

We have carried out a high-pressure transport and ac-susceptibility study of superconductivity in the type-I superconductor $PdTe_2$ (T_c = 1.64 K). T_c shows a pronounced variation with pressure: it increases at low pressure, then passes through a maximum of 1.91 K around 0.91 GPa, and subsequently decreases smoothly up to the highest pressure measured, p_{max} = 2.5 GPa. At each pressure, the critical field, $H_c(T)$, follows the characteristic quadratic in temperature depression for type-I superconductivity. Type-I superconductivity is robust under pressure. In view of the absence of structural modifications in our pressure range and the minute change of the c/a-ratio [173], the non-monotonous variation of T_c indicates an intricate role of the dominant phonon frequency, the electron-phonon-coupling parameter and Coulomb pseudopotential used to compute T_c with help of the McMillan formula. This effect has not been captured by band structure calculations so far [170, 175], notably the electron band structure calculations predict a smooth decrease of T_c under pressure [170]. This calls for more elaborate and detailed calculations for pressures up to p_{max} = 2.5 GPa.

The unusual surface superconductivity, first reported at ambient pressure [163], persists under pressure. Surprisingly, for $p \geq 1.41$ GPa the superconducting transition temperature for the surface T_c^S exceeds T_c of the bulk. This tells us surface and bulk superconductivity are distinct phenomena. This is further confirmed by the observation that the phase lines $H_c(T)$ and $H_c^S(T)$ move apart under pressure and no longer intersect for $p \geq 1.41$ GPa. We propose surface superconductivity possibly has a non-trivial nature and originates from topological non trivial surface states. This calls for quantum-oscillation experiments under pressure, possibly enabling one to follow the pressure evolution of the bulk electronic structure and topological surface states.

In the same spirit it will be highly interesting to extend the experiments to higher pressures, especially because a pronounced change in the electronic properties of $PdTe_2$ is predicted to occur in the range 4.7-6.1 GPa: the type-II Dirac points disappear at 6.1 GPa, and a new pair of type-I Dirac points emerges at 4.7 GPa [170]. Thus a topological phase transition may occur in the pressure range 4.7-6.1 GPa. This in turn might have a strong effect on (surface) superconductivity, because the tilt parameter of the Dirac cones passes the critical value of 1 [121, 164, 178]. We conclude further high-pressure experiments on $PdTe_2$ provide a unique opportunity to investigate the connection between topological quantum states and superconductivity.

5.6 Appendix

5.6.1 Hall-effect measurements

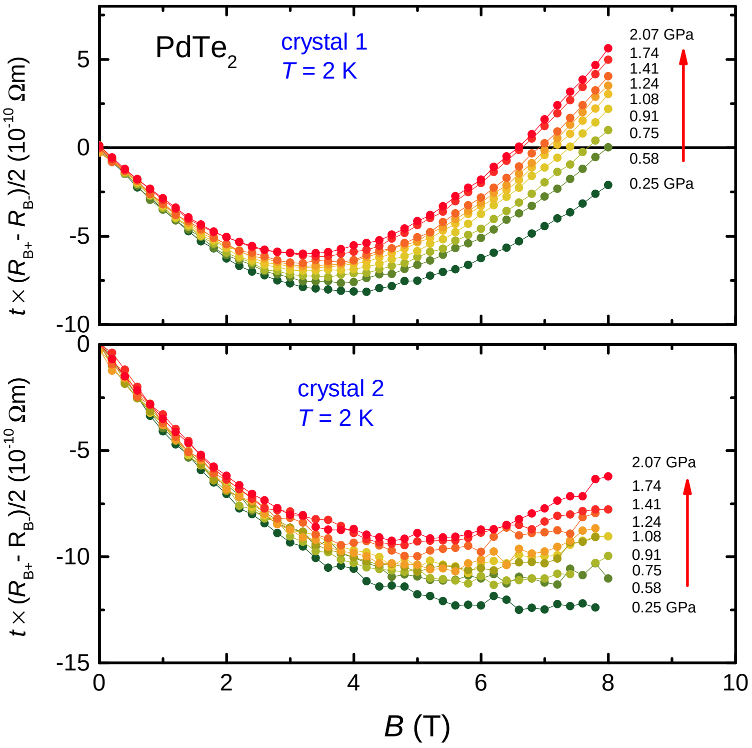

Figure 5.10: Symmetrized Hall resistance multiplied by the crystal thickness t as a function of magnetic field for two PdTe$_2$ crystals at pressures ranging from 0.25 to 2.07 GPa, as indicated. The temperature is 2 K.

In Fig.5.10 we show $t \times R_H$ as a function of the applied field at 2 K at different pressures. Data were collected at temperatures of 2, 10, 50, 150 and 300 K in magnetic fields up to 8 T. Here t is the sample thickness. $R_H(B)$ is a non-linear function indicating the presence of several charge carrier bands, expected from Fermi surface measurements [145, 177]. For crystal 1 the Hall resistance goes through a deep minimum and changes sign in the field range 6-8 T. For crystal 2 the minimum is less pronounced. Overall the $R_H(B)$-curves show a modest, smooth pressure variation, which tells us the nonmonotonous variation $T_c(p)$ is not accompanied by a similar change in the carrier concentration. We estimate the dominant carrier concentration at low fields, n, from the initial linear slope of $R_H(B)$. The results are traced in Fig. 5.11. Upon lowering the temperature from 300 K to 2 K, n drops typically by 20% and 50% for crystal 1 and 2, respectively.

At 2 K, n amounts to 1.5-1.7$\times10^{22}$ cm^{-3} at 0.25 GPa. It varies quasi-linearly with pressure and has increased by ~20% at the highest pressure. No anomalous behavior is observed in low fields around 0.9 GPa, where $T_c(p)$ has a maximum. We also measured the Hall resistance at ambient pressure on a third crystal. The resulting carrier concentration is 0.8$\times10^{22}$ cm^{-3} at 2 K. which is about a factor two smaller compared to the values for crystal 1 and 2.

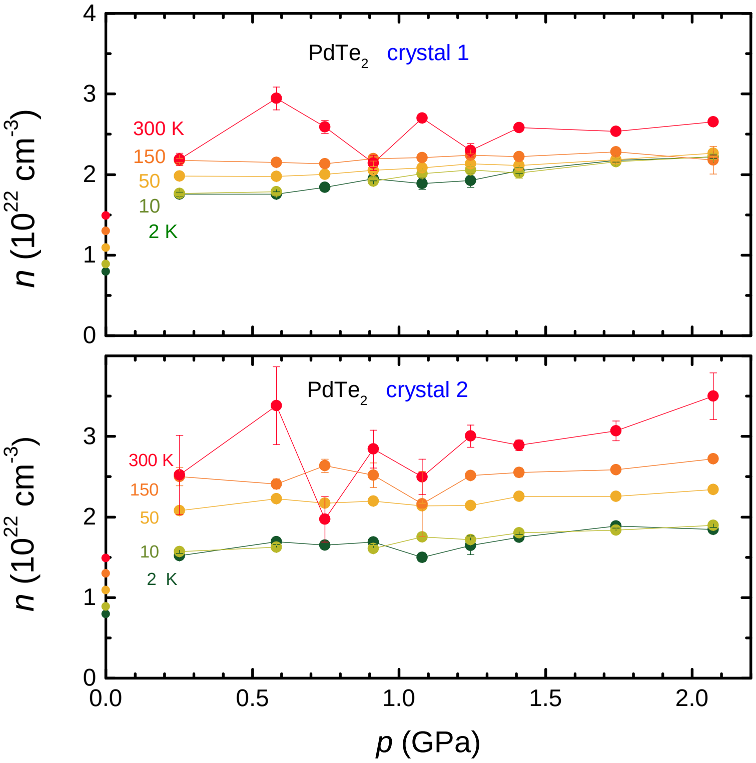

Figure 5.11: Carrier concentration as a function of pressure for two PdTe$_2$ crystals, at temperatures of 2, 10, 50, 150 and 300 K, as indicated. The data at ambient pressure are taken from a third crystal.

5.6.2 Resistance and ac-susceptibility measurements in field

In order to investigate the response of the superconducting phase of PdTe$_2$ to an applied magnetic field, and to construct the field-temperature phase diagram, electrical resistivity and ac-susceptibility measurements were carried out. The resistance as a function of temperature, $R(T)$, was measured using a sensitive resistance bridge (model Linear Research LR700) in a four-point geometry by a low-frequency ac-method with an excitation current $I = 300$ μA. The ac-susceptibility was measured by placing the crystal in a small coil-set with an excitation and pick-up coil, mounted inside the pressure cell. The excitation field was $\mu_0 H_{ac} = 0.0047$ mT. The in-phase and out-of-phase signals were recorded at a frequency of $f_{ac} = 313$ Hz using a lock-in amplifier (EG&G Instruments Model 7260). The applied dc-field, directed in the basal plane of the crystal, was produced by a superconducting magnet. Special care was taken to reduce the remnant field of the superconducting magnet to close to zero, since the PdTe$_2$ crystals show type-I superconductivity. Measurements were carried out at eleven different pressures. The data at 0.25 GPa are reported in the main text. In Fig. 5.12 and Fig. 5.13 the data sets at 1.08 and 2.07 GPa, respectively, are presented.

Pressure 1.08 GPa

The χ_{ac}-data at 1.08 GPa are plotted in the lower panel of Fig. 5.12. The peak just below T_c for the data in small applied fields is due to the differential paramagnetic effect (DPE) and is rapidly depressed with field. It signals the presence of the intermediate state in the bulk of the type-I superconductor. From the shift of the DPE peak we determine the H_c phase boundary. For $H_a > H_c$ large screening signals persist, which we attribute to superconductivity of the surface sheath [163] with a critical field H_c^S. A sizeable screening is still observed at 40 mT. The phase boundaries H_c and H_c^S derived from χ_{ac} are reported in Fig.5.6 (middle panel) in the main text.

The transition to $R = 0$ in small applied fields is sharp and depressed rapidly in fields up to $\sim$ 11 mT. This signals bulk type-I superconductivity. The suppression of T_c with field is shown in Fig.5.7 in the main text. Using a quadratic temperature variation in the range 1.3-1.9 K, we obtain a critical field $H_c(0) = 22$ mT by extrapolation. For larger fields superconductivity is depressed at a much lower rate, the transition broadens and becomes incomplete for $H_a \geq 120$ mT. Signs of superconductivity in $R(T)$ persist up to 200 mT for $T \rightarrow 0$. $H_c^R(T)$ extracted from the upper panel in Fig. 5.12 is reported in Fig.5.7 in the main text.

Pressure 2.07 GPa

The χ_{ac}-data at 2.07 GPa, plotted in the lower panel of Fig. 5.13, show a very different behavior compared to the data at 1.08 GPa. The DPE peak in applied fields is reduced and appears in $\chi_{ac}(T)$ well below the initial diamagnetic step. This implies that surface screening precedes screening due to bulk superconductivity. Thus $T_c^S > T_c^\chi$, where T_c^χ is the bulk superconducting transition temperature. The data points extracted from Fig. 5.13 in this manner define the phase boundaries $H_c(T)$ and $H_c^S(T)$ reported in Fig.5.6 (right panel) in the main text. Screening at the surface is not complete and amounts to 60% only. Note the DPE peak is

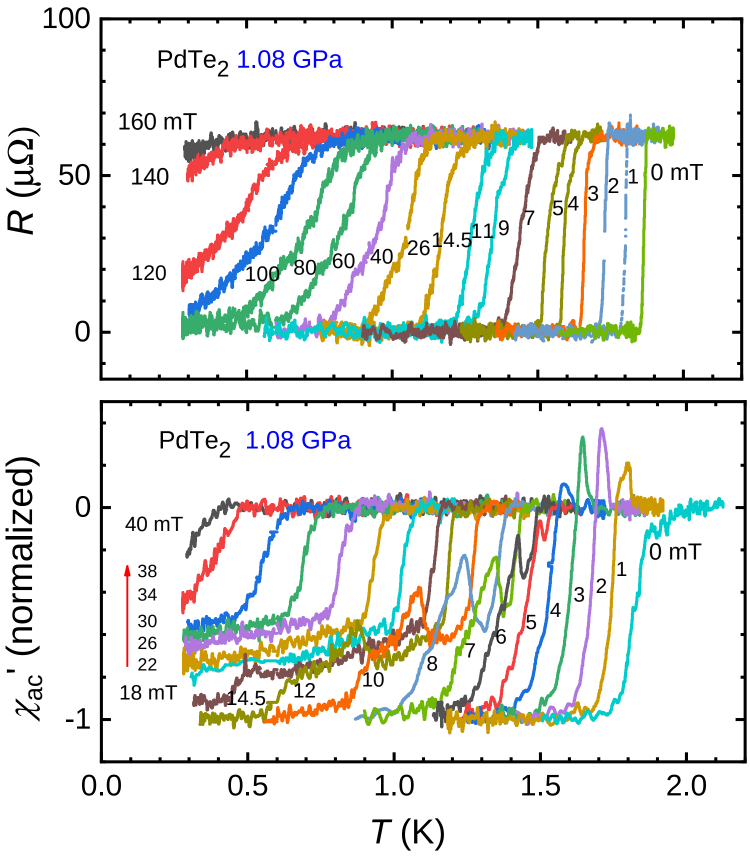

Figure 5.12: Upper panel: Resistance of $PdTe_2$ as a function of temperature at a pressure $p = 1.08$ GPa measured in applied magnetic fields $\mu_0 H_a \parallel I \parallel a$. Curves from right to left are taken in fields of 0, 1, 2, 3, 4, 5, 7, 9, 11, 14.5, 26, 40, 60, 80, 100, 120, 140 and 160 mT. Lower panel: Ac-susceptibility at $p = 1.08$ GPa measured in applied magnetic fields. Curves from right to left in 0 mT to 8 mT with 1 mT steps and in 10, 12, 14.5, 18, 22, 26, 30, 34, 38 and 40 mT.

no longer observed for $H_a > 10$ mT, and $H_c(T)$ (defined by $T_c^{\chi}(H)$) follows the quadratic temperature variation for bulk type-I superconductivity, as explained in the Section 1.3.1.

The resistance data at 2.07 GPa, shown in the upper panel of Fig. 5.13, compare well to the data at 1.08 GPa, except superconductivity in zero field is further depressed from $T_c^R = 1.85$ K at 1.08 GPa to 1.41 K at 2.07 GPa. Consequently, the extrapolated critical field for bulk superconductivity is reduced to $H_c^R(0) = 19$ mT.

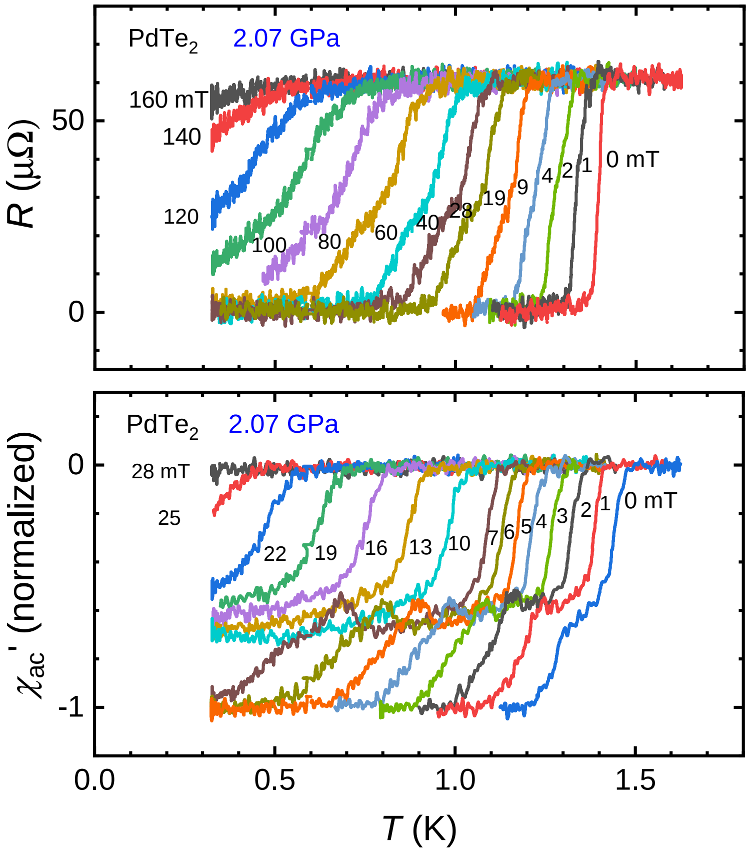

Figure 5.13: Upper panel: Resistance of PdTe$_2$ as a function of temperature at a pressure $p = 2.07$ GPa measured in applied magnetic fields $\mu_0 H_a \parallel I \parallel a$. Curves from right to left are taken in fields of 0, 1, 2, 4, 9, 19, 28, 40, 60, 80, 100, 120, 140 and 160 mT. Lower panel: Ac-susceptibility at $p = 2.07$ GPa measured in applied magnetic fields. Curves from right to left in 0 mT to 7 mT with 1 mT steps and in 10, 13, 16, 19, 22, 25 and 28 mT.

5.6.3 Pressure variation of the critical field

In Fig. 5.14 the pressure variation of the critical fields H_c and H_c^R in the limit $T \to 0$ and at $T = 0.3$ K for H_c^S is presented. The field $H_c(0)$ is representative of bulk superconductivity. It is determined from ac-susceptibility with help of the expression $H_c(T) = H_c(0)[1-(T/T_c)^2]$, where $T_c = T_c^{\chi}$. The $H_c(T)$-curves measured at eleven different pressures are reported in Fig. 5.4. $H_c^R(0)$ is determined from the data in the temperature range $1.3-1.9$ K in Fig. 5.7 by extrapolating $T \to 0$, using the quadratic temperature variation with $T_c = T_c^R$. Note the temperature range in which $H_c^R(T)$ represents type-I superconductivity and follows a quadratic temperature variation is small, since below $T = 1.3$ K $H_c^R(T)$ shows

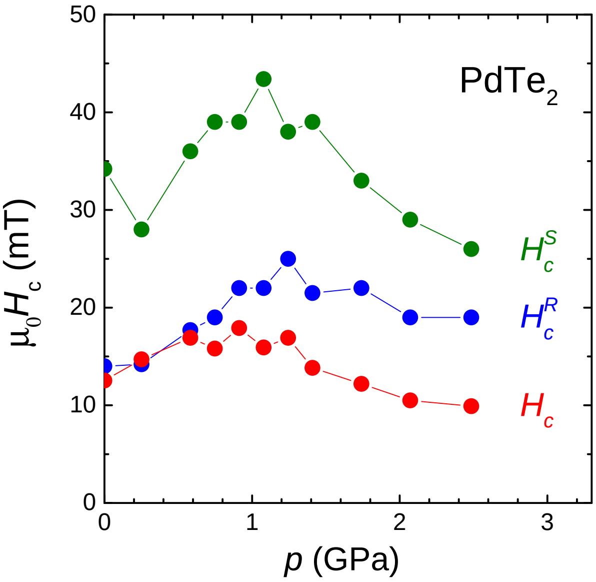

Figure 5.14: Pressure variation of the critical field of PdTe$_2$. H_c (red symbols) represents bulk type-I superconductivity determined by χ_{ac} measurements in the limit $T \to 0$. H_c^R (blue symbols) is determined from resistance measurements by extrapolating the initial low field $H_c^R(T)$-data to 0 K using a quadratic temperature variation. H_c^S (green symbols) represents surface superconductivity at the lowest temperature, $T = 0.3$ K, as extracted from χ_{ac} .

a pronounced upturn (see Fig.5.7 in the main text). Consequently, the fit brings about an uncertainty in $H_c^R(0)$, which explains the overestimated values compared to $H_c(0)$. $H_c^S(0)$ represents the critical field at $T = 0.3$ K for superconductivity of the surface sheath determined by ac-susceptibility. For all three data sets in Fig. 5.14 a maximum in the critical field as a function of pressure is observed near 0.9-1.2 GPa.

Chapter 6

Type-I superconductivity in the Dirac semimetal $PdTe_2$ probed by μSR

The Dirac semimetal $PdTe_2$ *was recently reported to be a type-I superconductor with* $T_c = 1.64$ *K and a critical field* $\mu_0 H_c = 13.6$ *mT. Since type-I superconductivity is unexpected for binary compounds, we have conducted muon spin rotation experiments to probe the superconducting phase on the microscopic scale via its intermediate state. For crystals with a finite demagnetization factor,* N*, the intermediate state forms in applied fields* $(1 - N)H_c < H_a < H_c$*. We have carried out transverse field muon spin rotation measurements on a thin disk-like crystal with the field perpendicular to (*$N_\perp = 0.86$*) and in the plane (*$N_\parallel = 0.08$*) of the disk. By analysing the* μ*SR signal we find that the volume fraction of the normal domains grows quasi-linearly with applied field at the expense of the Meissner domain fraction. This then provides solid evidence for the intermediate state and type-I superconductivity in the bulk of* $PdTe_2$*.*

This chapter has been published as Phys. Rev. B 100 224501 (2019).

6.1 Introduction

The large family of layered transition metal dichalcogenides is extensively studied because of their fascinating electronic properties. One of the modern-day research interests is a non-trivial nature of the electronic band structure, which may result in topology driven quantum states. Density functional calculations show, for instance, that selected transition metal dichalcogenides host generic three-dimensional type-II Dirac fermion states [128, 129, 130, 161]. In a type-II Dirac semimetal the Dirac cone, which embodies the linear energy dispersion, is tilted, and the Hamiltonian breaks Lorentz invariance [128]. Here we focus on the exemplary material PdTe$_2$. Extensive electronic structure calculations combined with angle resolved photoemmission spectroscopy (ARPES) demonstrate a type-II Dirac semimetallic state with the Dirac point at $\sim$ 0.6 eV below the Fermi energy [121, 120, 132, 161, 162]. Another interesting property of PdTe$_2$ is that it superconducts below $T_c = 1.6$ K [131]. In a type-II Dirac semimetal the Dirac point is the touching point of the electron and hole pockets and a nearly flat band may form near the Fermi level. This could promote superconductivity, which in turn prompts the question whether superconductivity has a topological nature [121, 163].

In a recent paper Leng *et al.* [163] reported a magnetic and transport study on single crystalline PdTe$_2$ and concluded superconductivity shows type-I behavior. This result is surprising, because binary compounds when superconducting exhibit in general type-II behavior. Until today this rare phenomenon has been documented convincingly for about a dozen binary or ternary compounds only (see Ref. [179]). In the case of PdTe$_2$ evidence for type-I behavior is provided by (i) the dc-magnetization curves as function of the applied field, $M(H_a)$, that show the presence of the intermediate state between $(1-N)H_c < H_a < H_c$, where N is the demagnetization factor and H_c the critical field with $\mu_0 H_c(0) = 13.6$ mT, (ii) the differential paramagnetic effect (DPE), that shows up as a peak in the ac-susceptibility in applied dc-field, just below T_c, and (iii) the quadratic temperature variation of the thermodynamic critical field $H_c(T) = H_c(0)[1-(T/T_c)^2]$. The value of the Ginzburg-Landau parameter $\kappa = \lambda/\xi$, where λ is the magnetic penetration depth and ξ the superconducting coherence length, amounts to 0.09-0.29 [163, 166] and is smaller than $1/\sqrt{2}$, the boundary value for type-I and type-II behavior. The superconducting phase has further been characterized by heat capacity [165], scannning tunneling microscopy/spectroscopy (STM/STS) [162, 168, 180], and magnetic penetration depth measurements [166, 167]. The specific heat data confirm conventional weak-coupling Bardeen-Cooper- Schrieffer superconductivity with a ratio $\Delta c/\gamma T_c \approx 1.52$, which is close to the weak-coupling value 1.43. Here Δc is the size of the step in the specific heat at T_c and γ the Sommerfeld coefficient. The

STM/STS spectra taken in zero magnetic field point to a fully-gapped superconducting state, without any in-gap states. Finally, the magnetic penetration depth, $\lambda(T)$, shows an exponential temperature variation for $T/T_c < 0.4$ consistent with a fully-gapped superconducting state.

Nonetheless, several curious features have come to the fore in the superconducting state of $\mathrm{PdTe_2}$. First of all, ac-susceptibility measurements in a small driving field have revealed large screening signals in applied dc-fields $H_a > H_c$ (Ref. [163]) (here H_a is directed along the a-axis). This has been attributed to superconductivity of the surface sheath [163]. Screening persists up to the critical field $\mu_0 H_c^S(T \to 0) = 34.9$ mT. Surface superconductivity is not of the standard Saint-James - de Gennes type, which has a critical field $H_{c3} = 2.39 \times \kappa H_c$ (Ref. [141]). In fact when $\kappa < 0.42$, $H_{c3} < H_c$ and Saint-James - de Gennes surface superconductivity should not occur. This opens up the possibility that superconductivity of the surface layer has a different nature and originates from the topological surface states that were detected by ARPES [120, 132]. Another striking feature is that electrical resistance measurements reveal superconductivity to survive up to fields that are much higher, typically $\mu_0 H_c^R(0) = 0.3$ T $\gg \mu_0 H_c^S(0) > \mu_0 H_c(0)$ (Ref.[163]). The resulting complex phase diagram in the $H - T$ plane shows some similarities with the diagrams reported for the superconductors $\mathrm{LaRhSi_3}$ [140] and $\mathrm{ZrB_{12}}$ [181]. However, in these cases the unusual diagram is attributed to a field-induced change from type-I to type-II superconductivity below a conversion temperature $T^* < T_c$. These materials are called type-II/1 superconductors, and have a κ-value close to $1/\sqrt{2}$ (Ref. [156]).

Another puzzling aspect comes from STM/STS measurements in applied dc fields. Das *et al.* [168] have investigated the closure of the gap for a field along the c-axis at $T/T_c = 0.23$ and find that the superconducting gap predominantly is suppressed at a critical field $\mu_0 H_c(0) \approx 25$ mT. However, they also find regions on the surface of the crystal where significantly larger fields are required to suppress superconductivity, typically in the range 1-4 T. These STM/STS results were taken a step further by Sirohi *et al.* [180] who reported a distinct behavior in the spectra taken in the low and high H_c regions. They concluded that the observed spatial distribution of critical fields is due to mixed type-I and type-II superconducting behavior, which in turn stems from electronic inhomogeneities visible in the spectra in the normal state. A third STM/STS characterization was carried out by Clark *et al.* [162] Since these authors observe a vortex core in a field of 7 mT they claim $\mathrm{PdTe_2}$ is a type-II superconductor, and report an upper field critical field $\mu_0 H_{c2} = 20$ mT. We remark, that in the STM/STS work reported so far, evidence of an Abrikosov vortex lattice has not been produced. More recently, mechanical and soft point contact spectroscopy (PCS) data were also taken as evidence for mixed type-I and type-I superconductivity on the surface [182]. A possible issue in all these experiments is that the applied field was directed perpendicular to a flat crystal, which involves a large demagnetization factor and the formation of the field-induced intermediate state. This has not been addressed in the aforementioned STM/STS papers.

These conflicting results warrant the investigation of the superconducting phase of PdTe$_2$ on the microscopic scale. For this the μSR technique is extremely well suited, because it is a local probe which permits to determine whether regions with distinct magnetic properties are present in the crystal [65, 183]. μSR is also a well-established technique to measure the penetration depth of type-II superconductors [66]. In the transverse field configuration the precession of the muon (μ^+) spin is damped by the local field distribution of the vortex lattice. From the resulting Gaussian damping rate, $\sigma(T)$, the magnetic penetration depth, $\lambda(T)$, can be derived. In a type-I superconductor in the Meissner phase, the application of a transverse field will not give rise to precession of the μ^+ spin because the magnetic induction in the crystal is zero. However, for applied fields larger than $(1-N)H_c$ the intermediate state is generated and a macroscopic phase separation occurs in Meissner and normal state domains. The field in the normal regions is equal to the critical field H_c. Consequently, μ^+ spin precession will occur in the normal-phase fraction of the crystal. By fitting the μSR signal with the appropriate muon depolarization function, one can determine the Meissner and normal phase fractions in the crystal.

Although a powerful technique, μSR on type-I superconductors has not been explored in much detail. Studies of the intermediate state in elemental superconductors are scarce and concise [184, 185, 186, 187, 188, 189, 190]. The most recent work by Karl *et al.* (Ref. [190]), however, presents a comprehensive review of the technique and an in-depth analysis of the μSR signal in the intermediate phase of a β-Sn sample. Binary and ternary compounds that have been scrutinized for type-I superconductivity include LaNiSn [191], LaRhSi$_3$ [192], LaIrSi$_3$ [193], LaPdSi$_3$ [194], and very recently AuBe [195, 196].

Here we report transverse field muon spin rotation measurements in the superconducting phase of PdTe$_2$. Experiments were performed on a thin disk-like crystal in two configurations: (i) with the field perpendicular to the plane of the disk ($N_\perp = 0.87$) and (ii) with the field in the plane of the disk ($N_\parallel = 0.08$). By analysing the asymmetry of the μSR signal we find that the normal phase volume fraction grows quasi-linearly with applied field at the expense of the Meissner phase fraction. This provides solid evidence for the intermediate state and type-I superconductivity in the bulk of our PdTe$_2$ crystal.

6.2 Experiment

The $PdTe_2$ crystal used for the μSR experiment was taken from a single-crystalline boule prepared by the modified Bridgman technique[59]. Its single-crystalline nature was checked by Laue backscattering. Powder X-ray diffraction confirmed the trigonal CdI_2 structure (spacegroup $P\bar{3}m1$). Scanning electron microscopy (SEM) with energy dispersive X-ray (EDX) spectroscopy showed the proper 1:2 stoichiometry within the experimental resolution of 0.5%. The superconducting properties of small crystals cut from the single-crystalline boule were measured by dc-magnetization and ac-susceptibility [163]. The Meissner volume fraction for a bar-shaped crystal cut along the a-axis, and $H_a \parallel a$, amounts to 93% after correcting for demagnetization effects [163]. The crystal used in the present experiment is cut from the same region of the single-crystalline boule and has a disk-like shape, with the c-axis perpendicular to the plane of the disk. Its thickness equals 0.65 mm and the diameter is 10.0 mm. However, a small piece was removed and cut from the disk along the a-axis, which reduced the size in the perpendicular a^*-direction ($\perp a$) to 6.8 mm. This causes additional field inhomogeneities near the edges of the sample, notably for the configuration with the field in the plane of the disk. It also thwarts a precise calculation of the demagnetization factors. With appropriate approximations of the sample shape the estimated values are $N_\perp = 0.87 \pm 0.02$ and $N_\parallel = 0.08 \pm 0.02$ (see Appendix 1). These values have been calculated for a completely diamagnetic state, $\chi = -1$.

The crystal was attached with its largest flat surface (*i.e.* the plane of the disk) utilizing vacuum grease (Apiezon N) to a thin copper foil that is supported by a fork-shaped copper holder. A thin layer of Kapton foil was wrapped around the sample and holder to mechanically fix the crystal. The holder was attached to the cold finger of a helium-3 refrigerator (HELIOX, Oxford Instruments) and μSR spectra were taken in the temperature range $T = 0.25 - 5.00$ K. The crystal is oriented with the plane of the disk perpendicular to the muon beam and the area for the implanted muons is $\sim$55 mm^2.

Muon spin rotation (μSR) experiments were carried out with the Multi Purpose Surface Muon Instrument DOLLY installed at the πE1 beamline at the SμS facility of the Paul Scherrer Institute. The technique employs the decay probability of spin-polarized muons that are implanted in the crystal. In the case of $PdTe_2$ (density 8.3 g/cm^3) the muons typically penetrate over a distance of 133±26 μm, and thus probe the bulk of the crystal. In the presence of a local or applied field at the muon stopping site the muon spin will precess around the field direction with an angular frequency $\omega_\mu = \gamma_\mu B_{loc}$, where γ_μ is the muon gyromagnetic ratio ($\gamma_\mu/2\pi = 135.5$ MHz/T). The subsequent asymmetric decay process is monitored by counting the emitted positrons by scintillation detectors that are placed at opposite directions in the muon-spin precession plane [65, 183, 66]. The parameter

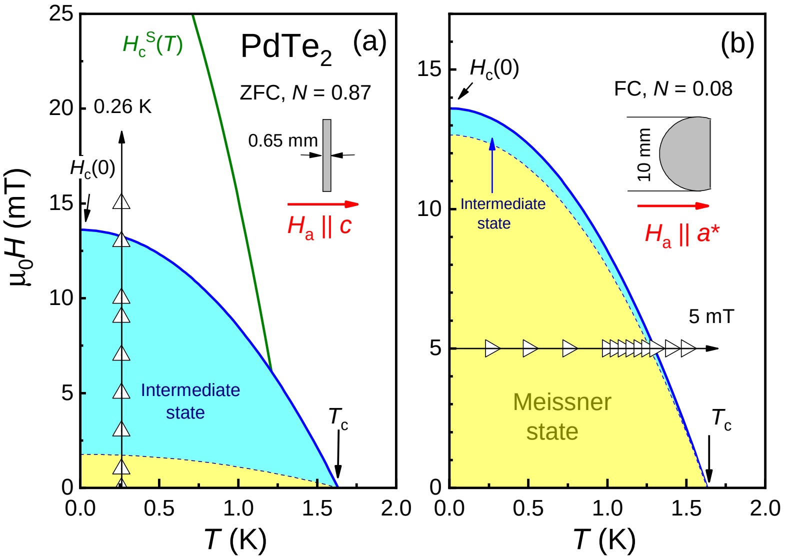

Figure 6.1: Field and temperature scan procedure of the superconducting phase diagram of PdTe$_2$. The phase boundary $H_c(T) = H_c(0)[1-(T/T_c)^2]$ with $\mu_0 H_c(0) = 13.6$ mT and $T_c = 1.64$ K is taken from Ref. [163]. The blue colored area indicates the intermediate phase for $(1-N)H_c < H_a < H_c$, with $N = N_\perp = 0.87$ (a) and $N = N_\parallel = 0.08$ (b) and the yellow area the Meissner phase. (a) After zero field cooling (ZFC) down to $T = 0.26$ K, spectra were recorded by increasing the field $H_a \parallel c$ step-wise at values denoted by the up-triangles. (b) After cooling down to 0.26 K in a field $H_a \parallel a^*$ of 5 mT, spectra were recorded at the temperatures indicated by the side triangles. In the upper part of (a) and (b) the sample and field geometry is sketched. The solid green line in (a) indicates the region below which surface superconductivity is observed [163]. Note the vertical scale is different in (a) and (b).

of interest is the muon spin asymmetry function, $A(t)$, which is determined by calculating $A(t) = (N_1(t) - \alpha N_2(t))/(N_1(t) + \alpha N_2(t))$, where $N_1(t)$ and $N_2(t)$ are the positron counts of the two opposite detectors, and α is a calibration constant. In our case α is close to 1.

Transverse field (TF) experiments were performed with the magnetic field applied parallel and perpendicular to the crystal plane. In the first configuration the muon spin is along the beam direction, the field in the horizontal plane at right angles to the beam (and in the plane of the disk, $N = N_\parallel$), and the decay positrons are detected in the backward and forward counters. In the second case the beam-line is operated in the muon spin-rotated mode, the applied field is along the beam direction (perpendicular to the plane of the disk, $N = N_\perp$), and the decay positrons are collected in the left and right counters. In the spin-rotated mode the muon spin is directed $\sim 45°$ out of the horizontal plane. This results is a reduced asymmetry function ($A \approx 0.18$) with respect to the full asymmetry ($A \approx 0.23$) in the non-spin-rotated mode. The μSR time spectra were analysed with the software packages WIMDA [197] and MUSRFIT [198].

6.3 Results and Analysis

In order to investigate the presence of the intermediate state we have scanned the superconducting phase diagram as depicted in Fig. 6.1. In Fig. 6.1(a) we show the case where the sample is cooled in zero field (ZFC) after which the field, directed perpendicular to the plane of the disk, is increased in eight steps to a value $H_a > H_c$. In this case the intermediate state covers a large region of the phase diagram. In Fig.6.1(b) we show the case where the sample is cooled in 5 mT (FC), applied in the plane of the disk, after which the temperature is raised in eleven steps to $T > T_c$ (at 5 mT). In this case the intermediate state region is expected to be small.

6.3.1 Field perpendicular to the plane of the disk

In Fig. 6.2 we show three typical TF μSR spectra at $T = 0.26$ K recorded during step-wise increasing the field to 15 mT. In panel (a) no field is applied and muon spin precession is absent, the muons probe the Meissner phase. In panel (b) the applied field is raised to 9 mT. Now a clear spin precession is visible, but with a reduced asymmetry. The superconducting volume has shrunk. The spin precession frequency corresponds to a local field $B_{loc} = 13.1 \pm 0.1$ mT, which is equal to $\mu_0 H_c$ at 0.26 K. This shows the sample is in the intermediate state. Lastly, in panel (c) the field is raised to 15 mT $> \mu_0 H_c$ and all muons show a precession frequency corresponding to $B_a = B_{loc} = 15$ mT, as expected in the normal state.

The μSR response $A(t) = AP(t)$, where $P(t)$ is the muon depolarization function, in panel (a) of Fig. 6.2 is well described by a Gaussian Kubo-Toyabe function

$$A_{KG}(t) = A_0[\frac{1}{3} + \frac{2}{3}(1 - \sigma_{KG}^2 t^2)\exp(-\frac{1}{2}\sigma_{KG}^2 t^2)] \tag{6.1}$$

Here A$_0$ is the initial asymmetry and σ_{KG} the depolarization rate. The fit is shown in panel (a) by the solid blue line. The fit parameters are $A_0 = 17.6 \pm 0.1$ and $\sigma_{KG} = 0.052 \pm 0.003$ μs^{-1}. The small depolarization rate is attributed to a Gaussian distribution of static nuclear moments. In the normal phase, panel (c), the μSR response is best fitted with the function (solid black line):

$$A_N(t) = A_0 \exp(-\frac{1}{2}\sigma_N^2 t^2)\cos(\gamma_\mu B_a t + \phi_N) \tag{6.2}$$

where σ_N is a Gaussian damping rate, B_a the applied field and ϕ_N a phase factor. The fit parameters are $A_0 = 17.5 \pm 0.1$ and $\sigma_N = 0.075 \pm 0.004$ μs^{-1}. The small damping rate is attributed to the field distribution of nuclear moments as well, which is considered to be static in the μSR time window.

In an applied field in the superconducting phase, panel (b), best fits are obtained with a three component function (in the following we use B_a and B_c for the applied and critical field rather than H_a and H_c)

$$\begin{aligned} A(t) = A_0[f_S(\frac{1}{3} + \frac{2}{3}(1-\sigma_{KG}^2 t^2)\exp(-\frac{1}{2}\sigma_{KG}^2 t^2)) \\ + f_N \exp(-\frac{1}{2}\sigma_N^2 t^2)\cos(\gamma_\mu B_c t + \phi_N) \\ + f_{bg}\exp(-\frac{1}{2}\sigma_{bg}^2 t^2)\cos(\gamma_\mu B_a t + \phi_{bg})] \end{aligned} \tag{6.3}$$

The third term, which we give the label 'background' for the moment, is small and accounts for muons that precess in the applied field at the angular frequency $\omega = \gamma_\mu B_a$, and σ_{bg} and ϕ_{bg} are the related damping and phase factor, respectively. $f_S = A_S/A_0$, $f_N = A_N/A_0$ and $f_{bg} = A_{bg}/A_0$ are the volume fractions related to the superconducting domains, normal domains, and the background term, respectively. $A_0 = A_S + A_N + A_{bg}$ is the full experimental asymmetry, and was kept constant in the fitting procedure at the normal state value 17.50. The fit parameters at 9 mT (panel (b)) are: $f_S = 0.34 \pm 0.01$ (solid blue line), $f_N = 0.56 \pm 0.01$ and $\sigma_N = 0.246 \pm 0.049$ μs^{-1} (solid green line), and $f_{bg} = 0.10 \pm 0.01$ and $\sigma_{bg} = 0.504 \pm 0.043$ μs^{-1} (solid pink line). Here we have fixed $\sigma_{KG} = 0.052$ μs^{-1}. We remark that the Gaussian damping in the normal domains, $\sigma_N \approx 0.246 \pm 0.049$ μs^{-1}, is larger than the value extracted from the normal state fit, see panel (c). This is not unexpected given the complicated domain patterns that can arise in the intermediate state [199]. The field variation of the relaxation rates σ_{KG}, σ_N and σ_{bg} is reported in the section Appendix 2. We will address the background term in the Discussion section.

In order to follow the evolution of the intermediate state with increasing magnetic field it is illustrative to inspect the Fast Fourier Transforms (FFT) of the μSR time spectra. The FFT amplitudes are shown in a three-dimensional (3D) plot in Fig. 6.3. The magnetic field distributions have a sharp peak at $B = 0$, which is due to the superconducting volume fraction. For $B_a = 5$ mT a second peak appears at a field $B = B_c > B_a$. This magnetic intensity is due to the normal

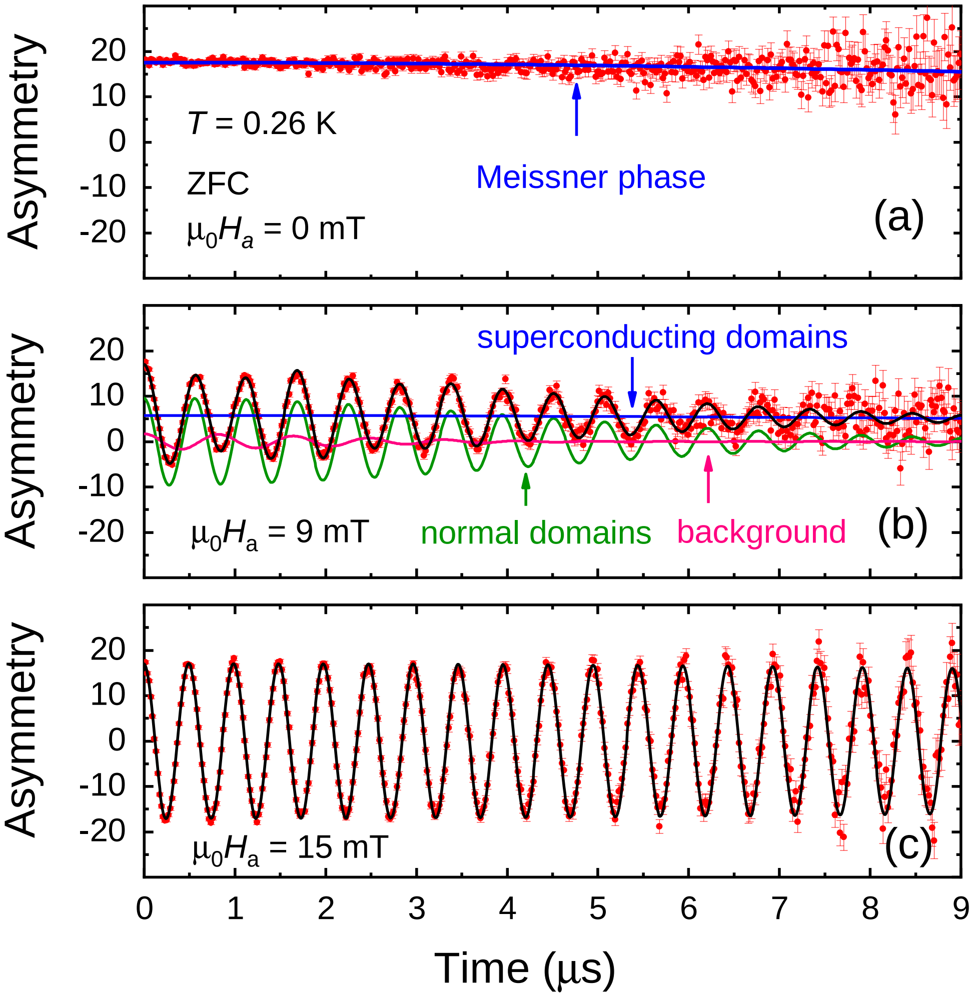

Figure 6.2: μSR spectra collected at $T = 0.26$ K in ZF and in applied fields of 9 mT and 15 mT directed perpendicular to the sample plane. (a) Zero-field. The solid blue line is a fit to the Gaussian Kubo-Toyabe function Eq. 6.1. (b) TF = 9 mT. The black line is a fit to the three component function Eq. 6.3. The different components, due to superconducting domains, normal domains and background, are shown by the solid blue, green and pink lines, respectively. (c) TF = 15 mT. The black solid line is a fit to the depolarization function Eq. 6.2. See text for fit details.

domains. It shows the crystal is phase separated in normal and superconducting domains, as expected for the intermediate state. By further increasing the field, the peak at B_c grows, while the peak at $B = 0$ decreases in intensity and vanishes at $B_a = B_c$. Eventually, for $B_a = 15$ mT $> B_c = 13.1 \pm 0.1$ mT, the FFT shows a peak at the applied field only. In all FFT's a low-intensity hump is visible at the applied field as well. This field distribution corresponds to the background term.

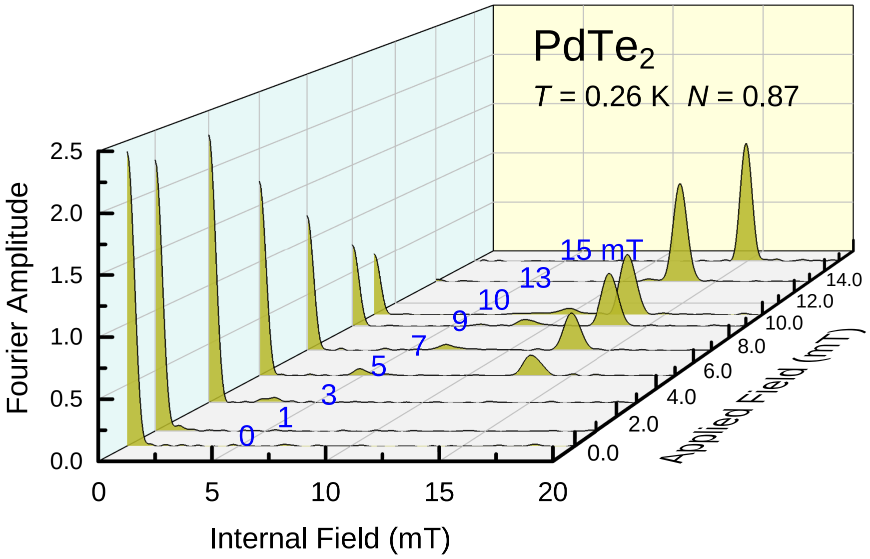

Figure 6.3: Magnetic field distribution in the PdTe$_2$ crystal at $T = 0.26$ K obtained by FFT for fields applied perpendicular to the sample plane. The field values are given in blue colored numbers. In the intermediate state two peaks are present at $B = 0$ and at $B = B_c > B_a$. The weak intensity at $B = B_a$ signals the background contribution.

In order to produce a quantitative analysis of the growth of the intermediate phase we have fitted the μSR spectra in applied fields to Eq. 6.3, as illustrated in Fig. 6.2(b). In Fig. 6.4 we trace the fit parameters f_S, f_N and f_{bg}. In the Landau scenario the intermediate state is predicted to occur in the field range $(1-N)H_c < H_a < H_c$ and its volume fraction grows linearly $f_N(H_a) = (H_a-(1-N)H_c)/NH_c$ (Ref. [200]). Overall, our results comply with the simple model, but for small fields the quasi-linear behavior does not extend all the way to $\mu_0 H_a = (1-N)\mu_0 H_c = 1.9$ mT, but rather to 3 mT. This we attribute to the non ideal shape of the crystal and field inhomogeneities near the edge, which seem to provide a weak barrier for the flux to enter. To conclude this section we remark that the value of $B_c = 13.1 \pm 0.1$ mT at $T = 0.26$ K obtained by μSR for $H_a \parallel c$, is close to the value of 13.3 ± 0.1 mT for $H_a \parallel a$ (Ref. [163]).

6.3.2 Field in the plane of the disk

A second set of spectra was taken after field cooling in 5 mT to a base temperature of 0.26 K, followed by stepwise heating the crystal to above T_c, as indicated in Fig. 6.1(b). Here the field was applied in the plane of the disk. It is instructive to

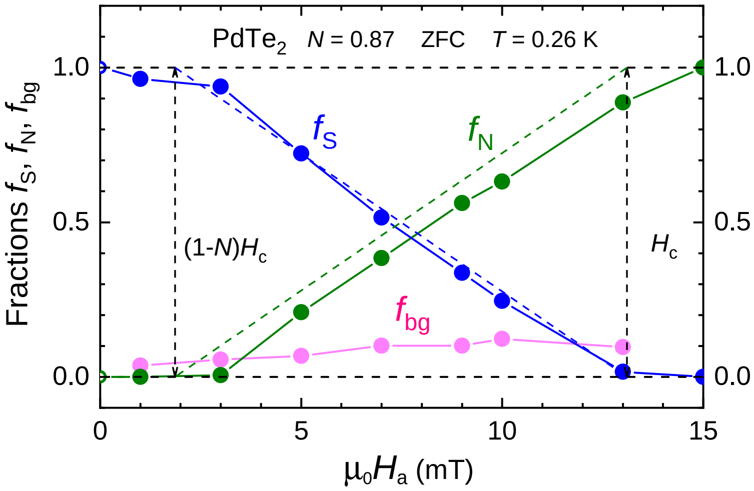

Figure 6.4: Field variation of the superconducting f_S (blue symbols), normal f_N (green symbols) and background f_{bg} (pink symbols) volume fractions obtained by fitting the μSR spectra. The open symbols are ZFC at $B = 0$. The vertical dashed lines at $(1 - N)H_c$ and H_c bound the region in which the intermediate state is expected for $N_\perp = 0.87$. The dashed blue and green lines show the expected linear field variation of the superconducting and normal volume fractions. The error bars in f_S, f_N and f_{bg} are smaller than the size of the symbols. The temperature is 0.26 K.

first inspect the 3D graph with the FFT's shown in Fig. 6.5. The large peaks at $B = 0$ signal the superconducting volume fraction. Surprisingly, after field cooling a tiny fraction of the crystal is in the intermediate state already, as validated by the weak magnetic intensity at $B = B_c = 13.0 \pm 0.1$ mT (at 0.26 K) $> B_a$. Upon increasing the temperature this fraction remains small up to 1.1 K. For higher temperatures the magnetic intensity at B_c grows rapidly, while the peak at $B = 0$ shows the opposite behavior. This shows the bulk of the crystal converts to the intermediate state. The temperature variation of B_c follows the standard quadratic expression $B_c(T) = B_c(0)[1 - (T/T_c)^2]$, here $B_c(0) = 13.3 \pm 0.1$ mT and $T_c = 1.53$ K. These values obtained for $H_a \parallel a^*$ are a few percent smaller than those reported in Ref. [163] for $H_a \parallel a$: $B_c(0) = 13.6$ mT and $T_c = 1.64$ K. The low-intensity hump at $B_a = 5$ mT below T_c is attributed to the background term. For $T > T_c$ the FFT peak at 5 mT is large and characterizes the paramagnetic normal-state volume of the crystal.

In Fig. 6.6 we show three typical μSR spectra from the temperature run in 5 mT together with the fit results using Eq. 6.2 and 6.3. Here the total experimental asymmetry $A_0 = 23.2 \pm 0.1$. At 0.26 K, panel (a), the solid blue line describes the large Meissner volume, with $\sigma_{KG} = 0.033 \pm 0.001$ μs^{-1}. A tiny volume fraction

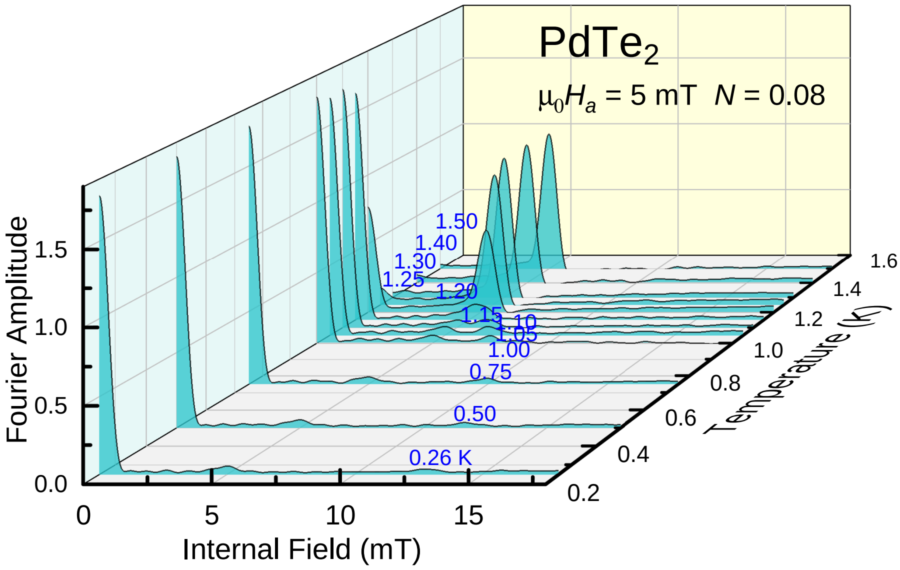

Figure 6.5: Magnetic field distribution in the PdTe$_2$ crystal after FC in $B_a = 5$ mT directed in the plane of the disk at different temperatures as indicated. The large peak at $B = 0$ corresponds to the superconducting volume fraction. The weak intensity at $B_c(T)$ is due to a tiny part of the crystal that is already in the intermediate state at the lowest temperature (0.26 K). Upon approaching T_c the whole crystal converts to the intermediate phase. The small peak that remains at $B = B_a$ signals the background contribution.

with normal domains ($B_c = 13.0$ mT) shows up in the fit as well (solid green line), which indicates a tiny part of the crystal is in the intermediate state. At 1.2 K, panel (b), the normal state domains occupy about half of the crystal's volume. This is shown as the solid green line, which is the Gaussian damped oscillatory component with $\sigma_N = 0.080 \pm 0.015$ μs^{-1}. At 1.5 K, panel (c), the crystal is the normal state. The data above T_c are well fitted by Eq. 6.2 with the small relaxation rate $\sigma_N = 0.046 \pm 0.005$ μs^{-1} (black solid line). In Fig. 6.7 we trace the different volume fractions as a function of temperature obtained by fitting all the spectra. Clearly, during field cooling some flux remains trapped in the crystal, resulting in a superconducting volume fraction $f_S \simeq 0.90$. The tiny volume fraction with normal domains (internal field B_c) does not vary with temperature below $\sim$ 1.1 K and equals $f_N \simeq 0.02$. This implies that the Meissner fraction in this bulky sample occupies $\sim$ 90% of its volume, which may be compared with the value of 93% obtained for a small crystal measured via dc-magnetization [163]. The presence of a tiny intermediate state fraction is most likely related to the edges of the crystal that may result locally in a large demagnetization factor. Upon raising the temperature the bulk of the crystal transforms to the intermediate state above

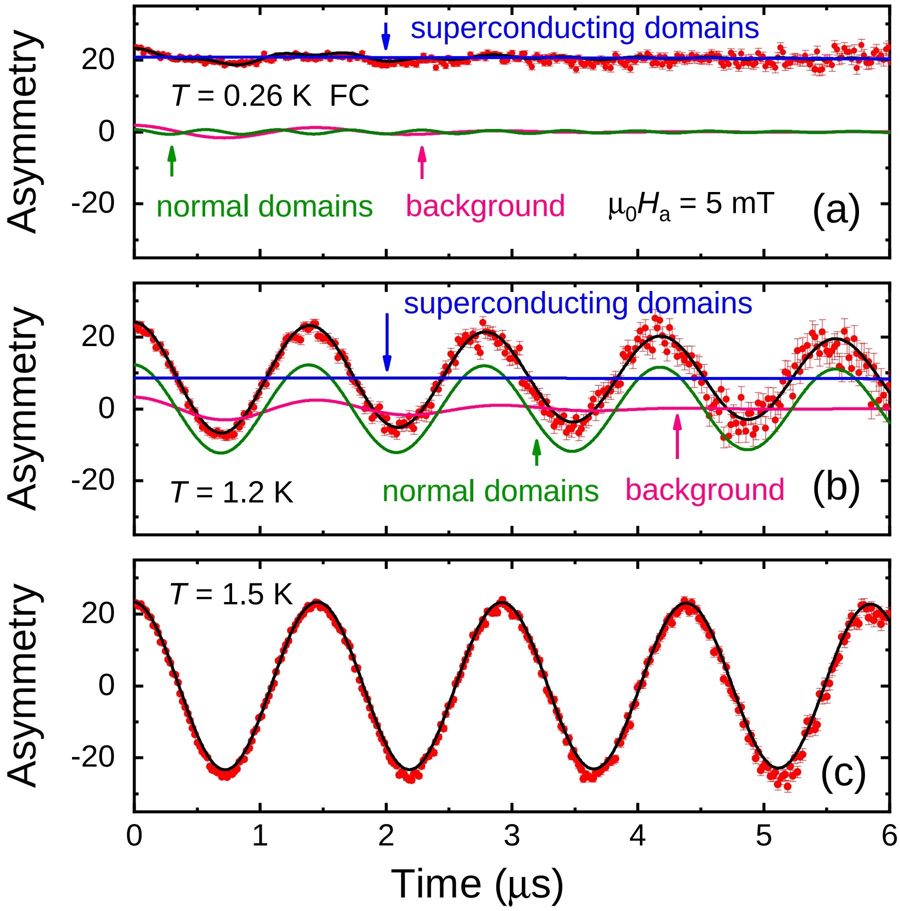

Figure 6.6: μSR spectra collected in a field $H_a = 5$ mT directed in the plane of the sample at 0.26 K, 1.2 K and 1.5 K. The sample is field cooled. In (a) and (b) the black line is a fit to the three component function Eq. 6.3. The different components, due to superconducting domains, normal domains and background, are shown by the solid blue, green and pink lines, respectively. In (c) the black solid line is a fit to the muon depolarization function Eq. 6.2. See text for fit details.

$\sim$ 1.1 K. While f_N grows steeply, f_S decreases. In Fig. 6.7 we have indicated the borders of the intermediate phase by the vertical dashed lines at $T_{IM} = 1.14$ K and $T_c = 1.25$ K. The temperature at which the transformation starts is lower than expected on the basis of the demagnetization factor $N = 0.08$. We remark the phase transformation here takes place as a function of temperature which apparently gives rise to a broadened local field distribution which can be captured by an effective demagnetization factor N_{eff}. With $T_{IM} = 1.14$ K, we calculate $N_{eff} = 0.16$.

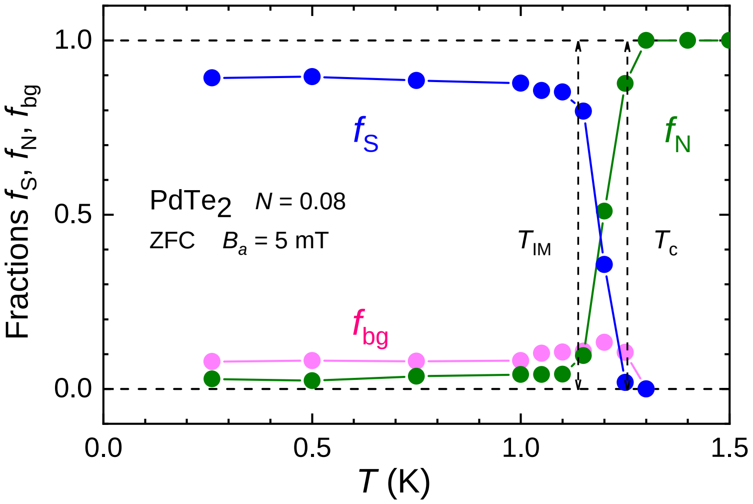

Figure 6.7: Temperature variation of the superconducting f_S (blue symbols), normal f_N (green symbols) and background f_{bg} (pink symbols) volume fractions obtained by fitting the μSR spectra using Eq. 6.3 (FC 5 mT directed in the plane of the disk). The vertical dashed lines at T_{IM} and T_c bound the region in which the intermediate state in the bulk of the crystal is found.

6.4 Discussion

The most important conclusion that can be drawn from our μSR experiments is that the bulk of our PdTe$_2$ crystal exhibits type-I superconductivity. Solid evidence for this is provided by the detection of the intermediate phase. Here we use the muon as a local probe of the bulk on the microscopic level. It is of interest to provide a lower bound of the crystal volume that is occupied by type-I superconductivity. It cannot simply be taken equal to the ZFC Meissner volume, $f_S = 1$, deduced from Fig. 6.2(a), because muons stopping in a (tiny) non-superconducting part of the crystal will experience a similar Gaussian Kubo-Toyabe depolarization as muons in the superconducting part, and thus cannot be distinguished. However, an estimate can be made by considering the intermediate phase fraction, $f_{IM} = f_S + f_N$. From the data in Fig. 6.4 a lower bound for f_{IM} can be obtained by linearly extrapolating $f_N(H_a)$ to H_c, where $f_S = 0$. We find $f_N = f_{IM} = 0.92$. On the same grounds, $f_S = f_{IM} = 0.94$ at the start of the linear growth of f_N. This tells us type-I superconductivity occupies at least 92% of the crystal's volume.

Next we address the background term that gives rise to the remaining volume fraction (5-10%) due to the third component in Eq. 6.3, *i.e.* muons that precess at the frequency of the applied field. Since the muons and decay positron events are collected in the so-called VETO mode, the contribution from positrons arising from muons that do not stop in the sample will be small. Besides, the damping rate σ_{bg} varies with field and temperature and attains values that are too large to stem from the usual background components, such as the sample holder and cryostat. This indicates a local broad field distribution, due to an intrinsic source of inhomogeneities related to type-I superconductivity. In general the penetration or expulsion of flux in a type-I superconductor is a complicated process, and the domain pattern in the intermediate state can be diverse and complex [199]. Moreover, the demagnetization factor in the crystal is not uniform, especially near the edges. This brings about additional internal field inhomogeneities, as illustrated by the tiny intermediate state fraction observed with the field in the plane of the disk.

Another aspect is that the superconducting and normal domains in the intermediate state are separated by domain walls. The width of the domain wall [199] is of the order $\delta \sim \xi - \lambda \approx 1.3$ μm [166]. In the ideal case of a laminar domain pattern an estimate for the volume fraction of the domain walls is $f_{DW} = 2\delta/a$, where the periodicity length $a = (d\delta/f(\tilde{h}))^{1/2}$, see Ref. [199]. Here $d = 0.65$ mm is the sample thickness and $f(\tilde{h})$ a numerical function with $\tilde{h} = H_a/H_c$. For an applied field of typically 5 mT (Fig. 6.6), $\tilde{h} = 0.38$ and $f(\tilde{h}) = 0.022$. Consequently, $f_{DW} \approx 1.4\%$. It is not surprising that this value is considerably smaller than f_{bg} measured, because the domain patterns in our crystal will be complex, and concurrently the domain walls broad. We therefore argue that muons stopping in domain walls can largely account for the background term. Besides, muons stopping in regions where the magnetic field is pinned or trapped at defects during flux penetration or expulsion will contribute as well. Considering that the background term can be accounted for by these sources of μ^+-spin depolarization, the data do not rule out that the type-I superconducting fraction in our crystal is close to 100%.

On the other hand, the possibility that a minute fraction of the crystal exhibits type-II superconductivity cannot be completely dismissed. In a type-II superconductor the local field in the vortex phase is close to the applied field and thus its field distribution could contribute to f_{bg}. Local type-II behavior could possibly originate from a pronounced deviation of the 1:2 stoichiometry. We recall, however, that the EDX spectra show a uniform 1:2 composition within the experimental resolution of 0.5%. A mixed type-I and type-II behavior has been evoked to explain the STM/STS and PCS spectra, measured at the surface of $PdTe_2$ [180, 182]. Here it is proposed that the electron mean free path, ℓ, is locally reduced, which results in $\kappa > 1/\sqrt{2}$. We remark, evidence for flux quantization and a vortex lattice required for type-II superconductivity has not been produced. STM/STS and PCS are surface sensitive probes, and thus possibly the mixed behavior is a property of the crystal's surface only. But this in turn is difficult to reconcile with the resulting field of the vortex that has to penetrate the bulk. It is tempting to speculate that these unusual surface effects, as well as the superconductivity of the surface sheath [163], are related to the Dirac type-II character that involves topological surface states. This warrants a continuing investigation of $PdTe_2$. Superconductivity of the surface sheath [163] has been detected by magnetic susceptibility in small ac-driving fields only, and could not be probed in the present μSR experiments, which employs dc-fields. In order to obtain access to the surface properties Low Energy Muons (LEM) form an excellent tool. Here the energy of the muons can be tuned such that they localize in the surface layer of the crystal. However, at the moment this μSR technique is restricted to temperatures above 2 K only.

6.5 Summary

We have investigated the superconducting phase of $PdTe_2$ ($T_c = 1.6$ K) by transverse field muon spin rotation experiments. μSR spectra were taken on a thin disk-like crystal in two configurations: with the field perpendicular to the plane of the disk ($N_\perp = 0.87$) and with the field in the plane of the disk ($N_\parallel = 0.08$). The $H - T$ phase diagram was scanned as a function of temperature and applied field. The μSR spectra have been analysed with a three component muon depolarization function, accounting for the superconducting domains, the normal domains and a background term. In the superconducting phase normal domains are found in which the local field is always equal to B_c and larger than the applied field. This is the hall mark of the intermediate phase in a type-I superconductor. The background term is predominantly attributed to muons stopping in the superconducting-normal domain walls. In conclusion, our μSR study provides solid evidence for type-I behavior in the bulk of the $PdTe_2$ crystal.

6.6 Appendix

6.6.1 Estimate of the demagnetization factors $N_\perp$ and $N_\parallel$

The single crystal used for the μSR measurements had a disk-like shape with the c-axis perpendicular to the plane of the disk. Its thickness and diameter were 0.65 mm and 10 mm, respectively. A small piece was removed from the disk along the a-axis for other measurements. This reduced the size in the perpendicular a^*-direction to 6.8 mm and hampered the precise calculation of N. For the configuration with the field applied along the c-axis ($N_\perp$) we made two approximations. Assuming the crystal is a short cylinder with diameter 10 mm we calculate $N_\perp = 0.88$ [201]. Assuming the crystal is a rectangular bar with size

$10 \times 6.8 \times 0.65$ mm^3 we calculate $N_\perp = 0.86$ [202]. We use the average value $N_\perp = 0.87 \pm 0.02$, where the error is partly due to the uncertainty in the dimensions of the sample. Under the assumption that $N = N_\perp + 2N_\parallel = 1$, we calculate for the field in the plane of the disk $N_\parallel = 0.07$. On the other hand, the calculated value of the radial demagnetization factor of the short cylinder is $N_\parallel = 0.09$ [203]. Again, we use the average value $N_\parallel = 0.08 \pm 0.02$. We remark these values are obtained for a complete diamagnetic screening, $\chi = -1$.

6.6.2 Temperature variation of the μSR damping rate

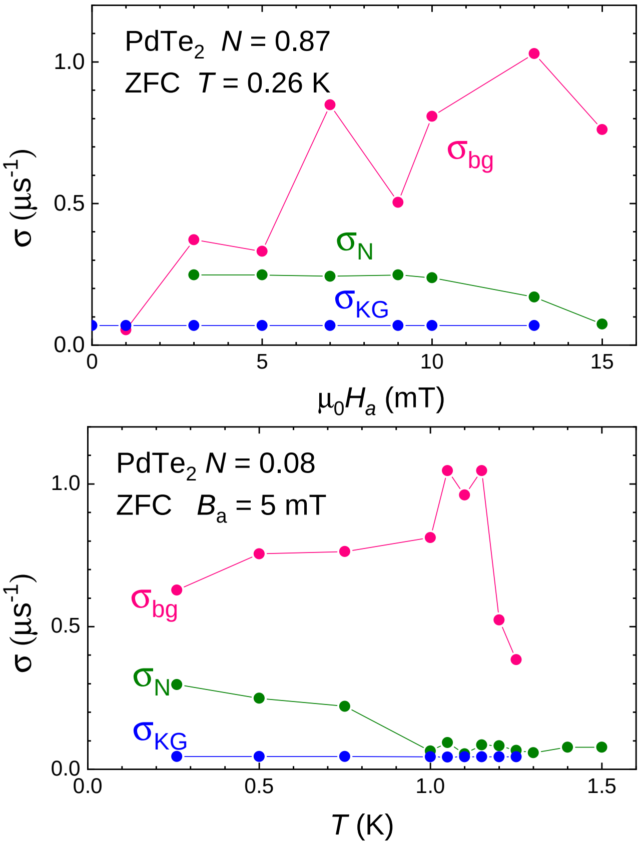

Figure 6.8: Field and temperature variation of the μSR relaxation rate for the Meissner phase, σ_{KG}, the intermediate or normal phase, σ_N, and the background contribution, σ_{bg}.

The field and temperature variations of the different relaxation rates derived from fitting the μSR spectra to Eqs. 6.1, 6.2 and 6.3 are shown in Fig. 6.8. In the upper diagram $\sigma(H)$ is traced for the configuration with the applied field perpendicular to the plane of the disk and in the lower panel $\sigma(T)$ for the field in the plane of the disk. Note the volume fraction of the background contribution is always relatively small, $\sim 10\%$.

Chapter 7

μSR study of the topological superconductor $\mathrm{Sr}_x\mathrm{Bi}_2\mathrm{Se}_3$

We report transverse-field (TF) muon spin rotation experiments on single crystals of the topological superconductor $Sr_xBi_2Se_3$ with nominal concentrations $x = 0.15$ and 0.18 ($T_c \sim 3$ K). The TF spectra ($B = 10$ mT), measured after cooling to below T_c in field, did not show any additional damping of the muon precession signal due to the flux line lattice within the experimental uncertainty. This puts a lower bound on the magnetic penetration depth $\lambda \geq 2.3$ μm. However, when we induce disorder in the vortex lattice by changing the magnetic field below T_c a sizeable damping rate is obtained for $T \rightarrow 0$. The data provide microscopic evidence for a superconducting volume fraction of ~ 70 % in the $x = 0.18$ crystal and thus bulk superconductivity.

This chapter has been published as Phys. Rev. B 97 054503 (2018).

7.1 Introduction

$Sr_xBi_2Se_3$ belongs to the new family of Bi_2Se_3-based superconductors, which is reported to exhibit unconventional superconducting properties. The parent compound Bi_2Se_3 is a well documented, archetypal topological insulator [204, 205, 206]. Recently, it was demonstrated that by doping Cu [207], Sr [208], Nb [209] or Tl [137] atoms Bi_2Se_3 can be transformed into a superconductor with $T_c \sim 3$ K. Theory predicts the superconducting state to have a topological character, which is based on the close correspondence of the Bogoliubov - de Gennes Hamiltonian for the quasiparticles of the superconductor and the Bloch Hamiltonian for the insulator (for recent reviews on topological superconductivity see Refs[210, 134]). In a topological superconductor the condensate is expected to consist of Cooper pairs with odd parity symmetry, while at the surface of the material gapless Andreev bound states form that host Majorana zero modes. This provides an excellent motivation to thoroughly examine the family of Bi_2Se_3-based superconductors. These centrosymmetric compounds (D_{3d} point group, $R\overline{3}m$ space group) belong to the symmetry class DIII [211]. Calculations within a two-orbital model show that odd-parity pairing, favoured by strong spin-orbit coupling, can be realized [212]. In the case of $Cu_xBi_2Se_3$ specific heat [213], upper critical field [172] and soft-point contact experiments [214] lend support to an odd parity superconducting state. However, scanning tunneling microscopy (STM) measurements were interpreted to be consistent with s-wave pairing symmetry [215]. Clearly, further studies are required to solve this issue.

Superconductivity in $Sr_xBi_2Se_3$ was discovered by Liu *et al.* [208]. Transport and magnetic measurements on $Sr_xBi_2Se_3$ single crystals with $x = 0.06$ show $T_c = 2.5$ K. The resistivity is metallic with a low carrier concentration $n \approx 2 \times 10^{25}$ m^{-3}. Evidence for topological surface states was extracted from Shubnikov - de Haas oscillations observed in large magnetic fields [208]. The persistence of topological surface states upon Sr doping was confirmed by angle resolved photoemisison experiments (ARPES) measurements, that showed a topological surface state well separated from the bulk conduction band [216, 217]. The superconducting state was further characterized by Shruti *et al.* [218] who reported $T_c = 2.9$ K for $x = 0.10$ and a large Ginzburg-Landau parameter, $\kappa \approx 120$, pointing to extreme type II superconducting behavior. A surprising discovery was made by Pan *et al.* [219] by performing magnetotransport measurements on crystals with nominal concentrations $x = 0.10$ and 0.15: the angular variation of the upper critical field, $B_{c2}(\theta)$, shows a pronounced *two-fold anisotropy for field directions in the basal plane*, i.e. the rotational symmetry is broken. Magnetotransport measurements under high pressures show the two-fold anisotropy is robust up to at least $p = 2.2$ GPa[220].

Most interestingly, rotational symmetry breaking appears to be a common feature of the Bi_2Se_3-based superconductors when the dopant atoms are intercalated. In $Cu_xBi_2Se_3$ it appears in the spin-system below T_c as was established by the angular variation of the Knight shift measured by nuclear magnetic resonance (NMR) [221]. Moreover, specific heat measurements show the basal-plane anisotropy in B_{c2} is a thermodynamic bulk feature [222]. In $Nb_xBi_2Se_3$ rotational symmetry breaking was demonstrated by torque magnetometry that probes the magnetization of the vortex lattice [223]. These recent experiments put important constraints on the superconducting order parameter. Notably, it restricts the order parameter to an odd-parity two-dimensional representation, E_u, with Δ_4-pairing [224, 225, 226]. Moreover, the superconducting state involves a nematic director that breaks the rotational symmetry when pinned to the crystal lattice, hence the label nematic superconductivity. The odd-parity Cooper pair state implies these Bi_2Se_3-derived superconductors are topological superconductors.

Here we report a muon spin rotation study on $Sr_xBi_2Se_3$. Muon spin rotation is an outstanding technique to determine the temperature variation of λ, as well as its absolute value, via the Gaussian damping rate, σ_{TF}, of the μ^+ precession signal in a transverse field experiment. Below T_c, an increase of σ_{TF} is expected because the muon senses the additional broadening of the field distribution due to the flux line lattice [65, 66]. The measurements show, however, that the increase of σ_{TF} is smaller than the experimental uncertainty in field-cooling experiments, which tell us λ is very large (≥ 2.3 μm for $T \to 0$). On the other hand, when we induce disorder in the vortex lattice by changing the magnetic field below T_c a sizeable damping rate $\sigma_{SC} \approx 0.36$ μs^{-1} ($T \to 0$) is obtained. These results provide microscopic evidence for a superconducting volume fraction of ~ 70 % in the crystal with nominal Sr content $x = 0.18$ and thus bulk superconductivity.

7.2 Experimental

Single crystalline samples $Sr_xBi_2Se_3$ with nominal values $x = 0.15$ and $x = 0.18$, were synthesized by melting high-purity elements at 850 °C in sealed evacuated quartz tubes. The crystals were formed by slowly cooling to 650 °C at a rate of 3 °C/hour. Powder X-ray diffraction confirmed the R$\bar{3}$m space group. The single-crystalline nature of the crystals was checked by Laue back-reflection. Thin (thickness 0.4 mm) flat rectangular crystals were cut from the single-crystalline batch by a scalpel and/or spark erosion. The sample plane contains the trigonal basal plane with the a and a^* axes. The sample area for the incident muon beam is 8×12 mm^2 and 3×10 mm^2 for $x = 0.15$ and $x = 0.18$, respectively. The characterization of the single-crystalline batch with $x = 0.15$ is presented in Ref. [219] Ac-susceptibility measurements show a superconducting shielding fraction of 80 %. For the $x = 0.18$ batch we obtain a slightly lower screening fraction, 70 %.

Muon spin rotation (μSR) experiments were carried out with the Multi Purpose Surface Muon Instrument DOLLY installed at the πE1 beamline at the SμS facility of the Paul Scherrer Institute. The technique uses spin-polarized muons that are implanted in a sample. Taking into account the density of Sr$_x$Bi$_2$Se$_3$ we calculate that muons typically penetrate over a depth of 230 μm and thus probe the bulk of the sample. If there is a local or applied field at the sample position the muon spin will precess around the field direction. The subsequent asymmetric decay process is monitored by counting the emitted positrons by scintillation detectors that are placed at opposite directions in the muon-spin precession plane [65, 66]. The parameter of interest is the muon spin asymmetry function, $A(t)$, which is determined by calculating $A(t) = (N_1(t) - \alpha N_2(t))/(N_1(t) + \alpha N_2(t))$, where $N_1(t)$ and $N_2(t)$ are the positron counts of the two opposite detectors, and α is a calibration constant. In our case α is close to 1. In the transverse field (TF) configuration the damping of the muon spin precession signal is a measure for the field distribution sensed by the muon at its localization site. For a superconductor below T_c, in a small TF of typically 10 mT, the vortex lattice is expected to produce a Gaussian damping, $\sigma_{SC} = \gamma_\mu \sqrt{\langle(\Delta B)^2\rangle}$, with $\gamma_\mu = 2\pi \times 135.5$ MHz/T the muon gyromagnetic ratio and $\langle(\Delta B)^2\rangle$ the second moment of the field distribution. TF experiments were performed for a field along the a-axis and the c-axis. In the first case the muon spin is horizontal, i.e. along the beam direction, and the positrons are collected in the forward and backward detectors. In the second case the muon spin is vertical (spin rotated mode), the field is applied along the beam, and the positrons are collected in the left and right detectors. The crystals were glued with General Electric (GE) varnish to a thin copper foil, that was attached to the cold finger of a helium-3 refrigerator (HELIOX, Oxford Instruments). μSR spectra were taken in the temperature interval $T = 0.25 - 10$ K. The μSR time spectra were analysed with the software packages WIMDA [197] and Musrfit [198].

7.3 Results and analysis

7.3.1 Field-cooled spectra

A first set of experiments was carried out for $x = 0.15$. The crystal with $T_c = 2.8$ K was slowly cooled in a TF field of 10 mT ($B \parallel a$) to $T = 0.25$ K, after which μSR spectra were recorded at fixed temperatures, during step-wise increasing the temperature up to 3.0 K. The measured spectra at 0.25 K and 3.0 K are shown Fig. 7.1, where we have plotted the decay asymmetry as a function of time. The initial asymmetry $A(0) = 0.24$ is the full experimental asymmetry (A_{tot}). As can be noticed, the spectra at 0.25 K and 3.0 K are very similar. We have fitted the spectra with the muon depolarization function

$$A(t) = A_{tot} \exp(-\frac{1}{2}\sigma_{TF}^2 t^2) \cos(2\pi\nu t + \phi). \tag{7.1}$$

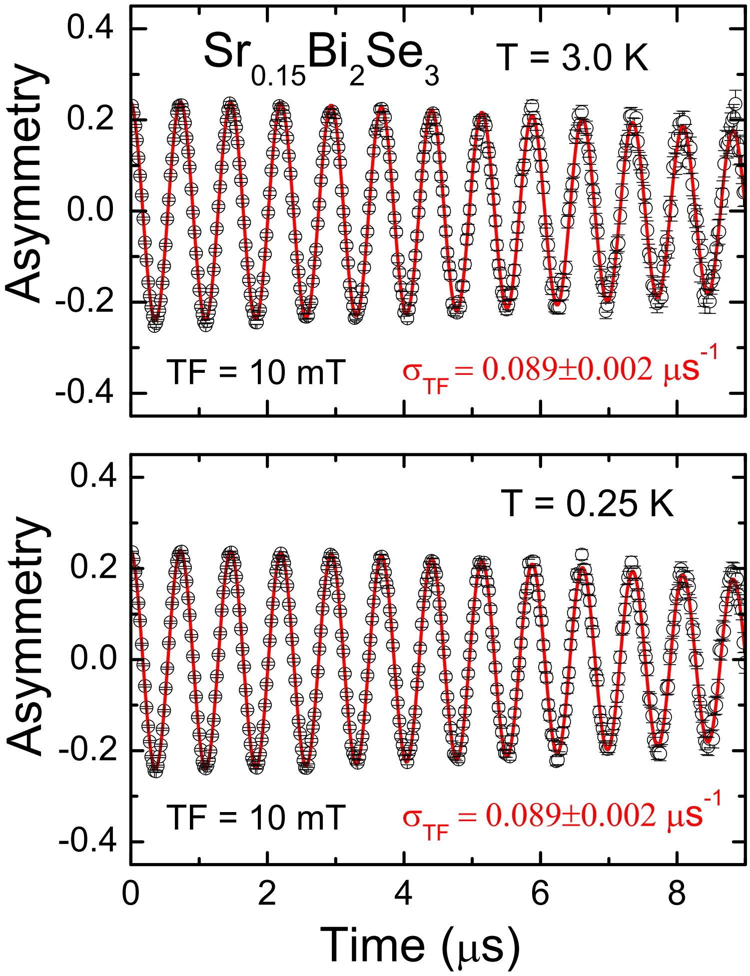

Figure 7.1: μSR spectra for $Sr_{0.15}Bi_2Se_3$ measured in a transverse field of 10 mT ($B \parallel a$) at $T = 3.0$ K (upper panel) and $T = 0.25$ K (lower panel). The red lines are fits using the muon depolarization function Eq. 1. The spectra are taken after field cooling in 10 mT.

Here σ_{TF} is the Gaussian damping rate, $\nu = \gamma_\mu B_\mu / 2\pi$ is the muon precession frequency, B_μ is the average field sensed by the muon ensemble and ϕ is a phase factor. The resulting temperature variation $\sigma_{TF}(T)$ is shown in Fig. 7.2. In the normal phase $\sigma_{TF} = 0.089 \pm 0.002$ μs^{-1}, which we attribute to the field distribution due to nuclear moments considered static within the μSR time window. No

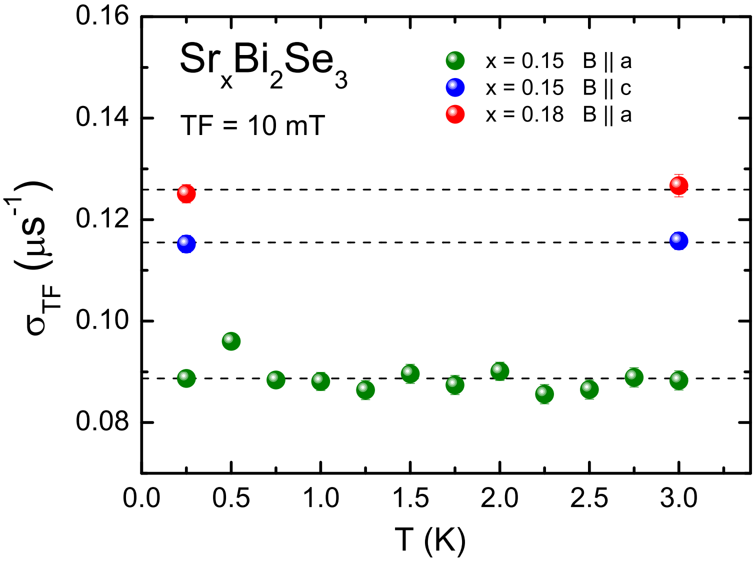

Figure 7.2: Temperature variation of the Gaussian damping rate σ_{TF} extracted with help of Eq. 1 from TF μSR spectra taken after field cooling in 10 mT. Green symbols: for $x = 0.15$ and $B \parallel a$. Blue symbols: for $x = 0.15$ and $B \parallel c$. Red symbols: for $x = 0.18$ and $B \parallel a$. The dashed horizontal lines show σ_{TF} is temperature independent.

additional damping is observed below T_c within the experimental resolution and we conclude σ_{SC} is very small. An upper bound for σ_{SC} can be derived with help of the equation [227]

$$\sigma_{SC} = (\sigma^2_{TF,T<T_c} - \sigma^2_{TF,T>T_c})^{1/2}. \tag{7.2}$$

With the experimental uncertainty in σ_{FL} of ± 0.002 μs^{-1} we obtain $\sigma_{SC} \leq 0.02$ μs^{-1}. This allows us to determine a lower bound for the London penetration depth. In the vortex state of an extreme type II superconductor with a trigonal flux line lattice λ can be estimated from the second moment of the field distribution for $B > B_{c1}$ via the relation $\langle(\Delta B)^2\rangle = 0.003706 \times \Phi_0^2/\lambda^4$, where Φ_0 is the flux quantum [228], or

$$\lambda = (0.0609\gamma_u \Phi_0/\sigma_{SC})^{1/2}. \tag{7.3}$$

With $\sigma_{SC} = 0.02$ μs^{-1} we calculate $\lambda \geq 2.3$ μm for $T \to 0$.

In the experimental configuration used to measure the data in Fig. 7.2 ($B \parallel a$) we probe the penetration depths orthogonal to the field direction, or rather the product $\lambda_c\lambda_{a^*}$. We have also carried out field-cooled (10 mT) measurements for $B \parallel c$ (muon spin rotated mode; here $A_{tot} = 0.19$) to probe the product $\lambda_a\lambda_{a^*}$. The extracted σ_{TF}-values at 0.25 K and 3.0 K are slightly larger than for $B \parallel a$, but are equal within the experimental resolution, as shown in Fig. 7.2. Finally, we have measured field-cooled μSR spectra on the $x = 0.18$ crystal for $B \parallel a$ at 0.25 K and 3.0 K. The analysis shows $\sigma_{TF} = 0.126 \pm 0.002$ μs^{-1} and, again, no significant temperature variation in σ_{TF} is observed as shown in Fig. 7.2. We conclude, for both crystals the London penetration is very large and a conservative lower bound is $\lambda = 2.3$ μm.

7.3.2 Vortex lattice with disorder

The standard procedure, used above, to extract λ from the μSR spectra for a type II superconductor relies on cooling the crystal in a small magnetic field $> B_{c1}$, which tends to produce a well ordered flux line lattice. Eq. 7.3 can then be used to calculate λ once σ_{SC} is determined [228]. It is well known that inducing disorder in the vortex lattice increases the distribution of the internal magnetic fields, and hence σ_{SC} [229, 230, 231]. In this case, λ can no longer be calculated with help of Eq. 7.3, because the calculation of λ from the field distribution has become an intricate problem [229, 230, 231]. Inducing disorder in the vortex lattice provides however an appealing route to probe the superconducting volume fraction of our crystals.

A standard procedure to induce disorder in the flux line lattice is to cool the sample to below T_c in zero field and then sweep the field to the desired TF value (ZFC mode). Examples in the literature that show a pronounced increase of σ_{SC} due to disorder can be found in Refs.[227, 232]. Here we followed a different procedure and cooled the $x = 0.18$ crystal in a strong magnetic field ($B \parallel c$) of 0.4 T to $T = 0.25$ K, after which the field was reduced to 10 mT. Decreasing the applied field causes the flux lines to move. Pinning of flux lines at crystalline defects and inhomogeneities generates magnetic disorder. We remark that for an applied field of 0.4 T the lattice parameter of the trigonal vortex lattice is $a_{\triangle} = (4/3)^{1/4}(\Phi_0/B)^{1/2} = 0.08$ μm. After decreasing the field to 10 mT $a_{\triangle} = 0.49$ μm. Next, TF=10 mT μSR spectra were taken in the temperature range 0.25 - 5 K by step-wise increasing the temperature. In Fig. 7.3 we show the data taken at 0.25 K and 3.0 K. As expected, a pronounced damping now appears in the superconducting state. We first fitted the spectrum at 0.25 K to Eq. 1, but it appeared a better fit can be made with the two-component depolarization function

$$A(t) = A_{tot}[f_{SC}\exp(-\frac{1}{2}\sigma_{SC}^2 t^2)\cos(2\pi\nu_{SC}t + \phi_{SC}) \\ + f_N \exp(-\frac{1}{2}\sigma_N^2 t^2)\cos(2\pi\nu_N t + \phi_N)]. \quad (7.4)$$

Here $f_{SC} = A_{SC}/A_{tot}$ and $f_N = A_N/A_{tot}$ are the volume fractions related to the superconducting and normal phases, respectively (ν_{SC}, ϕ_{SC} and ν_N, ϕ_N are the corresponding frequencies and phases). In the normal state $f_{SC} = 0$ and the relaxation rate σ_N equals 0.134 ± 0.002 μs^{-1}. This value is close to the one reported in Fig. 7.2. The result of the two-component fit of the spectrum at 0.25 K is shown in Fig. 7.3. Here the total asymmetry $A_{tot} = A_{SC} + A_N$ is fixed at the experimental value $A(0) = 0.19$ (spin-rotated mode) and σ_N is fixed at 0.134 μs^{-1}. We obtain $f_{SC} = 0.71$, $f_N = 0.29$ and $\sigma_{SC} = 0.36 \pm 0.02$ μs^{-1}. It shows that for this crystal the superconducting volume fraction amounts to 70 %, in good agreement with ac-susceptibility measurements, see Fig. 7.4(c). In Fig. 7.4 we show the temperature variation of the fit parameters f_{SC}, f_N and σ_{SC}. The smooth variation of f_{SC} to zero indicates $T_c = 2.5$ K, which is slightly below the onset temperature for superconductivity $T_c = 2.7$ K determined by ac-susceptibility on a piece of the same single-crystalline batch.

The values of σ_{SC} in Fig. 7.4 indicate considerable disorder in the flux line lattice. In a second run we have field-cooled the sample in 10 mT to 0.25 K, next reduced the field to zero and subsequently increased it to 14.5 mT. TF field spectra ($B \parallel a$) taken after this field history showed $\sigma_{TF} = 0.20$ μs^{-1} at 0.25 K, which indicates a much weaker degree of disorder in the vortex lattice. The temperature variation of the fit parameters σ_{SC}, f_{SC} and f_N obtained by using Eq. 7.4 for this second run are shown in Fig. 7.4.

The fitting procedure with a two-component muon depolarization function (Eq. 7.4) is a standard and frequently used method to determine the superconducting volume fraction. Another method is to directly compare the frequencies in the normal and superconducting phases and the corresponding amplitudes of the Fast Fourier Transform (FFT). Frequency shifts of the asymmetry spectra for our data are reported in the Appendix. Clear frequency shifts are detected in the superconducting phase. However, the shifts are small (< 1.1 %) and the FFTs of the asymmetry spectra relatively broad. This hampers the determination of the superconducting volume fraction from the FFTs.

7.4 Discussion

An important conclusion that can be drawn from the TF μSR spectra taken in the disordered vortex lattice case is that Sr$_x$Bi$_2$Se$_3$ for $x = 0.18$ is a bulk superconductor. We remark that specific heat experiments around T_c, which provide a thermodynamic way to demonstrate bulk superconductivity, have not been reported in the literature so far. The superconducting volume fraction of 70 % obtained by μSR nicely agrees with the superconducting screening fraction determined by ac-susceptibility measurements.

In the field-cooled case (ordered vortex lattice) we could not detect the damping

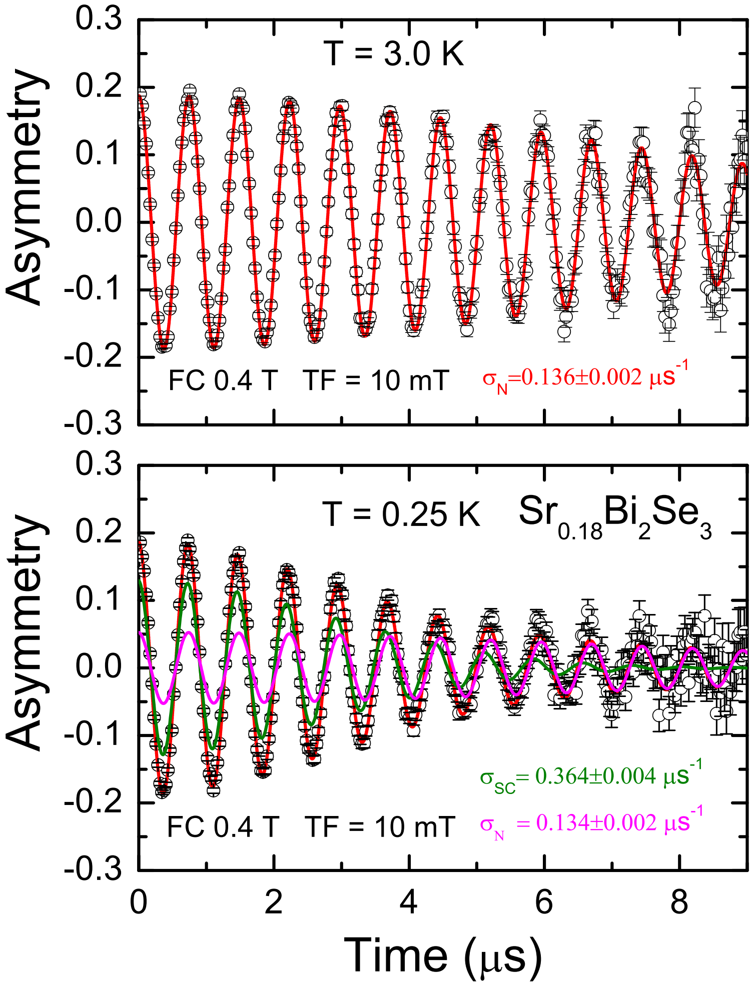

Figure 7.3: μSR spectra for $Sr_{0.18}Bi_2Se_3$ measured in a transverse field of 10 mT at $T = 3.0$ K (upper panel) and $T = 0.25$ K (lower panel). The crystal was cooled in a strong field of 0.4 T ($B \parallel c$), after which the field was reduced to 10 mT. The red lines are fits to the muon depolarization function Eq. 4. The green and magenta lines in the lower panel represent the contributions to the μSR signal from the superconducting and normal state volume fractions, respectively.

of the μ^+ precession signal due to superconductivity. This puts a lower bound on the penetration depth λ of 2.3 μm. Within the London model λ is related to the superfluid density n_s via the relation

$$\lambda = (\frac{m^*}{\mu_0 n_s e^2})^{1/2}, \tag{7.5}$$

where m^* is the effective mass of the charge carriers, μ_0 is the permeability of the

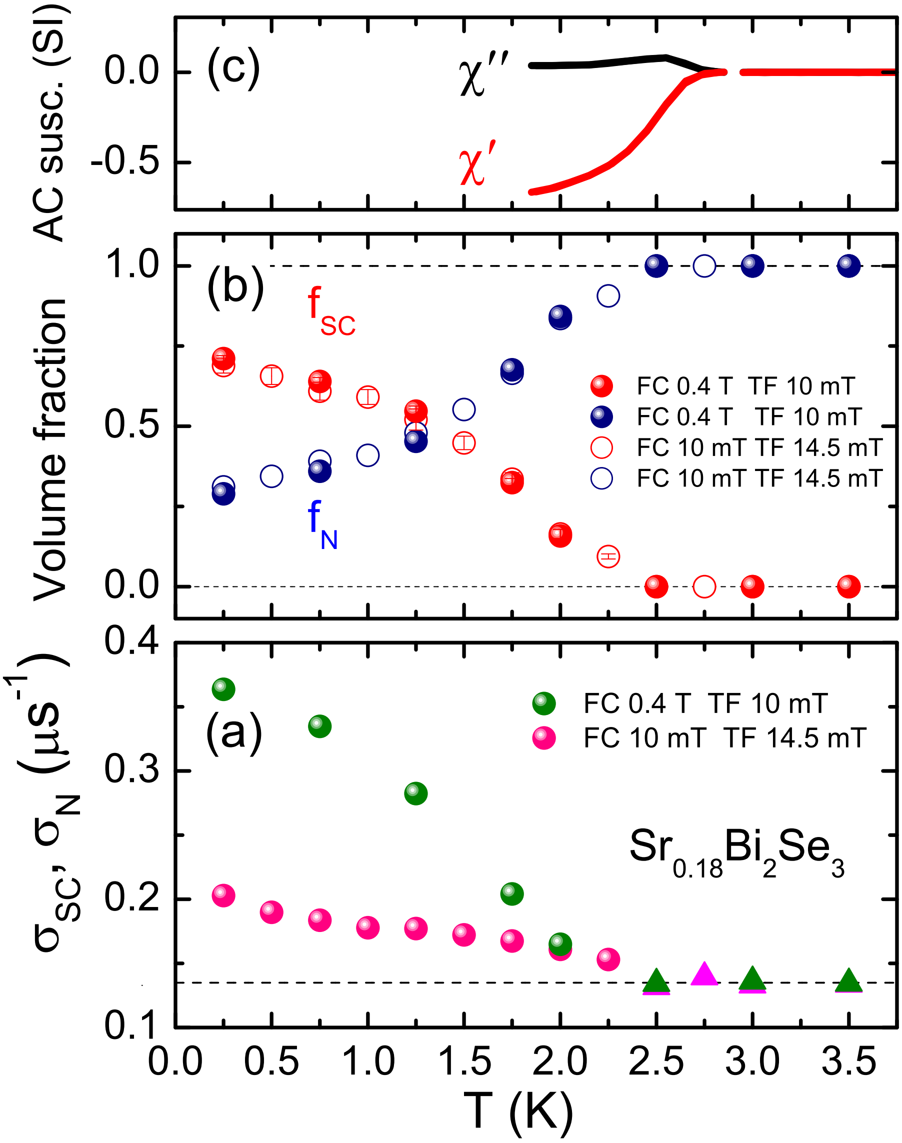

Figure 7.4: Fit parameters of the two-component analysis (Eq. 4) of TF μSR spectra for $Sr_{0.18}Bi_2Se_3$. Disorder in the vortex lattice is induced by changing the field below T_c. Panel (a): $\sigma_{SC}(T)$ (round symbols) and $\sigma_N(T)$ (triangles). Green symbols: field-cooling in 0.4 T, spectra measured after reducing the field to TF = 10 mT ($B \parallel c$). Magenta symbols: cooling in 10 mT, spectra measured after sweeping the field first to zero and then up to TF= 14.5 mT ($B \parallel a$). Panel (b): Superconducting f_{SC} and normal-state f_N volume fraction for cooling in 0.4 T (closed symbols) and 10 mT (open symbols). Panel (c): AC susceptibility in S.I. units. The superconducting screening fraction is 0.7.

vacuum and e the elementary charge. Assuming $m^* = m_e$, $\lambda = 2.3$ μm translates to an extremely small value $n_s \sim 0.05 \times 10^{26}$ m^{-3}. This is difficult to reconcile with the carrier density $n = 1.2 \times 10^{26}$ m^{-3} we measured by the Hall effect on a crystal from the same batch at 4.2 K. In the literature, however, significant lower values for n have been reported: 0.27×10^{26} m^{-3} (Ref. [208]) and 0.19×10^{26} m^{-3} (Ref.[218]), which results in λ-values of 1.0 μm and 1.2 μm, respectively, using Eq. 5. A possible solution is that $m^* > m_e$, but this is not in accordance with quantum oscillation studies. For low-carrier density samples of Bi_2Se_3 Shubnikov - de Haas data ($B \parallel c$) show $m^* = 0.124m_e$ [233]. Doping may result in a slightly larger value of m^*. For instance for Cu-doped Bi_2Se_3 $m^* = 0.2$-$0.3m_e$ [234]. On the other hand, from specific heat experiments on Cu-doped Bi_2Se_3 a quasiparticle mass of $2.6m_e$ has been deduced [213]. Values for the effective mass of $Sr_xBi_2Se_3$ have not been reported so far.

Very recently TF field muon spin rotation experiments on $Cu_xBi_2Se_3$ crystals have been reported for a field of 10 mT applied along the c-axis [235]. Interestingly, the authors do find a small increase of σ_{TF} below T_c. In the normal state $\sigma_{TF} = 0.105 \pm 0.001$ μs^{-1}, a value comparable to the ones for the Sr doped case reported in Fig. 7.2. In the superconducting phase a small but clear increase of σ_{TF} is observed to a value of 0.113 ± 0.001 μs^{-1} for $T \to 0$. By analyzing the data with help of Eq. 7.2 the authors calculate $\sigma_{SC} = 0.04$ μs^{-1} and $\lambda = 1.6$ μm. We remark the total increase in σ_{TF} below T_c is only 0.008 μs^{-1}, which is only slightly larger than the scatter in our values of σ_{TF} (see Fig. 7.2). The higher precision in these experiments is partly due to very long counting times resulting in better statistics. The μSR experiments on Cu and Sr doped Bi_2Se_3 agree in the sense that for both materials λ is very large. Note that for $Cu_xBi_2Se_3$ we calculate, with Eq. 5, using $\lambda = 1.6$ μm and assuming $m^* = m_e$ a superfluid density $n_s = 0.11 \times 10^{26}$ m^{-3}, which is also at variance with the measured carrier concentration [213, 234] (n_s is a factor 10 smaller). The recurring result that $n_s \ll n$ seems to indicate that only part of the conduction electrons participate in the superconducting condensate. A possible explanation is substantial electronic phase inhomogeneities, where the superconducting phase (volume fraction 70 % for $Sr_{0.18}Bi_2Se_3$ and 40-60 % for $Cu_xBi_2Se_3$ [213, 235]) has effectively a lower carrier concentration than the normal phase. On the other hand, a similar mismatch between n_s and n has recently been reported for the Nb doped low-carrier density superconductor $SrTiO_3$ notably in the over-doped, dirty regime, which is relevant in the context of high-T$_c$ cuprates as well [236]. We remark that the discrepancy between n_s and n does not show up in the standard analysis of the Ginzburg-Landau parameter $\kappa = \lambda/\xi$, where ξ is the superconducting coherence length. The large value of $\kappa \sim 100$ and the small coherence length $\xi \sim 15$ nm extracted from transport and magnetic measurements [218, 213] result in a substantial value

$\lambda \sim 1.5$ μm. Here we have neglected for the purpose of simplicity the crystalline anisotropy of about a factor 1.5 in these parameters.

The μSR spectra for the $x = 0.18$ crystal, taken after cooling in 0.4 T and subsequently reducing the field to 10 mT, show a sizeable depolarization due to disorder in the vortex lattice. If we assume a random distribution of flux lines, λ can be calculated using the expression $\langle(\Delta B)^2\rangle = \Phi_0 B/4\pi\lambda^2$ (see Refs [230, 231]). With $\sigma_{SC} = 0.36$ μs^{-1} (see Fig. 7.4(a)) we calculate $\lambda = 3.0$ μm, a value in line with the lower bound 2.3 μm estimated from the field-cooled experiments. It is not surprising substantial disorder in the vortex lattice can be created. In the Cu, Sr and Nb case experimental evidence has been presented that the dopant atoms are intercalated in the Van der Waals gaps between the quintuple layers of the Bi$_2$Se$_3$ structure [207, 208, 209]. However, partial substitution on the Bi lattice cannot be ruled out. A detailed refinement of the crystal structure after intercalation has not been reported for these compounds so far. For Cu$_x$Bi$_2$Se$_3$ it has been inferred by analogy to related selenides that the intercalant atoms reside in the 3*b* site (Wyckoff notation) [207]. Moreover, structural investigations report considerable disorder on various length scales [237, 238]. Thus the Bi-based superconductors are prone to various types of structural disorder, which in turn may provide different sources of flux pinning.

7.5 Summary and conclusions

We have performed transverse field muon spin rotation experiments on single-crystalline samples of Sr$_x$Bi$_2$Se$_3$ with the aim to determine the London penetration depth, λ. Field-cooled μSR spectra measured for the ordered flux line lattice reveal however no additional damping of the μ^+ precession signal in the superconducting phase. From the data we infer a lower bound for λ of 2.3 μm. By changing the applied magnetic field in the superconducting phase we are able to induce disorder in the vortex lattice. This results in a sizeable value $\sigma_{SC} = 0.36$ μs^{-1} for $T \to 0$. By analyzing the μSR time spectra with a two component function we obtain a superconducting volume fraction of 70 %. This provides solid evidence for bulk superconductivity in Sr$_x$Bi$_2$Se$_3$. We signal a discrepancy between the superfluid density, n_s, calculated from λ within the London model, and the measured carrier concentration. Finally, we recall that the reported [219, 221, 222, 223] breaking of rotational symmetry in the small family of Bi$_2$Se$_3$-based superconductors deserves a close examination, notably because it offers an excellent opportunity to study unconventional superconductivity with a two-component order parameter.

7.6 Appendix

7.6.1 Frequency shift in the superconducting state

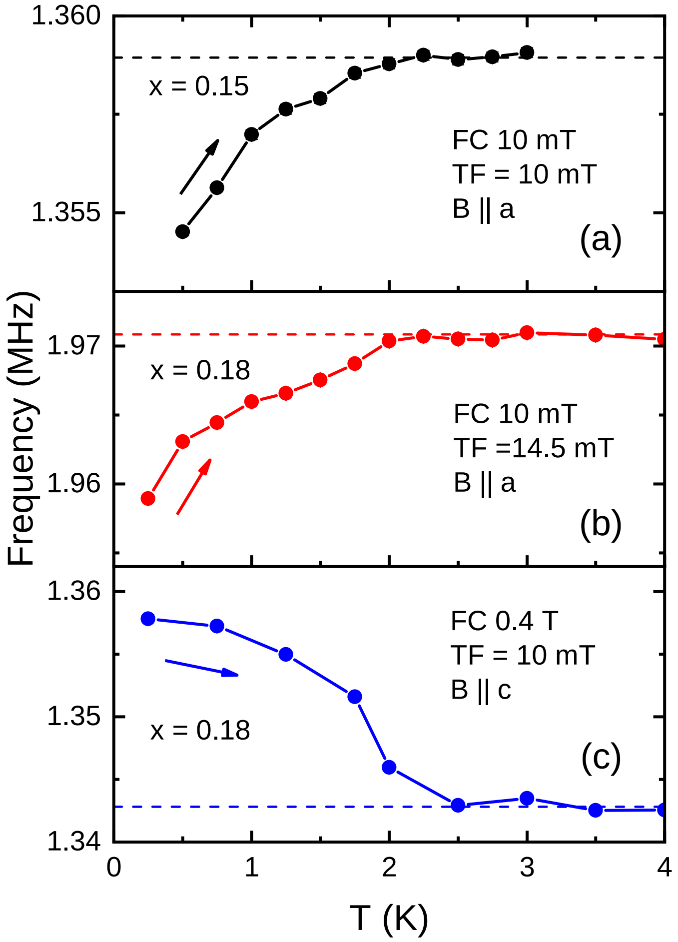

Figure 7.5: Observed frequency shifts in the superconducting phase of the asymmetry signal of $Sr_xBi_2Se_3$ crystals obtained by fitting the spectra to a one-component muon depolarization (see above). The arrows indicate the data are taken with increasing temperature.

Fitting the asymmetry spectra to the one- or two-component muon depolarization functions (shown in Eqs. 7.1 and 7.4) as presented in section 1.3 is a standard and frequently used method to determine the damping due to the vortex lattice and the superconducting volume fraction. Another way is to directly compare the frequencies in the normal and superconducting state and the corresponding amplitudes of the Fast Fourier Transform (FFT). However, since the frequency shifts are small (< 1.1 %) and the FFTs of the asymmetry spectra relatively broad we cannot resolve the frequencies for the superconducting and normal phase. Nonetheless, a clear frequency shift is detected as reported in Fig. 7.5. Here we have fitted the asymmetry spectra $A(t)$ to the one-component depolarization function (Eq. 7.1)

$$A(t) = A_{tot} \exp(-\frac{1}{2}\sigma_{TF}^2 t^2) \cos(2\pi\nu t + \phi), \tag{7.6}$$

where A_{tot} is the experimental asymmetry, σ_{TF} is the Gaussian damping rate, $\nu = \gamma_\mu B_\mu / 2\pi$ is the muon precession frequency, B_μ is the average field sensed by the muon ensemble and ϕ is a phase factor. For the ordered vortex lattice ($x = 0.15$; FC 10 mT; $B \parallel a$) we observe a small diamagnetic shift of the order of -0.3 % (panel a). For the disorder vortex lattice the total shift amounts to -0.6 % ($x = 0.18$; FC 10 mT; TF = 14.5 mT; $B \parallel a$; panel b) and 1.1 % ($x = 0.18$, FC 0.4 T; TF = 10 mT, $B \parallel c$, panel c). Note the sign of the shift relates to the field history: negative for FC 10 mT (panel a) and for FC 10 mT → 0 mT → 14.5 mT (panel b), and positive for FC 0.4 T → 10 mT (panel c). The latter shift is positive, because the field is reduced from a large positive value and thus the data are taken in the positive quadrant of the $M(H)$ hysteresis loop.

Summary

Topological quantum materials have sparked great interest to pursue electronically nontrivial phases. It is expected this new trend will keep on producing more exotic discoveries about novel quantum phases of topological matter. Regarding topological superconductors the physics of dispersive Majorana fermions on the surface is a new field of research, and also it is important for future applications in quantum computation. Investigating new types of topological phenomena in real materials is significant for both developing new devices and verifying theoretical models and predictions. Intrinsic topological superconductors are rare in nature, several concrete cases have been investigated extensively, such as Sr_2RuO_4, $Cu_xBi_2Se_3$, $Sn_{1-x}In_xTe$ and several noncentrosymmetric superconductors. The presence of Weyl and Dirac semimetals as a 3D analog of graphene shed further light on topological superconductors with their characteristic electronic properties, for instance protected Fermi surface states and a novel response to applied electric and magnetic fields. In this thesis we presented the experimental results on the type II Dirac semimetal $PdTe_2$ (Chapter 4-6) and the topological superconductor candidate $Sr_xBi_2Se_3$ (Chapter 7).

The first chapter may be read as a rather general introduction to topological materials, special attention was paid to TSCs and two candidates of TSCs $PdTe_2$ and $Sr_xBi_2Se_3$. In the second chapter we described the preparation and characterization of the samples, and the experimental techniques used in this thesis project. Chapter 3 dealt with the theoretical aspects relevant for this thesis project.

In Chapter 4, we discussed the superconducting properties of $PdTe_2$ investigated by dc-magnetization, ac-susceptibility and transport measurements. Our crystals clearly show type I superconductivity as demonstrated by the observation of the intermediate state probed by the differential paramagnetic effect measured by in the ac-susceptibility. In addition, superconductivity of the surface layer is found below $T_c^s = 1.33$ K $< T_c$. It persists up to $\mu_0 H_c^s(0) = 34.9$ mT and does not follow the standard Saint-James-de Gennes behavior. Resistance data point to an even larger critical field for the surface layer $H_c^R(0) \approx 0.30$ T. $PdTe_2$ is the only topological material for which type I superconductivity has been reported so far. This, together with the unusual superconducting phase diagram, calls for a close examination of superconductivity in $\mathrm{PdTe_2}$, especially in view of the existence of topological surface states.

In Chapter 5 we focused on a high-pressure transport and ac-susceptibility study of superconductivity in the type-I superconductor $\mathrm{PdTe_2}$ ($T_c = 1.64$ K). T_c shows a pronounced variation with pressure: it increases at low pressure, then passes through a maximum of 1.91 K around 0.91 GPa, and subsequently decreases smoothly up to the highest pressure measured, $p_{max} = 2.5$ GPa. Type-I superconductivity is robust under pressure. The unusual surface superconductivity persists under pressure. Surprisingly, for $p \geq 1.41$ GPa the superconducting transition temperature for the surface T_c^S exceeds T_c of the bulk. This tells us surface and bulk superconductivity are distinct phenomena. We propose surface superconductivity possibly has a non-trivial nature and originates from topological non trivial surface states. This calls for quantum-oscillation experiments under pressure. In the same spirit it will be highly interesting to extend the experiments to higher pressures, especially because a pronounced change in the electronic properties of $\mathrm{PdTe_2}$ is predicted to occur in the range 4.7-6.1 GPa: the type-II Dirac points disappear at 6.1 GPa, and a new pair of type-I Dirac points emerges at 4.7 GPa. Thus a topological phase transition may occur in the pressure range 4.7-6.1 GPa. This in turn might have a strong effect on (surface) superconductivity, because the tilt parameter of the Dirac cones passes the critical value of 1. We conclude further high-pressure experiments on $\mathrm{PdTe_2}$ provide a unique opportunity to investigate the connection between topological quantum states and superconductivity.

In Chapter 6 we have investigated the superconducting phase of $\mathrm{PdTe_2}$ ($T_c =$ 1.6 K) by transverse field muon spin rotation experiments. μSR spectra were taken on a thin disk-like crystal in two configurations: with the field perpendicular to the plane of the disk ($N_\perp = 0.87$) and with the field in the plane of the disk ($N_\parallel = 0.08$). The $H-T$ phase diagram was scanned as a function of temperature and applied field. The μSR spectra have been analysed with a three component muon depolarization function, accounting for the superconducting domains, the normal domains and a background term. In the superconducting phase normal domains are found in which the local field is always equal to B_c and larger than the applied field. This is the hall mark of the intermediate phase in a type-I superconductor. The background term is predominantly attributed to muons stopping in the superconducting-normal domain walls. In conclusion, our μSR study provides solid evidence for type-I behavior in the bulk of the $\mathrm{PdTe_2}$ crystal.

In Chapter 7 we have performed transverse field muon spin rotation experiments on single-crystalline samples of $\mathrm{Sr}_x\mathrm{Bi_2Se_3}$ with the aim to determine the magnetic penetration depth, λ. Field-cooled μSR spectra measured for the ordered flux line lattice reveal however no additional damping of the μ^+ precession signal in the superconducting phase. From the data we infer a lower bound for λ

of 2.3 μm. By changing the applied magnetic field in the superconducting phase we are able to induce disorder in the vortex lattice. This results in a sizeable value $\sigma_{SC} = 0.36$ μs^{-1} for $T \to 0$. By analyzing the μSR time spectra with a two component function we obtain a superconducting volume fraction of 70 %. This provides solid evidence for bulk superconductivity in Sr$_x$Bi$_2$Se$_3$. We signal a discrepancy between the superfluid density, n_s, calculated from λ within the London model, and the measured carrier concentration. Finally, we recall that the reported breaking of rotational symmetry in the small family of Bi$_2$Se$_3$-based superconductors deserves a close examination, notably because it offers an excellent opportunity to study unconventional superconductivity with a two-component order parameter.

Samenvatting

Topologische quantummaterialen hebben grote belangstelling gegenereerd voor de zoektocht naar elektronische niet-triviale fasen. Naar verwachting zullen er dankzij deze ontwikkeling meer exotische ontdekkingen gedaan worden rondom nieuwe quantumfases in topologische materie. Bij topologische supergeleiders leidde dit tot dispersieve Majorana fermionen op het oppervlak als nieuw onderzoeksveld, wat als belangrijk element fungeert voor toekomstige toepassingen in quantumcomputers. Onderzoek naar nieuwe topologische fenomenen in echte materialen is cruciaal voor zowel de ontwikkeling van nieuwe apparaten als het verifiëren van theoretische modellen. Intrinsiek topologische materialen zijn zeldzaam. Diverse concrete kandidaten zijn uitgebreid onderzocht, zoals $\mathrm{Sr_2RuO_4}$, $\mathrm{Cu}_x\mathrm{Bi_2Se_3}$, $\mathrm{Sn}_{1-x}\mathrm{In}_x\mathrm{Te}$ en verschillende niet-centrosymmetrische supergeleiders. Het voorkomen van Weyl en Dirac semimetalen als 3D analoog van grafeen bracht meer verheldering over karakteristieke electronische eigenschappen van topologische supergeleiders, bijvoorbeeld beschermde Fermi-oppervlaktetoestanden en bijzondere responses op aangelegde elektrische en magnetische velden. In dit proefschrift werden de experimentele resultaten van het type II Dirac semimetal $\mathrm{PdTe_2}$ (Hoofdstuk 4-6) en de kandidaat topologische supergeleider $\mathrm{Sr}_x\mathrm{Bi_2Se_3}$ (Hoofdstuk 7) gepresenteerd.

Het eerste hoofdstuk diende als algemene inleiding op topologische materialen, met speciale aandacht voor topologische supergeleiders en de desbetreffende kandidaten $\mathrm{PdTe_2}$ en $\mathrm{Sr}_x\mathrm{Bi_2Se_3}$. In het tweede hoofdstuk werden de bereiding en karakterisering van de preparaten, alsmede de gebruikte experimentele technieken, beschreven. Het derde hoofdstuk richtte zich op theoretische aspecten die relevant zijn voor dit promotieonderzoek. In hoofdstuk 4 werden de supergeleidende eigenschappen van $\mathrm{PdTe_2}$ besproken die onderzocht waren door middel van dc-magnetizatie, ac-susceptibiliteit en transportmetingen. De aanwezigheid van type I supergeleiding in onze kristallen is onherroeplijk aangetoond door het observeren van de intermediaire toestand door middel van het differentieële paramagnetische effect gemeten met ac-susceptibiliteit. Bovendien is supergeleiding in de oppervlaktelaag gevonden beneden $T_c^S = 1.33$ K $< T_c$, wat aanhoudt tot $\mu_0 H_c^S(0) = 34.9$ mT, en dat niet het conventionele Saint-James-de Gennes gedrag vertoont. Weerstandsdata suggereren een hoger kritisch veld voor de oppervlaktelaag $H_c^R(0) \approx 0.30$ T. Tot nu toe is PdTe$_2$ het enige topologisch materiaal waar voor type I supergeleiding gerapporteerd is. Dit, in combinatie met het ongewone supergeleidende fasediagram, vraagt om nauwgezet vervolgonderzoek naar supergeleiding in PdTe$_2$, zeker gezien de aanwezigheid van topologische oppervlaktetoestanden.

Hoofdstuk 5 was gericht op een hoge-druk transport en ac-susceptibiliteit studie van de type I supergeleider PdTe$_2$ ($T_c = 1.64$ K). T_c vertoont een opmerkelijke variatie met druk: een toename bij lage druk tot een maximum van 1.91 K rond 0.91 GPa, gevolgd door een gelijdelijke afname tot de hoogst gemeten drukwaarde van 2.5 GPa. Type I supergeleiding is robuust onder druk. De buitengewone oppervlaktesupergeleiding blijft eveneens bestaan onder druk. Voor $p \geq 1.41$ GPa overschrijdt de overgangstemperatuur van de oppervlaktesupergeleiding T_c^S die van de bulk verbazingwekkend genoeg. Dit geeft aan dat oppervlakte en bulk supergeleiding aparte fenomenen zijn. Dit leidt tot de veronderstelling dat oppervlaktesupergeleiding mogelijk een niet-triviale aard heeft en afkomstig is van topologische niet-triviale oppervlaktetoestanden. Ter verifiëring zouden er quantumoscillatie experimenten onder druk kunnen worden verricht. In dezelfde geest zou een extensie naar hogere drukken zeer interessant zijn met het oog op de voorspelde geprononceerde verandering in de elektronische eigenschappen van PdTe$_2$ rond 4.7-6.1 GPa: type II Dirac punten verdwijnen rond 6.1 GPa en type I Dirac punten onstaan bij 4.7 GPa, suggererende dat er een topologische faseovergang zou kunnen plaatsvinden in het drukgebied 4.7 tot 6.1 GPa. Dit kan mogelijkerwijs een sterk effect hebben op de (oppervlakte)supergeleidbaarheid, aangezien de kantelparameter van de Dirac kegels de kritische waarde van 1 overschrijdt. Verder concluderen wij dat hoge-druk experimenten op PdTe$_2$ een unieke mogelijkheid bieden om de connectie tussen topologische quantumtoestanden en supergeleideing te onderzoeken.

In hoodfstuk 6 werden de onderzoeksresultaten van de supergeleidende fase van PdTe$_2$ ($T_c = 1.6$ K) weergegeven onderzocht door middel van transvers veld muon spin rotatie experimenten. μSR spectra zijn verkregen op een dun schijfachtig kristal in twee configuraties: met het veld loodrecht op het schijfvlak ($N_\perp = 0.87$) en met het veld in het schijfvlak ($\mathrm{N}_\parallel = 0.08$). Het $H - T$ fasediagram is gescand als functie van temperatuur en veld. De μSR spectra zijn geanalyseerd met een drie-componenten muon depolarisatiefunctie, rekening houdend met de supergeleidende domeinen, de normale domeinen en een achtergrondterm. In het supergeleidende fasediagram zijn er domeinen gevonden waarin het lokale veld altijd gelijk is aan B_c, alsmede groter dan het aangelegde veld, hetgeen kenmerkend is voor de intermediaire fase van een type I supergeleider. De achtergrondterm wordt hoofdzakelijk toegeschreven aan de muonen die precesseren in de supergeleidende domeinwanden. Ter conclusie, deze μSR studie levert een solide bewijs voor type

I supergeleiding in de bulk van $PdTe_2$.
In hoofstuk 7 werden de resultaten van transvers veld muon spin rotatie experimenten op één-kristallijne preparaten van $Sr_xBi_2Se_3$ gepresenteerd, met als doel de magnetische indringdiepte λ te bepalen. De veld-gekoelde μSR spectra gemeten voor het geordende fluxlijnrooster onthullen daarentegen geen additionele demping van het μ^+ precessiesignaal in de supergeleidende fase. Een ondergrens voor λ van 2.3 μm is afgeleid uit de data. Door het aangelegde magnetische veld te variëren is het mogelijk om wanorde in het vortexrooster te realiseren. Dit resulteert in een opmerkelijke waarde $\sigma_{SC} = 0.36$ μs^{-1} voor $T \to 0$. Een supergeleidende volumefractie van 70 % is bepaald door de μSR tijdsspectra te analyseren met een twee-componenten functie. Dit biedt solide bewijs voor de aanwezigheid van bulk supergeleiding in $Sr_xBi_2Se_3$. Wel is er een discrepantie tussen de supervloeistof dichtheid, n_s, berekend vanuit λ met het London model, en de gemeten ladingdragersconcentratie. Ten slotte werd er opgemerkt dat de gerapporteerde rotationele symmetriebreking in de kleine familie van Bi_2Se_3 gebaseerde supergeleiders nauwgezette aandacht verdient, in het bijzonder omdat dit een uitstekende mogelijkheid biedt om onconventionele supergeleding met een twee-componenten orde parameter te bestuderen.

Bibliography

[1] M. Sato and Y. Ando *Rep. Prog.*, vol. 80, p. 076501, 2017.

[2] Z. Liu, B. Zhou, Y. Zhang, Z. Wang, H. Weng, D. Prabhakaran, S.-K. Mo, Z. Shen, Z. Fang, X. Dai, *et al. Science*, vol. 343, p. 864, 2014.

[3] B. Yan and C. Felser *Annu. Rev. Condens. Matter. Phys.*, vol. 8, p. 337, 2017.

[4] D. J. Thouless, M. Kohmoto, M. P. Nightingale, and M. den Nijs *Phys. Rev. Lett.*, vol. 49, p. 405, 1982.

[5] C. L. Kane and E. J. Mele *Phys. Rev. Lett.*, vol. 95, p. 226801, 2005.

[6] J. E. Moore and L. Balents *Phys. Rev. B*, vol. 75, p. 121306, 2007.

[7] Z.-C. Gu and X.-G. Wen *Phys. Rev. B*, vol. 80, p. 155131, 2009.

[8] B. A. Bernevig, T. L. Hughes, and S.-C. Zhang *Science*, vol. 314, p. 1757, 2006.

[9] H. Zhang, C.-X. Liu, X.-L. Qi, X. Dai, Z. Fang, and S.-C. Zhang *Nat. Phys.*, vol. 5, p. 438, 2009.

[10] Y. Chen, J. G. Analytis, J.-H. Chu, Z. Liu, S.-K. Mo, X.-L. Qi, H. Zhang, D. Lu, X. Dai, Z. Fang, *et al. Science*, vol. 325, p. 178, 2009.

[11] D. Hsieh, D. Qian, L. Wray, Y. Xia, Y. S. Hor, R. J. Cava, and M. Z. Hasan *Nature*, vol. 452, p. 970, 2008.

[12] L. Fu and C. L. Kane *Phys. Rev. B*, vol. 76, p. 045302, 2007.

[13] L. Yang, Z. Liu, Y. Sun, H. Peng, H. Yang, T. Zhang, B. Zhou, Y. Zhang, Y. Guo, M. Rahn, *et al. Nat. Phys.*, vol. 11, p. 728, 2015.

[14] S.-Y. Xu, I. Belopolski, N. Alidoust, M. Neupane, G. Bian, C. Zhang, R. Sankar, G. Chang, Z. Yuan, C.-C. Lee, *et al. Science*, vol. 349, p. 613, 2015.

[15] Y. Ando and L. Fu *Annu. Rev. Condens. Matter Phys.*, vol. 6, p. 361, 2015.

[16] S. Kashiwaya, H. Kashiwaya, H. Kambara, T. Furuta, H. Yaguchi, Y. Tanaka, and Y. Maeno *Phys. Rev. Lett.*, vol. 107, p. 077003, 2011.

[17] Y. Maeno, S. Kittaka, T. Nomura, S. Yonezawa, and K. Ishida *J. Phys. Soc. Jpn*, vol. 81, p. 011009, 2011.

[18] A. Pustogow, Y. Luo, A. Chronister, Y.-S. Su, D. Sokolov, F. Jerzembeck, A. P. Mackenzie, C. Hicks, N. Kikugawa, S. Raghu, *et al. Nature*, vol. 574, p. 72, 2019.

[19] L. Maier, J. B. Oostinga, D. Knott, C. Brüne, P. Virtanen, G. Tkachov, E. M. Hankiewicz, C. Gould, H. Buhmann, and L. W. Molenkamp *Phys. Rev. Lett.*, vol. 109, p. 186806, 2012.

[20] R. S. Deacon, J. Wiedenmann, E. Bocquillon, F. Domínguez, T. M. Klapwijk, P. Leubner, C. Brüne, E. M. Hankiewicz, S. Tarucha, K. Ishibashi, *et al. Phys. Rev. X*, vol. 7, p. 021011, 2017.

[21] F. Yang, F. Qu, J. Shen, Y. Ding, J. Chen, Z. Ji, G. Liu, J. Fan, C. Yang, L. Fu, *et al. Phys. Rev. B*, vol. 86, p. 134504, 2012.

[22] K. Matano, M. Kriener, K. Segawa, Y. Ando, and G.-q. Zheng *Nat. Phys.*, vol. 12, p. 852, 2016.

[23] T. Bay, T. Naka, Y. Huang, H. Luigjes, M. Golden, and A. De Visser *Phys. Rev. Lett.*, vol. 108, p. 057001, 2012.

[24] Y. Pan, A. Nikitin, G. Araizi, Y. Huang, Y. Matsushita, T. Naka, and A. De Visser *Sci. Rep.*, vol. 6, p. 28632, 2016.

[25] Y. S. Hor, A. J. Williams, J. G. Checkelsky, P. Roushan, J. Seo, Q. Xu, H. W. Zandbergen, A. Yazdani, N. P. Ong, and R. J. Cava *Phys. Rev. Lett.*, vol. 104, p. 057001, 2010.

[26] A. Nikitin, Y. Pan, Y. Huang, T. Naka, and A. de Visser *Phys. Rev. B*, vol. 94, p. 144516, 2016.

[27] S. Sasaki, Z. Ren, A. Taskin, K. Segawa, L. Fu, and Y. Ando *Phys. Rev. Lett.*, vol. 109, p. 217004, 2012.

[28] G. Goll, M. Marz, A. Hamann, T. Tomanic, K. Grube, T. Yoshino, and T. Takabatake *Physica B Condens. Matter.*, vol. 403, p. 1065, 2008.

[29] N. P. Butch, P. Syers, K. Kirshenbaum, A. P. Hope, and J. Paglione *Phys. Rev. B*, vol. 84, p. 220504, 2011.

[30] T. Bay, T. Naka, Y. Huang, and A. de Visser *Phys. Rev. B*, vol. 86, p. 064515, 2012.

[31] F. Tafti, T. Fujii, A. Juneau-Fecteau, S. R. de Cotret, N. Doiron-Leyraud, A. Asamitsu, and L. Taillefer *Phys. Rev. B*, vol. 87, p. 184504, 2013.

[32] G. Volovik *The Universe in a Helium Droplet, Clarendon Press, Oxford.* 2003.

[33] A. Burkov, M. Hook, and L. Balents *Phys. Rev. B*, vol. 84, p. 235126, 2011.

[34] X. Wan, A. M. Turner, A. Vishwanath, and S. Y. Savrasov *Phys. Rev. B*, vol. 83, no. 20, p. 205101, 2011.

[35] F. Fei, X. Bo, R. Wang, B. Wu, J. Jiang, D. Fu, M. Gao, H. Zheng, Y. Chen, X. Wang, *et al. Physical Review B*, vol. 96, p. 041201, 2017.

[36] M. Kargarian, M. Randeria, and Y.-M. Lu *PNAS*, vol. 113, p. 8648, 2016.

[37] A. A. Soluyanov, D. Gresch, Z. Wang, Q. Wu, M. Troyer, X. Dai, and B. A. Bernevig *Nature*, vol. 527, p. 495, 2015.

[38] Y. Sun, S.-C. Wu, M. N. Ali, C. Felser, and B. Yan *Phys. Rev. B*, vol. 92, p. 161107, 2015.

[39] H. Weng, C. Fang, Z. Fang, B. A. Bernevig, and X. Dai *Phys. Rev. X*, vol. 5, p. 011029, 2015.

[40] S.-M. Huang, S.-Y. Xu, I. Belopolski, C.-C. Lee, G. Chang, B. Wang, N. Alidoust, G. Bian, M. Neupane, C. Zhang, *et al. Nat. Commun.*, vol. 6, p. 1, 2015.

[41] B. Lv, H. Weng, B. Fu, X. Wang, H. Miao, J. Ma, P. Richard, X. Huang, L. Zhao, G. Chen, *et al. Phys. Rev. X*, vol. 5, no. 3, p. 031013, 2015.

[42] Z. Liu, J. Jiang, B. Zhou, Z. Wang, Y. Zhang, H. Weng, D. Prabhakaran, S. Mo, H. Peng, P. Dudin, *et al. Nat. Mater.*, vol. 13, p. 677, 2014.

[43] M. Neupane, S.-Y. Xu, R. Sankar, N. Alidoust, G. Bian, C. Liu, I. Belopolski, T.-R. Chang, H.-T. Jeng, H. Lin, *et al. Nat. Commun.*, vol. 5, p. 1, 2014.

[44] S. Borisenko, Q. Gibson, D. Evtushinsky, V. Zabolotnyy, B. Büchner, and R. J. Cava *Phys. Rev. Lett.*, vol. 113, p. 027603, 2014.

[45] H.-J. Noh, J. Jeong, E.-J. Cho, K. Kim, B. Min, and B.-G. Park *Physical review letters*, vol. 119, p. 016401, 2017.

[46] O. Clark, M. Neat, K. Okawa, L. Bawden, I. Marković, F. Mazzola, J. Feng, V. Sunko, J. Riley, W. Meevasana, *et al. Physical review letters*, vol. 120, p. 156401, 2018.

[47] L. Yan, Z. Jian-Zhou, Y. Li, L. Cheng-Tian, L. Ai-Ji, H. Cheng, D. Ying, X. Yu, H. Shao-Long, Z. Lin, *et al. Chinese Physics Letters*, vol. 32, p. 067303, 2015.

[48] Z. Liu, X. Yao, J. Shao, M. Zuo, L. Pi, S. Tan, C. Zhang, and Y. Zhang *J. Am. Chem. Soc.*, vol. 137, p. 10512, 2015.

[49] Y. Qiu, K. N. Sanders, J. Dai, J. E. Medvedeva, W. Wu, P. Ghaemi, T. Vojta, and Y. S. Hor *arXiv:1512.03519*, 2015.

[50] Z. Wang, A. Taskin, T. Frölich, M. Braden, and Y. Ando *Chem. Mat.*, vol. 28, p. 779, 2016.

[51] L. A. Wray, S.-Y. Xu, Y. Xia, Y. San Hor, D. Qian, A. V. Fedorov, H. Lin, A. Bansil, R. J. Cava, and M. Z. Hasan *Nat. Phys.*, vol. 6, p. 855, 2010.

[52] L. Fu and E. Berg *Phys. Rev. Lett.*, vol. 105, p. 097001, 2010.

[53] S. Yonezawa, K. Tajiri, S. Nakata, Y. Nagai, Z. Wang, K. Segawa, Y. Ando, and Y. Maeno *Nat. Phys.*, vol. 13, p. 123, 2017.

[54] T. Hashimoto, K. Yada, A. Yamakage, M. Sato, and Y. Tanaka *J. Phys. Soc. Jpn*, vol. 82, p. 044704, 2013.

[55] L. Fu *Phy. Rev. B*, vol. 90, p. 100509, 2014.

[56] C. Han, H. Li, W. Chen, F. Zhu, M.-Y. Yao, Z. Li, M. Wang, B. F. Gao, D. Guan, C. Liu, *et al. Appl. Phys. Lett.*, vol. 107, p. 171602, 2015.

[57] M. Neupane, Y. Ishida, R. Sankar, J.-X. Zhu, D. S. Sanchez, I. Belopolski, S.-Y. Xu, N. Alidoust, M. M. Hosen, S. Shin, *et al. Sci. Rep.*, vol. 6, no. 1, p. 1, 2016.

[58] V. Shruti, P. Neha, P. Srivastava, and S. Patnaik *Phys. Rev. B*, vol. 92, p. 020506, 2015.

[59] A. Lyons, D. Schleich, and A. Wold *Mat. Res. Bull.*, vol. 11, p. 1155, 1976.

[60] *HelioxVL Insert Manual.* Oxford Instruments NanoScience, 3 ed., 2006.

[61] Z. Koziol *Superconductivity in heavy-fermion and copper-oxide systems.* PhD thesis, University of Amsterdam, 1994.

[62] K. Yokogawa, K. Murata, H. Yoshino, and S. Aoyama *Jpn. J. Appl. Phys.*, vol. 46, p. 3636, 2007.

[63] E. Slooten, T. Naka, A. Gasparini, Y. K. Huang, and A. de Visser *Phys. Rev. Lett.*, vol. 103, p. 097003, 2009.

[64] T. V. Bay, T. Naka, Y. K. Huang, and A. de Visser *Phys. Rev. B*, vol. 86, p. 064515, 2012.

[65] A. Amato *Rev. Mod. Phys.*, vol. 69, p. 1119, 1997.

[66] S. J. Blundell *Contemp. Phys.*, vol. 40, p. 175, 1999.

[67] A. Amato *Physics with Muons: From Atomic Physics to Solid State Physics.* Lecture notes, Univ. Zurich, https://www.psi.ch/en/lmu, 2019.

[68] J. Sonier *Muon Spin Rotation/Relaxation*, 2002, http://musr.ca/intro/musr/muSRBrochure.pdf.

[69] S. L. Lee, R. Cywinski, and S. Kilcoyne *Muon science: Muons in physics, chemistry and materials.* CRC Press, Bristol and Philadelphia, 1999.

[70] L. Michel *Proceedings of the Physical Society. Section A*, vol. 63, p. 514, 1950.

[71] A. Suter *The muon spin spectroscopy technique.* 2014 PSI Summer School on Condensed Matter Research. Lecture slides. Paul Scherrer Institute, Switzerland, https://indico.psi.ch/event/2672/contributions/.

[72] T. Lancaster *Muons in condensed matter research.* Presentation. Durham University, UK, https://slideplayer.com/slide/10983168/.

[73] W. Buckel and R. Kleiner *Superconductivity: fundamentals and applications.* John Wiley & Sons, 2008.

[74] W. Meissner and R. Ochsenfeld *Naturwissenschaften*, vol. 21, p. 787, 1933.

[75] F. London and H. London *Proc. R. Soc. London, Ser. A*, vol. 149, p. 71, 1935.

[76] A. B. Pippard and W. L. Bragg *Proc. R. Soc. London, Ser. A*, vol. 216, p. 547, 1953.

[77] V. L. Ginzburg and L. D. Landau in *On Superconductivity and Superfluidity*, p. 113, Springer, 2009.

[78] J.-C. Toledano and P. Toledano *The Landau theory of phase transitions: application to structural, incommensurate, magnetic and liquid crystal systems*, vol. 3. World Scientific Publishing Company, 1987.

[79] A. Abrikosov *Proc. R. Soc. London, Ser. A*, vol. 2, p. 199, 1957.

[80] J. Bardeen, L. N. Cooper, and J. R. Schrieffer *Physical review*, vol. 108, no. 5, p. 1175, 1957.

[81] J. F. Annett *Superconductivity, superfluids and condensates*, vol. 5. Oxford University Press, 2004.

[82] H. Fröhlich *Phys. Rev.*, vol. 79, p. 845, 1950.

[83] L. N. Cooper *Phys. Rev.*, vol. 104, no. 4, p. 1189, 1956.

[84] D. Ter Haar *Collected papers of LD Landau.* Elsevier, 2013.

[85] R. P. Huebener *Magnetic flux structures in superconductors: extended reprint of a classic text*, vol. 6. Springer Science & Business Media, 2013.

[86] K. Maki *Phys. Physique Fizika*, vol. 1, p. 21, 1964.

[87] J. Auer and H. Ullmaier *Physical Review B*, vol. 7, p. 136, 1973.

[88] N. Kimura, N. Kabeya, K. Saitoh, K. Satoh, H. Ogi, K. Ohsaki, and H. Aoki *Journal of the Physical Society of Japan*, vol. 85, p. 024715, 2016.

[89] Y. Wang, R. Lortz, Y. Paderno, V. Filippov, S. Abe, U. Tutsch, and A. Junod *Phys. Rev. B*, vol. 72, p. 024548, 2005.

[90] A. Hubert *physica status solidi (b)*, vol. 24, p. 669, 1967.

[91] R. A. Hein and R. L. Falge Jr *Phys. Rev.*, vol. 123, p. 407, 1961.

[92] B. D. Cullity and C. D. Graham *Introduction to magnetic materials.* John Wiley & Sons, 2011.

[93] D.-X. Chen, J. A. Brug, and R. B. Goldfarb *IEEE Transactions on magnetics*, vol. 27, p. 3601, 1991.

[94] D.-X. Chen, E. Pardo, and A. Sanchez *IEEE Trans. Magn.*, vol. 41, p. 2077, 2005.

[95] D.-X. Chen, E. Pardo, and A. Sanchez *J. Magn. Magn. Mater.*, vol. 306, p. 135, 2006.

[96] V. Grebinnik, I. Gurevich, V. Zhukov, A. Klimov, L. Levina, V. Maiorov, A. Manych, E. Mel'Nikov, B. Nikol'Skii, A. Pirogov, *et al.* *Sov. Phys. JETP,*, vol. 52, p. 261, 1980.

[97] R. Karl, F. Burri, A. Amato, M. Donegà, S. Gvasaliya, H. Luetkens, E. Morenzoni, and R. Khasanov *Phys. Rev. B*, vol. 99, p. 184515, 2019.

[98] C. P. Bean *Phys. Rev. Lett.*, vol. 8, p. 250, 1962.

[99] L. Gor'Kov *Sov. Phys. JETP*, vol. 7, p. 158, 1958.

[100] L. P. Gor'kov *Sov. Phys. JETP*, vol. 9, p. 1364, 1959.

[101] D. Solenov, M. Nikolo, J. Singleton, J. Jiang, J. Weiss, and E. Hellstrom in *AIP Conference Proceedings*, vol. 1895, p. 060004, AIP Publishing LLC, 2017.

[102] E. Helfand and N. Werthamer *Phys. Rev.*, vol. 147, p. 288, 1966.

[103] N. Werthamer, E. Helfand, and P. Hohenberg *Phys. Rev.*, vol. 147, p. 295, 1966.

[104] K. Maki *Phys. Rev.*, vol. 148, p. 362, 1966.

[105] D. J. Griffiths and D. F. Schroeter *Introduction to quantum mechanics.* Cambridge University Press, 2018.

[106] J. Bardeen, L. Cooper, and J. Schrieffer *Phys. Rev.*, vol. 108, p. 1175, 1957.

[107] D. Saint-James and P. de Gennes *Phys. Lett.*, vol. 7, p. 306, 1963.

[108] W. J. Tomasch and A. S. Joseph *Phys. Rev. Lett.*, vol. 12, p. 148, 1964.

[109] M. Tinkham *Phys. Lett.*, vol. 9, 1964.

[110] J. Woollam and C. Chu *High-pressure and Low-temperature Physics.* Springer Science & Business Media, 2012.

[111] B. Lorenz and C. Chu in *Frontiers in Superconducting Materials*, p. 459, Springer, 2005.

[112] C. Chu, T. Smith, and W. Gardner *Phys. Rev. Lett.*, vol. 20, no. 5, p. 198, 1968.

[113] J. Hatton *Phys. Rev.*, vol. 103, p. 1167, 1956.

[114] M. Míšek *Magnetic and transport properties of f-electron compounds under extreme conditions.* PhD thesis, Charles University, 2013.

[115] E. G. M. *Soviet Phys.*, vol. 11, p. 696, 1960.

[116] P. B. Allen and R. Dynes *Phys. Rev. B*, vol. 12, no. 3, p. 905, 1975.

[117] R. Dynes *Solid State Commun.*, vol. 10, p. 615, 1972.

[118] W. McMillan *Physical Review*, vol. 167, no. 2, p. 331, 1968.

[119] R. Kubo and T. Toyabe *Magnetic resonance and relaxation.* North-Holland, Amsterdam, 1967.

[120] H. Noh, J. Jeong, E. Cho, K. Kim, B. Min, and B. Park *Phys. Rev. Lett.*, vol. 119, p. 016401, 2017.

[121] F. Fei, X. Bo, R. Wang, B. Wu, J. Jiang, D. Fu, M. Gao, H. Zheng, Y. Chen, X. Wang, H. Bu, F. Song, X. Wan, B. Wang, and G. Wang *Phys. Rev. B*, vol. 96, p. 041201, 2017.

[122] A. A. Soluyanov *Physics*, vol. 10, p. 74, 2017.

[123] C.-K. Chiu, J. C. Y. Teo, A. P. Schnyder, and S. Ryu *Rev. Mod. Phys.*, vol. 88, p. 035005, 2016.

[124] B. Yan and C. Felser *Annu. Rev. Condens. Matter Phys.*, vol. 8, p. 337, 2017.

[125] N. P. Armitage, E. J. Mele, and A. Vishwanath *e-print*, 2017.

[126] S. M. Young, S. Zaheer, J. C. Y. Teo, C. L. Kane, E. J. Mele, and A. M. Rappe *Phys. Rev. Lett.*, vol. 108, p. 140405, 2012.

[127] X. Wan, A. M. Turner, A. Vishwanath, and S. Y. Savrasov *Phys. Rev. B*, vol. 83, p. 205101, 2011.

[128] A. A. Soluyanov, D. Gresch, Z. Wang, Q. Wu, M. Troyer, X. Dai, and B. Bernevig *Nature*, vol. 257, p. 495, 2015.

[129] H. Huang, S. Zhou, and W. Duan *Phys. Rev. B*, vol. 94, p. 121117, 2016.

[130] M. Yan, H. Huang, K. Zhang, E. Wang, Y. W., K. Deng, G. Wan, H. Zhang, M. Arita, H. Yang, Z. Sun, H. Yao, W. Y., F. S., D. W., and Z. S. *Nature Comm.*, vol. 8, p. 257, 2017.

[131] J. Guggenheim, F. Hulliger, and J. Müller *Helv. Phys. Acta*, vol. 34, p. 408, 1961.

[132] Y. Liu, J. Zhao, L. Yu, C. Lin, A. Liang, C. Hu, Y. Ding, Y. Xu, S. He, L. Zhao, L. G.D., D. X.L., J. Zhang, C. Chen, Z. Xu, H. Weng, X. Dai, Z. Fang, and Z. X.J. *Chin. Phys. Lett.*, vol. 32, p. 067303, 2015.

[133] M. Sato and S. Fujimoto *J. Phys. Soc. Jpn*, vol. 85, p. 027001, 2016.

[134] M. Sato and Y. Ando *Rep. Progr. Phys.*, vol. 80, p. 076501, 2017.

[135] A. Kjekshus and W. B. Pearson *Can. J. Phys.*, vol. 43, p. 438, 1965.

[136] C. Raub, V. Compton, T. Geballe, B. Matthias, J. Maita, and G. Hull *J. Phys. Chem. Solids*, vol. 26, no. 12, p. 2051, 1965.

[137] Z. Wang, A. A. Taskin, T. Frölich, M. Braden, and Y. Ando *Chem. Mater.*, vol. 28, p. 779, 2016.

[138] L. L. Zhao, S. Lausberg, H. Kim, M. A. Tanatar, M. Brando, R. Prozorov, and E. Morosan *Phys. Rev. B*, vol. 85, p. 214526, 2012.

[139] S. Sun, L. Liu, and H. Lei *J. Phys. Condens. Matt.*, vol. 28, p. 085701, 2016.

[140] N. Kimura, N. Kabeya, K. Saitoh, K. Satoh, H. Ogi, K. Ohsaki, and H. Aoki *J. Phys. Soc. Jpn*, vol. 85, p. 024715, 2016.

[141] D. Saint-James and P. G. de Gennes *Phys. Lett.*, vol. 7, p. 306, 1963.

[142] L. Thomassen *Z. Phys. Chem.*, vol. B2, p. 349, 1929.

[143] S. Manzeli, D. Ovchinnikov, D. Pasquier, O. V. Yazyev, and A. Kis *Nat. Rev. Mat.*, vol. 2, p. 17033, 2017.

[144] H. Myron *Sol. State Comm.*, vol. 15, p. 395, 1974.

[145] A. E. Dunsworth *J. Low Temp. Phys.*, vol. 19, p. 51, 1975.

[146] J.-P. Jan and H. L. Skriver *J. Phys. F: Metal Phys.*, vol. 7, p. 1719, 1977.

[147] Hooda, M. K. and Yadav, C. S. *EPL*, vol. 121, no. 1, p. 17001, 2018.

[148] D.-X. Chen, E. Pardo, and A. Sanchez *IEEE Transactions on Magnetics*, vol. 38, p. 1742, 2002.

[149] C. P. Poole, H. A. Farach, R. J. Creswick, and R. Prozorov *Superconductivity.* Amsterdam: Elsevier, 2nd ed., 2007.

[150] R. A. Hein and R. L. Falge *Phys. Rev.*, vol. 123, p. 407, 1961.

[151] M. Tinkham *Introduction to Superconductivity.* McGraw-Hill Inc., New York, 1996.

[152] K. Kudo, H. Ishii, and M. Nohara *Phys. Rev. B*, vol. 93, p. 140505, 2016.

[153] J. L. Weber and J. P. McEvoy *Phys. Stat. Sol. b*, vol. 57, p. K87, 1973.

[154] N. R. Werthamer, E. Helfand, and P. C. Hohenberg *Phys. Rev.*, vol. 147, p. 295, 1966.

[155] D. J. Rebar *Exploring superconductivity in chiral structured AuBe.* PhD thesis, Louisiana State University, 2015.

[156] J. Auer and H. Ullmaier *Phys. Rev. B*, vol. 7, p. 136, 1973.

[157] S. Yip *Ann. Rev. Cond. Matt. Phys.*, vol. 5, p. 15, 2013.

[158] T. Hashimoto, S. Kobayashi, Y. Tanaka, and M. Sato *Phys. Rev. B*, vol. 94, p. 014510, 2016.

[159] S. Kobayashi and M. Sato *Phys. Rev. Lett.*, vol. 115, p. 187001, 2015.

[160] G. Bednik, A. A. Zyuzin, and A. A. Burkov *Phys. Rev. B*, vol. 92, p. 035153, 2015.

[161] M. S. Bahramy, O. J. Clark, B.-J. Yang, J. Feng, L. Bawden, J. M. Riley, I. Markovic, F. Mazzola, V. Sunko, D. Biswas, S. P. Cooil, M. Jorge, J. W. Wells, M. Leandersson, T. Balasubramanian, J. Fujii, I. Vobornik, J. E. Rault, T. K. Kim, M. Hoesch, K. Okawa, M. Asakawa, T. Sasagawa, T. Eknapakul, W. Meevasana, and P. D. C. King *Nature Mat.*, vol. 17, p. 21, 2018.

[162] O. J. Clark, M. J. Neat, K. Okawa, L. Bawden, I. Marković, F. Mazzola, J. Feng, V. Sunko, J. M. Riley, W. Meevasana, J. Fujii, I. Vobornik, T. K. Kim, M. Hoesch, T. Sasagawa, P. Wahl, M. S. Bahramy, and P. D. C. King *Phys. Rev. Lett.*, vol. 120, p. 156401, 2018.

[163] H. Leng, C. Paulsen, Y. K. Huang, and A. de Visser *Phys. Rev. B*, vol. 96, p. 220506, 2017.

[164] B. Y. Shapiro, I. Shapiro, D. Li, and B. Rosenstein *J. Phys.: Condens. Matter*, vol. 30, p. 335403, 2018.

[165] Amit and Y. Singh *Phys. Rev. B*, vol. 97, p. 054515, 2018.

[166] M. V. Salis, P. Rodière, H. Leng, Y. K. Huang, and A. de Visser *J. Phys: Condens. Matter*, vol. 30, p. 505602, 2018.

[167] S. Teknowijoyo, N. H. Jo, M. S. Scheurer, M. A. Tanatar, K. Cho, S. L. Bud'ko, P. P. Orth, P. C. Canfield, and R. Prozorov *Phys. Rev. B*, vol. 98, p. 024508, 2018.

[168] S. Das, Amit, A. Sirohi, L. Yadav, S. Gayen, Y. Singh, and G. Sheet *Phys. Rev. B*, vol. 97, p. 014523, 2018.

[169] J. A. Voerman, J. C. de Boer, T. Hashimoto, Y. Huang, C. Li, and A. Brinkman *Phys. Rev. B*, vol. 99, p. 014510, 2019.

[170] R. C. Xiao, P. L. Gong, Q. S. Wu, W. J. Lu, M. J. Wei, J. Y. Li, H. Y. Lv, X. Luo, P. Tong, X. B. Zhu, and Y. P. Sun *Phys. Rev. B*, vol. 96, p. 075101, 2017.

[171] T. V. Bay, T. Naka, Y. K. Huang, and A. de Visser *Phys. Rev. B*, vol. 86, p. 064515, 2012.

[172] T. V. Bay, T. Naka, Y. K. Huang, H. Luigjes, M. S. Golden, and A. de Visser *Phys. Rev. Lett.*, vol. 108, p. 057001, 2012.

[173] C. Soulard, P. Petit, P. Deniard, M. Evain, S. Jobic, M.-H. Whangbo, and A.-C. Dhaussy *Journal of Solid State Chemistry*, vol. 178, no. 6, p. 2008, 2005.

[174] J.-Q. Lei, K. Liu, S. Huang, X.-C. Mao, B.-S. Hou, J. Tan, and X.-L. Zhou *Chemical Physics Letters*, vol. 687, p. 250, 2017.

[175] K. Kim, S. Kim, J. S. Kim, H. Kim, J.-H. Park, and B. I. Min *Phys. Rev. B*, vol. 97, p. 165102, 2018.

[176] G. Ryu *Journal of Superconductivity and Novel Magnetism*, vol. 28, no. 11, p. 3275, 2015.

[177] W. Zheng, R. Schönemann, N. Aryal, Q. Zhou, D. Rhodes, Y.-C. Chiu, K.-W. Chen, E. Kampert, T. Förster, T. J. Martin, G. T. McCandless, J. Y. Chan, E. Manousakis, and L. Balicas *Phys. Rev. B*, vol. 97, p. 235154, 2018.

[178] G. Volovik *Physics-Uspekhi*, vol. 61, p. 89, 2018.

[179] D. Peets, E. Cheng, T. Ying, M. Kriener, X. Shen, S. Li, and D. Feng *Phys. Rev. B*, vol. 99, p. 144519, 2019.

[180] A. Sirohi, D. S., P. Adhikary, R. R. Chowdhury, A. Vashist, Y. Singh, S. Gayen, T. Das, and G. Sheet *J. Phys: Condens. Matter*, vol. 31, p. 085701, 2019.

[181] Y. Wang, R. Lortz, Y. Paderno, V. Filippov, S. Abe, U. Tutsch, and A. Junod *Phys. Rev. B*, vol. 72, p. 024548, 2005.

[182] T. Le, L. Yin, Z. Feng, Q. Huang, L. Che, J. Li, Y. Shi, and X. Lu *Phys. Rev. B*, vol. 99, p. 180504, 2019.

[183] A. Yaounc and P. Dalmas de Réotier *Muon spin rotation, relaxation and resonance; applications to condensed matter.* Oxford: Oxford University Press, 2011.

[184] M. Gladisch, D. Herlach, H. Metz, H. Orth, G. zu Putlitz, A. Seeger, H. Teichler, W. Wahl, and M. Wigand *Hyperfine Interact.*, vol. 6, p. 109, 1979.

[185] V. Grebinnik, I. Gurevich, V. Zhukov, A. Klimov, L. Levina, V. Maiorov, A. Manych, E. Mel'nikov, B. Nikol'skii, A. Pirogov, A. Ponomarev, V. Roganov, V. Selivanov, and V. Suetin *Sov. Phys. JETP*, vol. 52, p. 261, 1980.

[186] V. S. Egorov, G. Solt, C. Baines, D. Herlach, and U. Zimmermann *Phys. Rev. B*, vol. 64, p. 024524, 2001.

[187] C. M. Aegerter, H. Keller, S. L. Lee, C. Ager, F. Y. Ogrin, R. Cubitt, E. M. Forgan, W. J. Nutall, P. G. Kealey, S. H. Lloyd, S. T. Johnson, T. M. Riseman, and M. P. Nutley *arXiv:cond-mat/0305595*, 2003.

[188] V. Kozhevnikov, A. Suter, T. Prokscha, and C. Van Haesendonck *arXiv:1910.09082*, 2018.

[189] R. Khasanov, M. M. Radonjić, H. Luetkens, E. Morenzoni, G. Simutis, S. Schönecker, W. Appelt, A. Östlin, L. Chioncel, and A. Amato *Phys. Rev. B*, vol. 99, p. 174506, 2019.

[190] R. Karl, F. Burri, A. Amato, M. Donegà, S. Gvasaliya, H. Luetkens, E. Morenzoni, and R. Khasanov *Phys. Rev. B*, vol. 99, p. 184515, 2019.

[191] A. Drew, S. Lee, F. Ogrin, D. Charalambous, N. Bancroft, D. M. Paul, T. Takabatake, and C. Baines *Physica B*, vol. 374, p. 270, 2006.

[192] V. K. Anand, A. D. Hillier, D. T. Adroja, A. M. Strydom, H. Michor, K. A. McEwen, and B. D. Rainford *Phys. Rev. B*, vol. 83, p. 064522, 2011.

[193] V. K. Anand, D. Britz, A. Bhattacharyya, D. T. Adroja, A. D. Hillier, A. M. Strydom, W. Kockelmann, B. D. Rainford, and K. A. McEwen *Phys. Rev. B*, vol. 90, p. 014513, 2014.

[194] M. Smidman, A. D. Hillier, D. T. Adroja, M. R. Lees, V. K. Anand, R. P. Singh, R. I. Smith, D. M. Paul, and G. Balakrishnan *Phys. Rev. B*, vol. 89, p. 094509, 2014.

[195] D. Singh, A. D. Hillier, and R. P. Singh *Phys. Rev. B*, vol. 99, p. 134509, 2019.

[196] J. Beare, M. Nugent, M. N. Wilson, Y. Cai, T. J. S. Munsie, A. Amon, A. Leithe-Jasper, Z. Gong, S. L. Guo, Z. Guguchia, Y. Grin, Y. J. Uemura, E. Svanidze, and G. M. Luke *Phys. Rev. B*, vol. 99, p. 134510, 2019.

[197] F. L. Pratt *Physica B: Condensed Matter*, vol. 289, p. 710, 2000.

[198] A. Suter and B. Wojek *Physics Procedia*, vol. 30, p. 69, 2012.

[199] R. P. Huebener *Magnetic Flux Structures in Superconductors.* Springer, Berlin, 1979.

[200] L. D. Landau *Zh. Eksp. Teor. Fiz.*, vol. 7, p. 371, 1937.

[201] D. Chen, J. Brug, and R. Goldfarb *IEEE Trans. Magn.*, vol. 27, p. 3601, 1991.

[202] E. Pardo, D. Chen, and A. Sanchez *J. Appl. Phys.*, vol. 96, p. 5365, 2004.

[203] D. Chen, E. Pardo, and A. Sanchez *IEEE Trans. Magn.*, vol. 37, p. 3877, 2001.

[204] H. Zhang, C.-X. Liu, X.-L. Qi, X. Dai, Z. Fang, and S.-C. Zhang *Nature Phys.*, vol. 5, p. 438, 2009.

[205] Y. Xia, D. Qian, D. Hsieh, L.Wray, A. Pal, H. Lin, A. Bansi, D. Grauer, Y. S. Hor, R. J. Cava, and M. Z. Hasan *Nature Phys.*, vol. 5, p. 398, 2009.

[206] D. Hsieh, Y. Xia, D. Qian, L. Wray, J. H. Dil, F. Meier, J. Osterwalder, L. Patthey, J. G. Checkelsky, N. P. Ong, A. V. Fedorov, H. Lin, A. Bansil, D. Grauer, Y. S. Hor, R. J. Cava, and M. Z. Hasan *Nature*, vol. 460, p. 1101, 2009.

[207] Y. S. Hor, A. J. Williams, J. G. Checkelsky, P. Roushan, J. Seo, Q. Xu, H. W. Zandbergen, A. Yazdani, N. P. Ong, and R. J. Cava *Phys. Rev. Lett.*, vol. 104, p. 057001, 2010.

[208] Z. Liu, X. Yao, J. Shao, M. Zuo, L. Pi, S. Tan, C. Zhang, and Y. Zhang *J. Am. Chem. Soc.*, vol. 137, p. 10512, 2015.

[209] Y. Qiu, K. N. Sanders, J. Dai, J. E. Medvedeva, W. Wu, P. Ghaemi, T. Vojta, and Y. S. Hor *e-print: arXiv:1512.03519v1*, 2015.

[210] T. Mizushima, Y. Tsutsumi, T. Kawakami, M. Sato, M. Ichioka, and K. Machida *J. Phys. Soc. Jpn*, vol. 85, p. 022001, 2016.

[211] A. Schnyder, S. Ryu, A. Furusaki, and A. Ludwig *Phys. Rev. B*, vol. 78, p. 195125, 2008.

[212] L. Fu and E. Berg *Phys. Rev. Lett.*, vol. 105, p. 097001, 2010.

[213] M. Kriener, K. Segawa, Z. Ren, S. Sasaki, and Y. Ando *Phys. Rev. Lett.*, vol. 106, p. 127004, 2011.

[214] S. Sasaki, M. Kriener, K. Segawa, K. Yada, Y. Tanaka, M. Sato, and Y. Ando *Phys. Rev. Lett.*, vol. 107, p. 217001, 2011.

[215] N. Levy, T. Zhang, J. Ha, F. Sharifi, A. A. Talin, Y. Kuk, and J. A. Stroscio *Phys. Rev. Lett.*, vol. 110, p. 117001, 2013.

[216] C. Q. Han, H. Li, W. J. Chen, F. Zhu, M.-Y. Yao, Z. J. Li, M. Wang, B. F. Gao, D. Guan, C. Liu, C. L. Gao, D. Qian, and J.-F. Jia *Appl. Phys. Lett.*, vol. 107, p. 171602, 2015.

[217] M. Neupane, Y. Ishida, R. Sankar, J.-X. Zhu, D. S. Sanchez, I. Belopolski, S.-Y. Xu, N. Alidoust, S. Shin, F. Chou, M. Z. Hasan, and T. Durakiewicz *Sci. Reports*, vol. 6, p. 22557, 2016.

[218] Shruti, V. K. Maurya, P. Neha, P. Srivastava, and S. Patnaik *Phys. Rev. B*, vol. 92, p. 020506(R), 2015.

[219] Y. Pan, A. M. Nikitin, G. K. Araizi, Y. K. Huang, Y. Matsushita, T. Naka, and A. de Visser *Sci. Reports*, vol. 6, p. 28632, 2016.

[220] A. M. Nikitin, Y. Pan, Y. K. Huang, T. Naka, and A. de Visser *Phys. Rev. B*, vol. 94, p. 144516, 2016.

[221] K. Matano, M. Kriener, K. Segawa, Y. Ando, and G.-Q. Zheng *Nature Phys.*, vol. 12, p. 852, 2016.

[222] S. Yonezawa, K. Tajiri, S. Nakata, Y. Nagai, Z. Wang, K. Segawa, Y. Ando, and Y. Maeno *Nature Phys.*, vol. 13, p. 123, 2017.

[223] T. Asaba, B. Lawson, C. Tinsman, L. Chen, P. Corbae, G. Li, Y. Qiu, Y. Hor, L. Fu, and L. Li *Phys. Rev. X*, vol. 7, p. 011009, 2017.

[224] Y. Nagai, H. Nakamura, and M. Machida *Phys. Rev. B*, vol. 86, p. 094507, 2012.

[225] L. Fu *Phys. Rev. B*, vol. 90, p. 100509(R), 2014.

[226] J. Venderbos, V. Kozii, and L. Fu *Phys. Rev. B*, vol. 94, p. 180504, 2016.

[227] G. M. Luke, A. Keren, L. P. Le, W. D. Wu, Y. J. Uemura, D. A. Bonn, L. Taillefer, and J. D. Garrett *Phys. Rev. Lett.*, vol. 71, p. 1466, 1993.

[228] E. H. Brandt *Phys. Rev. B*, vol. 37, p. 2349, 1988.

[229] E. H. Brandt *J. Low Temp. Phys.*, vol. 73, no. 5, p. 355, 1988.

[230] Y. M. Belousov, V. N. Gorbunov, V. P. Smilga, and V. I. Fesenko *Usp. Fiz. Nauk*, vol. 160, p. 55, 1990.

[231] C. M. Aegerter and S. L. Lee *Appl. Magn. Reson.*, vol. 13, p. 75, 1997.

[232] W. D. Wu, A. Keren, L. P. Le, B. J. Sternlieb, G. M. Luke, Y. J. Uemura, P. Dosanjh, and T. M. Riseman *Phys. Rev. B*, vol. 47, p. 8172, 1993.

[233] H. Köhler *Phys. Stat. Sol. (b)*, vol. 58, p. 91, 1973.

[234] E. Lahoud, E. Maniv, M. S. Petrushevsky, M. Naamneh, A. Ribak, S. Wiedmann, L. Petaccia, Z. Salman, K. B. Chashka, Y. Dagan, and A. Kanigel *Phys. Rev. B*, vol. 88, p. 195107, 2013.

[235] J. A. Krieger, A. Kanigel, A. Riback, E. Pomjakushina, K. B. Chashka, K. Conder, E. Morenzoni, T. Prokscha, A. Suter, and Z. Salman *ArXiv e-prints*, 2017.

[236] C. Collignon, B. Fauqué, A. Cavanna, U. Gennser, D. Mailly, and K. Behnia *Phys. Rev. B*, vol. 96, p. 224506, 2017.

[237] M. Kriener, K. Segawa, Z. Ren, S. Sasaki, S. Wada, S. Kuwabata, and Y. Ando *Phys. Rev. B*, vol. 84, p. 054513, 2011.

[238] C. Mann, D. West, I. Miotkowski, Y. P. Chen, S. Zhang, and C.-K. Shih *Phys. Rev. B*, vol. 89, p. 155312, 2014.

List of publications

1. **H. Leng**, A. Ohmura, L.N. Anh, F. Ishikawa, T. Naka, Y.K. Huang and A. de Visser, *Superconductivity under pressure in the Dirac semimetal* $PdTe_2$, Journal of Physics: Condensed Matter, 32(2), 025603, (2020). (Chapter 5)

2. **H. Leng**, J.C. Orain, A. Amato, Y.K. Huang and A. de Visser, *Type-I superconductivity in the Dirac semimetal* $PdTe_2$ *probed by* μSR, Physical Review B, 100(22), 224501, (2019). (Chapter 6)

3. **H. Leng**, D. Cherian, Y.K. Huang, J.C. Orain, A. Amato, and A. de Visser, *Muon spin rotation study of the topological superconductor* $Sr_xBi_2Se_3$, Physical Review B, 97(5), 054503, (2018). (Chapter 7)

4. **H. Leng**, C. Paulsen, Y.K. Huang and A. de Visser, *Type-I superconductivity in the Dirac semimetal* $PdTe_2$, Physical Review B, 96(22), 220506(R), (2017). (Chapter 4)

5. L.H. Bao, F. Yang, O. Tegus, Y.K. Huang, **H. Leng** and A. de Visser, *Enhanced electron-phonon coupling in* NbB_2 *by nanoscaling the grain size*, Materials Characterization, 150, 13-21, (2019).

6. M.V. Salis, P. Rodière, **H. Leng**, Y.K. Huang and A. de Visser, *Penetration depth study of the type-I superconductor* $PdTe_2$, Journal of Physics: Condensed Matter, 30(50), 505602, (2018).

7. L.H. Bao, R.Y. Tao, Y.K. Huang, **H. Leng** and A. de Visser, *Anisotropy study on thermionic emission and magnetoresistivity of single crystal* CeB_6, Acta Physica Sinica, 66(18), 186102, (2017).

8. **H. Leng**, M. Zhou, J. Zhao, Y.M. Han and L.F. Li, *The thermoelectric performance of anisotropic SnSe doped with Na*, RSC Advances, 6(11), 9112-9116, (2016).

9. **H. Leng**, M. Zhou, J. Zhao, Y. Han and L. Li, *Optimization of thermoelectric performance of anisotropic* $Ag_x\ Sn_{1-x}Se$ *compounds*, Journal of Electronic Materials, 45(1), 527-534, (2016).

10. Y.M. Han, J. Zhao, M. Zhou, X.X. Jiang, **H. Leng** and L.F. Li, *Thermoelectric performance of SnS and SnS–SnSe solid solution*, Journal of Materials Chemistry A, 3(8), 4555-4559, (2015).

Acknowledgement

Time is like a fleeting show. At the end of my PhD journey at UvA, it's my pleasure to thank all people I met in the last 4 years who offered me great support in my daily life. I have enjoyed this period very much because of you talented and amazing people without whom I would not have been able to get this far.

First and foremost, I would like to express my most sincere gratitude to my promotor and supervisor, Dr. Anne de Visser. You are an exemplary experimental physicist and inspired me with a rigorous attitude and passionate enthusiasm towards research. From you I learned what a good scientist should be. Dear Anne, thank you for offering me the great opportunity to work in the Quantum Matter group and ushering me into the fascinating world of low temperature physics. I am grateful for your always timely feedback and great patience while performing experiments, writing scientific papers, presenting at conferences, as well as completing this thesis manuscript. Additionally I had a lot of fun all around the world at different conferences and μSR experiments from Prague to Villigen to Peking to Okayama. Thanks to you for this support. Besides research, I also enjoyed all group dinners at your place and activities across The Netherlands that made me feel at home (also thanks to Ineke). Likewise thank you Prof. Mark Golden for being my co-promotor. Dear Mark, you are calm and confident at all times while giving formal or informal scientific talks. I was unconsciously influenced by your high spirits on research. Thanks for your advice and comments on my presentations that always bring me inspiration. I am grateful for you offering your precious time to help me improving my English. Otherwise I had great time enjoying the group dinners at your place, many thanks.

High-quality crystals are very important for experimental research. Special thanks to Dr. Yingkai Huang and Dr. Dona Cherian for providing high-quality single crystals and helping me performing X-ray diffraction and EDX measurements. Thanks to Dr. Erik van Heumen for your insightful questions in the group meetings that motivated me to think harder. Thanks to Hugo Schlatter and Huib Luigjes for their kind assistance to keep all the equipment running smoothly.

I have been very lucky to collaborate with some excellent researchers out of UvA. First I owe my deep gratitude to the high pressure expert group from Japan.

Dr. Ayako Ohmura (Niigata University, Japan), you are the most organised person I've seen and working with you is always fun and productive. Your hard-working and perfectness on experiments inspired me a lot. Dear Ayako, many thanks to you for teaching me how to work with a pressure cell, constructive recommendation on the manuscript, delicious homemade Japanese food and all interesting conversations. Dr. Fumihiro Ishikawa (Niigata University, Japan) and Dr. Takashi Naka (National Institute for Materials Science, Tsukuba, Japan), thank you for helping me working with the pressure cell and valuable comments on the paper. Many thanks go to Dr. Carley Paulsen (Néel Institute, Grenoble, France) for the intensive magnetic measurements and helpful discussions. I also would like to thank Dr. Alex Amato (Paul Scherrer Institute, Switzerland) and Dr. Jean-Christophe Orain (Paul Scherrer Institute, Switzerland), Dr. Luong Ngoc Anh (Hanoi University of Science and Technology, Vietnam) and Dr. Lihong Bao (Inner Mongolia Normal University, China) for their kind help and collaboration. It was always pleasant to work together.

Also I wish to express my gratitude to all thesis committee members for their valuable time and feedback on my thesis. The China Scholarship Council is truly appreciated for financial support of my PhD project. In addition, I would like to pay my special regards to Prof. Laifeng Li, Dr. Min Zhou and Dr. Yemao Han from the Technical Institute of Physics and Chemistry, CAS, China for their help in obtaining the scholarship.

During my PhD project I have spent most of my time in the lab working with amazing fellows. I would like to recognize the invaluable assistance that you all, former and current QMat members, provided during my study. Dear Yu Pan, you were extremely helpful in the starting year of my life abroad. My anxiety for the unknown future was relieved when you showed up at airport at 6 o'clock a.m.. With your help I found an apartment, got familiar with the lab and new colleagues, and made new friends. It is said a good beginning is half done, thanks to you for offering me such a wonderful beginning of my PhD. Artem Nikitin, thank you for teaching me how to work with the Heliox and sharing your experience how to extend social circles and improve my English. I always enjoyed having conversations with you. Marc Salis, it was very pleasant to work with you shoulder to shoulder in the past two years and to have fun both in the lab and Veldhoven. You were always supportive, funny and a very good friend to me. Thank you for showing me the Dutch perspective in many aspects, to help me study Dutch and being my paranymph. I cherish all deep conversations we've had. George Araizi Kanoutas, thanks for your constant encouragement on my spoken English and creating a friendly atmosphere when I just joined our group. Thank you Stephan Bron and Xuanbo Feng for serious or brainstorm conversations we had. Both your passion towards experiments and theory in physics touched me deeply. Thank you Shyama Ramankutty, for being very comforting and making me feel at home whenever I talked to you. Alona Tytarenko, you were always smiling and full of zest. Thank you for warming up the “cold lunchtime” sometimes that brought me a more pleasant lunch. Steef Smit, Jans Henke, Lewis Bawden and Maarten Berben, thank you for the enjoyable time we’ve spent in the various activities, such as beer drinking, BBQs, soccer, disco and lunch club. The discussions we had always came with new knowledge about your culture. Jelle Lorentz, thanks for teaching me the rules of chess, I had fun to play with Fumi. I would like to thank people who have worked in our group: Guoyong Zhang, Linda, Roeland, Xanthe, Abel, Dominique, Floris and Florian. I am also thankful to other people within the IoP: Yingying Tang, Ankit Goyal, Chia-Ching Huang and Francesca Fama. Yingying, thanks for being my paranymph.

Furthermore, I would also like to acknowledge all staff members of the Van der Waals-Zeeman Institute for all the help they gave to make my research work smoothly. Thanks to Gerrit Hardeman, Johan Mozes, Daan Giesen from the mechanical and electronic workshops for technical support of the PPMS. Thanks to Anne-Marieke Crommentuijn, Astrid Harryson, Jirina Salkova, Klaartje Wartenbergh and Joost van Mameren for all administrative assistance. Thanks to Truc Ngo-Ha from the human resource department of the university for arranging my contract and residence permit.

The next part will be in Chinese, thanking people who did not directly contribute to the project described in this thesis, but more to me being able to write this thesis.

在阿姆的四年里，很幸运遇见很多优秀可爱的人，感谢所有的人，你们的存在为我在异国他乡的日子增添了许多的温暖和快乐。朱姗，很高兴在阿姆最初的一年认识你，谢谢你晚上陪我一起去看租房，一起去东欧玩的很开心。曹凌雪，你是我在荷兰第一个室友，谢谢你知道我的生日后，给我准备了蛋糕和梨花，常常怀念同住的日子一起执酒秉烛夜谈至夜深，还有一起涮着火锅畅想科研之外的发财之路。赵永贵，谢谢你最后帮我租到了这么好的公寓还留下了家具，你的工作效率和在沙特奢华的学术生活同样令人惊艳。吴燕妮，很高兴在阿姆认识独立又多才多艺的你，每次聊天都会让我有更多的思考。谢谢你带给我的快乐时光，一起吃火锅打牌，去梵高公园骑车，滑冰，很遗憾说好的温泉没有泡成。汤莹莹，谢谢你们家小七陪我度过了闭关修炼的黑色圣诞周，尽管我很烦它的上蹿下跳在家里跑酷，也很高兴在阿姆最后一年认识你，一起学荷兰语，看灯光节，滑冰，也谢谢你做我的答辩助理。贾文亮，很高兴跟你是同一楼层的邻居，谢谢你在我隔离在家工作的时候不胜其烦的帮我带资料，还有你意大利同事在你家做的披萨很好吃，我至今回味无穷。刘哲，可惜只做了一年邻居，谢谢你美味的卤鸡翅和水煎包，我会怀念跟你一起冒雨参加狄更斯节，骑车逛遍阿姆灯光节所有主题还有逗猫瞎扯的日子。还有很多朋友，在课程上认识的，在会议上认识的，聚会出去玩认识的，虽然后来交集不多，但是彼此活跃在彼此的朋友圈里，分享生活和观点，互相支持，像是古人说的神交，谢谢你们的点点滴滴同样丰富着我的生活。特别感谢远在意大利的赵晓蕾，你见证了我从高中到现在所有所有的起起落落，悲伤开心，谢谢你这么多年来的支持鼓励包容理解，于我你是朋友更像亲人。还有远在国内的梁师师，谢谢你在这一特殊时期的关心和帮助，不遗余力帮我购置邮寄口罩等防护用品。

最后，最深沉真挚的感谢给我最爱的家人，我的父母，姐姐所有的亲人。谢谢你们这么多年

给予我精神和生活的关心和支持，教我如何为人，如何抉择，如何努力追寻，你们的存在是我最大的财富和最坚强的后盾。

Huaqian Leng（冷华倩）
April 2020, Amsterdam